C O N T E N T S

Study and Analysis of Fibre Reinforced Textile Composites Developed by using Recycled Viscose and Polyester Fibres from Apparel industry Cut Panel Wastes

C. Rajesh Kumar[1] 0000-0003-4071-5425
T. Vidya[1] 0000-0002-7450-9219
C. Prakash[2] 0000-0003-2472-6765
D. Raja[1]* 0000-0002-1258-2525

[1] Department of Fashion Technology, Sona College of Technology, Salem-636005, Tamil Nadu, India

[2] Department of Handloom and Textile Technology, Indian Institute of Handloom Technology, Govt. of India, Ministry of Textiles, Fulia Colony, Shantipur, Nadia-741 402, West Bengal, India

Corresponding Author: Prakash C, dearcprakash@gmail.com

ABSTRACT

Garment cut wastes from the apparel industry are used in a variety of sectors. Apparel cut wastes and recycled fibres from apparel cut wastes are typically employed in the textile, home textile, automobile, architecture, and agrotextile industries for low performance applications. The major aim of this research work is to study and to develop high-performance composite materials using recycled fibres acquired from apparel cut wastes. Based on its properties, these composites can be used as replacement of wood panels in furniture industries, partition boards, electrical boards etc. To create these composites, recycled fibres from viscose, polyester, and viscose/polyester apparel cut panel wastes are utilized as reinforcements. Epoxy resin, kaolinite, and polypropylene sheets are used as matrices in the manufacturing of these composites. These composites were developed using a variety of reinforcement and matrix combinations. One of the fibre reinforced composites key advantages is combining the various features of many materials to create another unique, high-performance material. Technical characteristics of developed composites, including thickness, mass per unit area, tensile strength, flexural strength, impact strength, water absorption, and scanning electron microscopy, were investigated and evaluated. The findings suggest that viscose/polyester blended fibre reinforced composite exhibit higher mechanical performances when compared to other viscose and polyester fibre reinforced composites, and they are therefore recommended for a wide range of possible and potential applications.

1. INTRODUCTION

Natural resources including soil, clay, and wood are being used more and more frequently in the production of various composite materials for household and structural objects [1]. New concepts and workable goods can be generated using a variety of recycling techniques to meet this demand for necessities while also consuming fewer natural resources to safeguard the environment [2]. The demand for environmentally friendly items has increased recently, and it is vital to do so in order to maintain our ecosystem by consuming minimal natural resources. The demand for composite materials is increasing across a range of industries for both low- and high-end performance applications [4]. Depending on the various clothing product styles, the cutting efficiency in the apparel business ranges on average from a minimum of 70% to a maximum of 90%. Therefore, during the process of making clothes, 10 to 30 percent of the textiles are wasted as garment cut wastes in apparel industry cutting segment [5]. These cut wastes are majorly used for low performance applications like fibre fill, carpet manufacturing in home textile industries. We can enhance the efficient utilization of apparel cut wastes recycled fibres by using it to develop high performance composite panels and the unitization and consumption of various natural resources for new composite panel manufacturing can be minimized.

Reinforcement and matrix are the two distinct structural elements of composite materials [6-8]. While integrating different type of materials as reinforcement and matrix, the

To cite this article: Kumar C R, Vidya T, Prakash C, Raja D. 2024. Study and analysis of fibre reinforced textile composites developed by using recycled viscose and polyester fibres from apparel industry cut panel wastes. *Tekstil ve Konfeksiyon,* 34(3), 191-199.

composite material structure would display better functional characteristics than individual and separate components [9-11]. Two or more components of materials with dissimilar physical and chemical properties are combined to create composites [12]. Different new novel materials for composite development are preferred for numerous reasons, such as materials that are stronger, lighter, or more affordable when compared to conventional composite materials [13]. One of the best ways to utilize recycled fibres for various end uses and high-performance applications is to create composite materials utilizing recycled natural and synthetic fibre [14]. Apparel cut panel waste from apparel manufacturing industry can be used to make these recycled fibres. In a variety of applications, including automotive and structural composites, natural and synthetic fibres are already used as successive reinforcing elements [15]. Fiber reinforced polymer composites are typically made by reinforcing glass, carbon, aramid, and wood fibres with a matrix of epoxy, polyester thermosetting plastic, and phenol formaldehyde resins for high-performance applications in the aerospace, automotive, marine, and construction industries [16]. The major purpose of this study is to create composite materials from apparel cut wastes to match and replace the structural materials and applications that rely on wood products. The recycling of clothing cut wastes to create high-performance products and the reduction of the use of wood for various commercial products such partition boards, doors, furniture items, electrical switchboards, and fall roofing are the main needs for these current project studies [17].

Reinforcement fibres can be extracted and individualized from apparel cut wastes by using willowing machine technique. The iron spikes on the inside of a large drum in willowing machines separates, individualizes, and free the fibres from the apparel cut waste fabric panels. Then, to acquire the various properties of the finished composite, the loosening fibres can be organized in various orientations and bonded with various matrices. To keep the reinforcement in the proper orientation within the composite structure, many types of matrices can be utilized as resins. The reinforcement fibres and matrices form a link that improves protection against external and chemical attacks and successfully transfers applied loads to the entire composite structure. In this research, an effort has been made to create a composite material employing several types of matrices and recycled fibres from viscose and polyester apparel cut wastes [18].

2. MATERIALS AND METHODS

2.1. Materials

Epoxy resin, kaolinite, and polypropylene sheet are used as matrices in the development of composites, which are reinforced with recycled fibres extracted from apparel cut wastes that are 100% viscose, 100% polyester, 50/50%

viscose/polyester blend. 100% viscose, 100% polyester, and blends of 50% polyester and 50% viscose apparel cut fabric wastes were collected from apparel industries in south India. The willowing machine was used to turn the collected apparel cut fabric panel wastes into fibres. Recycled viscose, polyester, and viscose/polyester fibres were used to make needle-punched nonwoven textiles, which were then used as reinforcements in composite materials. Kaolinite (clay powder), polypropylene (120 gsm, 0.2 mm thickness) sheets, and epoxy resin (Tensile strength 80MPa, Glass transition Tg: 124.22°C) sheets were chosen as matrices for the development of composite samples. Kaolinite, a dioctahedral phyllosilicate clay, is a mineral commonly found in a soft and earthy form, often exhibiting a white coloration. It possesses a relatively low shrink-swell capacity as well as a low cation-exchange capacity, typically falling within the range of 1 to 15 meq/100 g. The formation of kaolinite primarily occurs through the process of chemical weathering, specifically the breakdown of aluminum silicate minerals like feldspar [20]. Within the domain of composite samples, the term "ratio" denotes the relative proportion of reinforcement material to matrix material employed in the fabrication of the composite. It signifies the ratio of these components in the composite's composition, which can be quantified in terms of weight, volume, or other suitable units of measurement, as dictated by the requirements of the composite manufacturing procedure. As mentioned in Table 1, four distinct types of composite samples were created in each ratio using various combinations and compositions of reinforcement and matrices.

2.2. Methods

The composites were developed using three different types of matrices (epoxy resin, kaolinite and polypropylene) and four distinct ratios of reinforcement (viscose, polyester, and polyester/viscose). Recycled fibres were used directly as reinforcements for the first and second ratio of sample preparations, and needle-punched nonwoven fabrics manufactured from recycled fibre were used as reinforcements for the third and fourth ratio of sample preparations. The composites were created using a compression moulding machine with high volume and pressure. A composite material was developed utilizing the unipolymer model high-pressure compression molding machine. As shown in Table 1, the reinforcement and matrices were mixed and stacked in various ratios. Then, it was compressed at a pressure of 50 kg/cm2 and at the temperature as specified in Table 1 in the compression moulding machine. The compressed composites were taken after 30 minutes of compression from the machine and left for 24 hours.

Table 1. Reinforcement vs matrices ratio, fibre components and Proportions samples with sample code

S. No	Sample Ratios	Sample Code	Reinforcement fibre (Recycled)	Sample components	Compression moulding Temperature &weight/sq.ft
1.	**RATIO - I** Reinforcement1: matrices 3.	V1	Viscose fibre 100%	1. Fibre RF-57g (RF-Reinforcement) 2. Kaolinite MT - 35g (MT-Matrice) 3. Epoxy MT - 135 g 4. Hardener - 16g- for better compression	135°C & 243g
2.		P1	Polyester fibre 100%		135°C & 243g
3.		PV1	Polyester/Viscose fibre blend 50/50%		135°C & 243g
4.	**RATIO - II** Reinforcement 1: matrices 3.	V2	Viscose fibre 100%	1. Fibre RF - 131 g 2. Kaolinite MT - 110 g 3. Epoxy MT - 284 g 4. Hardener - 20 g - better compression	135°C & 525 g
5.		P2	Polyester fibre 100%		135°C & 525 g
6.		PV2	Polyester/Viscose fibre blend 50/50%		135°C & 525 g
7.	**RATIO - III** Reinforcement 1: matrices 3. Three reinforcement layers were arranged among the four matrices layers.	V3	Viscose fibre 100%	1. Fibre RF - Needle punched non-woven fabric-30 g - 3 webs - 12 g/each lay 2. PolyPropylene sheet MT- 350 denier 8 sheets were used as 4 layers (2 sheets per lay)	160°C & 70 g
8.		P3	Polyester fibre 100%		160°C & 70 g
9.		PV3	Polyester/Viscose fibre blend 50/50%		160°C &70 g
10.	**RATIO - IV** Reinforcement 1: matrices 3. Matrice coating was applied to the top and bottom of the reinforcement.	V4	Viscose fibre 100%	1. Fibre RF - Non-woven fabric (Needle Punched) - 37 g 2. Epoxy MT - 72 g - 2 coatings top and bottom with 37 g/coating 3. Hardener - 4 g – for better compression	135°C &150 g
11.		P4	Polyester fibre 100%		135°C & 150 g
12.		PV4	Polyester/Viscose fibre blend 50/50%		135°C & 150 g

*V-Viscose, P-Polyester, PV- Polyester/Viscose, R**F**-Reinforcement, MT-Matrices

Figure 1.a Top surface view of recycled fibre reinforced composite sample

Figure 1.b Cross sectional view of recycled fibre reinforced composite sample

To evaluate and analyze the technical performance and properties of the twelve distinct developed composite samples shown in Table 1, tests for tensile strength, flexural strength, impact strength, and water absorbency were carried out. To assess the technical characteristics of composites, thickness, mass per unit area, and fracture surface are also examined. Prior to testing, all samples were prepared conditioned at the standard room temperature of

23°C and relative humidity of 62%. Five specimens were tested for each sample, and the findings were displayed as the average of those specimens.

2.2.1. Tensile strength

The force necessary to break composite specimens is measured using the ASTM D3039 tensile testing procedure, and the findings are presented as tensile strength in MPa. Universal testing equipment with a load cell capacity of 500 KN and a speed of 20 cm/min was used to conduct the tensile tests. The thickness of the sample varies from 2 mm to 8 mm, and the specimen size for tensile testing is a constant rectangular cross-section, measuring 25 mm width by 250 mm length.

2.2.2. Flexural Strength Test

Flexural testing evaluates a material's strength when a force is applied perpendicular to the sample's longitudinal axis. Flexural strength, a mechanical property of a material also known as modulus of rupture, bending strength, or fracture strength, is described as a material's capacity to withstand deformation under load. According to ASTM D 790 standards, the flexural test was performed on the universal strength testing apparatus. Flexural strength is expressed in kg/sq.cm. The specimen size is 3.2mm x 12.7mm x 125mm for measuring flexural strength.

2.2.3. Impact Strength Test

The Charpy impact test, commonly referred to as the Charpy V-notch test, is a standardized high strain-rate test that quantifies how much energy a material absorbs prior to fracture. A material's capacity to sustain a high-energy impact without breaking or cracking is impact strength. In the Charpy impact strength tester, the test was conducted in accordance with ASTM D6110-10 standard. The pendulum was released to calibrate the apparatus before the test samples were placed to it. The force needed to break the test samples was then released from the freely swinging pendulum while the test samples were held horizontally in a vice. The machine's calibrated scale was used to read the angle the pendulum had swung before the test sample was broken, which corresponded to the amount of energy used to break the sample. KJ/m2 is the unit used to measure impact strength.

2.2.4. Water Absorbency Test

The test was conducted in accordance with ASTM D570 standard. Rectangular specimens with dimensions of 15x2.5 cm were constructed in order to assess the water absorption properties of the composites. The samples were conditioned at 23°C and 62% relative humidity before being weighed. Weight was measured using a high accuracy electronic weighing balance. The dried, weighted samples were submerged in water for a whole day. The specimens are then taken out, dried with a lint-free cloth, and weighed. Samples were once more submerged in water for a week before being removed and weighed to analyze the long-term water absorbency characteristics of composites. Similarly, the cycle was repeated for 1.5 months (6 cycles). With the help of these findings, the sample's water absorption capacity over a specified period to determine its water absorption characteristics. The formula shown below was used to compute the specimen's increased weight.

$$\text{Water absorbency} = \frac{\text{(Final weight – Original weight)}}{\text{Original weight}} \times 100 \ (\text{Unit is \%})$$

2.2.5. Scanning Electron Microscope (SEM)

Using a JEOL JSM 5400 high-resolution SEM image, the morphology and microscopy of composite samples were examined. To prevent charging under the electron beam, the specimen was mounted on a stub and coated with a thin layer of gold using a sputter coater before analysis. With different magnification levels, such as x50, x60, x100, x110, x250, x300, and x700, the findings are obtained as an image of a morphological representation of the developed composites.

3. RESULTS AND DISCUSSION

3.1 Thickness and Mass per unit area

The results are shown in Table 2 for the thickness and mass per half square foot of created composite samples. The findings demonstrate that the thickness and mass per unit area are always directly proportional to the ratios of reinforcement and matrices. As a result, the ratio of reinforcement to matrices has a significant impact on the technical characteristics of composites.

Table 2. Composite sample thickness and mass per unit area

Sample Ratio code	Samples	Avg. Thickness in mm	Avg. Weight in g
I	V1	5	257.9
	P1	5.2	258.12
	PV1	5.1	258.01
II	V2	7.4	527.15
	P2	7.5	528.02
	PV2	7.4	527.8
III	V3	1.1	71.43
	P3	1.2	71.77
	PV3	1.1	71.52
IV	V4	2.8	154.69
	P4	2.7	156.74
	PC4	2.8	154.7

3.2 Tensile Strength

The tensile strength analysis of reinforced composite samples comprising polyester, viscose, and

polyester/viscose blends is depicted in Figure 2. Upon careful observation and analysis of the results, it is evident that samples PV1 and PV2, belonging to ratios I and II, respectively, exhibit significantly higher tensile strength compared to all other samples. This notable enhancement can be primarily attributed to the superior cohesion and bonding achieved between the epoxy resin and kaolinite matrices and the fiber reinforcement utilized in these samples. The robust interfacial bonding plays a crucial role in determining the overall tensile strength of the composite. In the same ratio categories (I and II), sample P1 demonstrates superior tensile strength due to the inherent bonding nature between the synthetic resin and the 100% synthetic polyester fibers employed. Furthermore, sample P3 exhibits commendable tensile strength, mainly attributed to the enhanced bonding between the PP sheet and the polyester fiber reinforcement.

Conversely, samples V4, P4, and PV4 demonstrate lower tensile strength compared to the other samples. This discrepancy can be attributed to the utilization of pure epoxy resin as the matrix and needle-punched non-woven fabric as the reinforcement in these samples. The needle-punched non-woven fabric possesses a tightly packed structure that inhibits the complete penetration of the epoxy resin. Furthermore, it should be noted that the samples V4, P4, and PV4 lack the incorporation of the kaolinite matrice component. As a result, the bonding between the reinforcement and the matrices remains moderate, leading to a comparatively lower tensile strength. In contrast, the other samples benefit from the direct incorporation of loosely mixed fibers with the matrices, facilitating a stronger bond between the constituents. This comprehensive analysis highlights the critical role of matrix-reinforcement compatibility and interfacial bonding in determining the tensile strength of composite samples. The findings underscore the significance of carefully selecting and optimizing the reinforcement materials, matrices, and their respective ratios to achieve superior mechanical properties in composite structures.

3.3 Flexural Strength

Figure 3 illustrates a comparison of the flexural strength exhibited by composite samples reinforced with viscose, polyester, and polyester/viscose fibers. The results reveal that the V2 composite material achieves the highest flexural strength value of 145.03 MPa, surpassing all other samples. This superior performance can be attributed to a higher proportion of reinforcement and matrix composition, as well as an optimized blending process that greatly influences the flexural strength of the composite material.

Sample V1 also demonstrates a commendable flexural strength value of 107.32 MPa, ranking second among all the samples tested. This outcome can be attributed to the utilization of the same material and composition as V2, highlighting the significance of consistent reinforcement and matrix selection. The data analysis suggests that the cohesion and bonding between the reinforcement fibers and the kaolinite and resin matrices significantly contribute to the overall flexural strength of the composite samples. The superior cohesion and bonding characteristics observed in these samples play a vital role in enhancing flexural strength. These findings underscore the importance of selecting appropriate reinforcement materials, optimizing their composition and blending process, and ensuring strong interfacial bonding between the constituents.
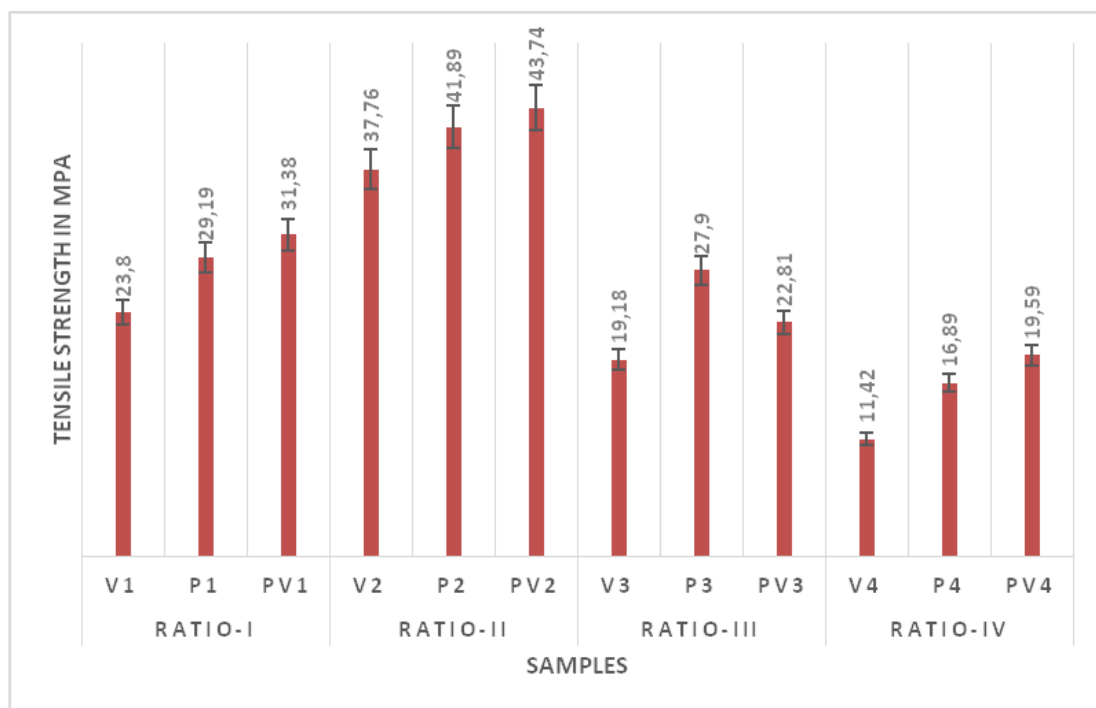
Figure 2. Comparison of tensile strength between viscose, polyester and polyester/viscose blended composites
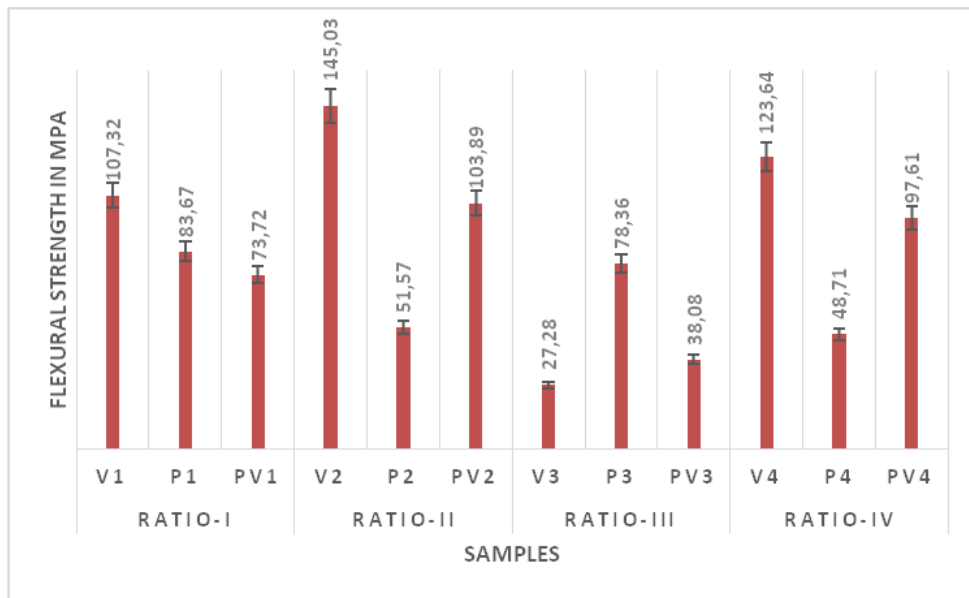
Figure 3. Comparison of flexural strength between viscose, polyester and polyester/viscose blended composites

3.4 Impact Strength

The impact strength analysis, as depicted in Figure 4, reveals important insights into the performance of composite samples reinforced with viscose, polyester, and polyester/viscose fibers. Among the samples tested, PV1, consisting of epoxy and kaolinite as matrices, exhibits the highest impact strength. This superior performance can be attributed to the specific composition of PV1, which incorporates 50% synthetic polyester fiber as the reinforcement material. The synthetic polyester fibers possess a higher crystalline content, enabling improved bonding with the synthetic epoxy resin matrix. This enhanced interfacial bonding contributes significantly to the overall impact strength of the composite sample PV1. Furthermore, the impact strength of sample P3 is also found

to be satisfactory. In this case, both the reinforcement material and the matrices are synthetic in nature, thereby facilitating effective bonding within the composite structure. This bonding mechanism plays a vital role in enhancing the impact strength performance of the P3 sample.

These findings highlight the crucial role of reinforcement-matrix compatibility and interfacial bonding in determining the impact strength of composite materials. The presence of synthetic materials, such as polyester fibers and epoxy resin, fosters stronger bonding and, consequently, improved impact strength. The results underscore the significance of carefully selecting and optimizing the composition of reinforcement materials and matrices to enhance the impact strength of composite structures.
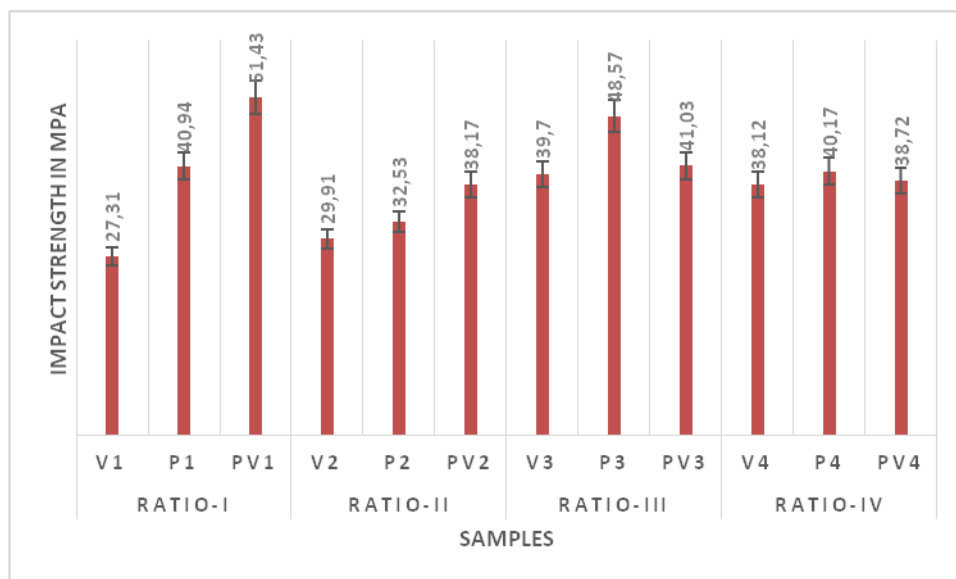

Figure 4. Comparison of impact strength between viscose, polyester and polyester/viscose blended composites

3.5 Water Absorption

The water absorbency percentage of the reinforced composite samples, as illustrated in Figure 5, provides valuable insights into their water absorption characteristics. Notably, samples P1, P1, P2, and P4 demonstrate lower water absorption levels from the initial 24 hours up to 1008 hours. Comparative analysis reveals that these samples exhibit reduced water absorption when compared to all other samples tested. The low water absorption observed in samples P1, P2, P3, and P4 can be attributed to several factors. Firstly, the close packing and reduced porosity within the composite structure, facilitated by the presence of epoxy and kaolinite matrices, contribute to the lower water absorption. These matrices provide a barrier against water penetration, limiting the ingress of moisture into the composite. Additionally, these samples are composed of synthetic polyester fibers, which possess lower moisture regain properties compared to other fibers used in the samples. The inherent characteristics of synthetic polyester fibers, including their hydrophobic nature and lower affinity for water, further contribute to the reduced water absorption observed in these samples.

These findings emphasize the importance of matrix selection, porosity control, and fiber composition in managing water absorption in composite materials. The incorporation of epoxy and kaolinite matrices, along with the use of synthetic polyester fibers, aids in minimizing water uptake, thereby enhancing the composite's resistance to moisture.

3.6 Scanning Electron Microscope (SEM)

Figure 6 exhibits the morphological representation of the composite samples at different magnification levels, offering visual evidence of the uniform distribution and adhesive nature of the matrices and reinforcements within the composites. The morphological analysis confirms that the PV sample series, incorporating two different fiber blends and matrices, demonstrates superior cohesion between the reinforcement and matrices when compared to other samples. The morphological images validate the successful integration and dispersion of the reinforcement materials within the matrix, indicating a well-blended composite structure. The uniform distribution of the fibers throughout the matrix signifies effective interfacial bonding, resulting in enhanced mechanical properties.

4. CONCLUSION

The primary objective of this research was to explore the potential for high-performance applications of recycled fiber reinforced composites. Experimental investigations were conducted to evaluate key properties such as tensile strength, flexural strength, impact strength, water absorption and SEM analysis. A total of twelve composite samples were tested, incorporating varying types and quantities of recycled fibers as reinforcement, along with different matrices in varying ratios. The results of the study revealed that polyester/viscose fiber reinforced composites exhibited superior tensile strength compared to other recycled fiber reinforced samples. These composites can be further tailored to specific application requirements by designing different lay-up angles and orientations, incorporating various preformed layers of reinforcements. The versatility of these composite materials extends to structural applications, including thermal and acoustic insulation. By utilizing recycled garment cut wastes, the scope of recycling can be expanded, allowing for increased utilization of these composites. This not only contributes to resource conservation but also offers potential benefits in terms of reduced cost and weight of the composites. Overall, this research highlights the promising potential of recycled fiber reinforced composites in high-end performance applications. Further research can focus on optimizing the composition and manufacturing processes to enhance the mechanical properties and explore additional functional attributes of these composites.
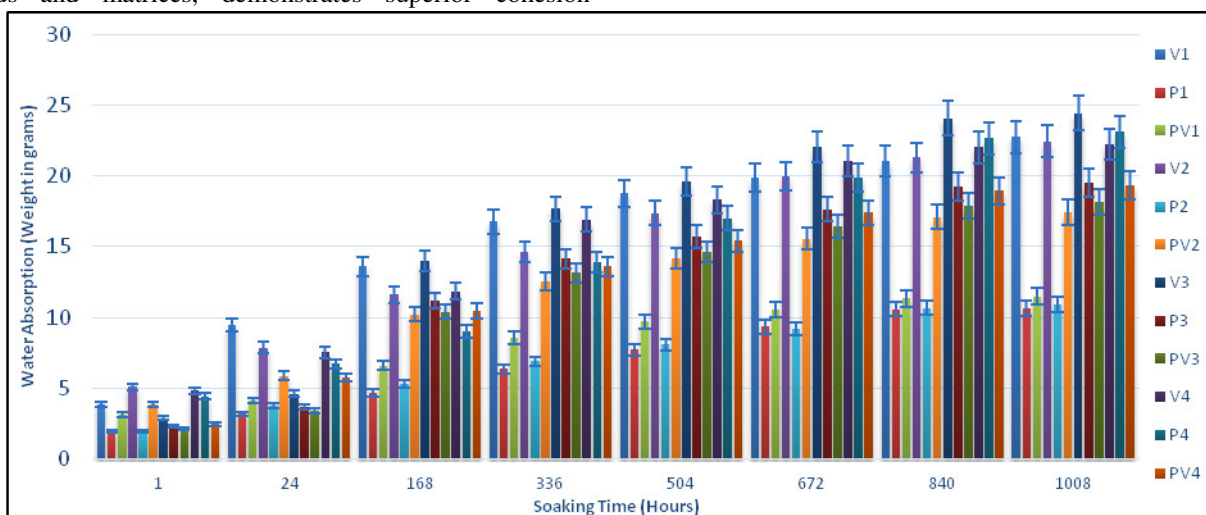
Figure 5. Comparison of water absorption between viscose, polyester and polyester/viscose blended composite samples
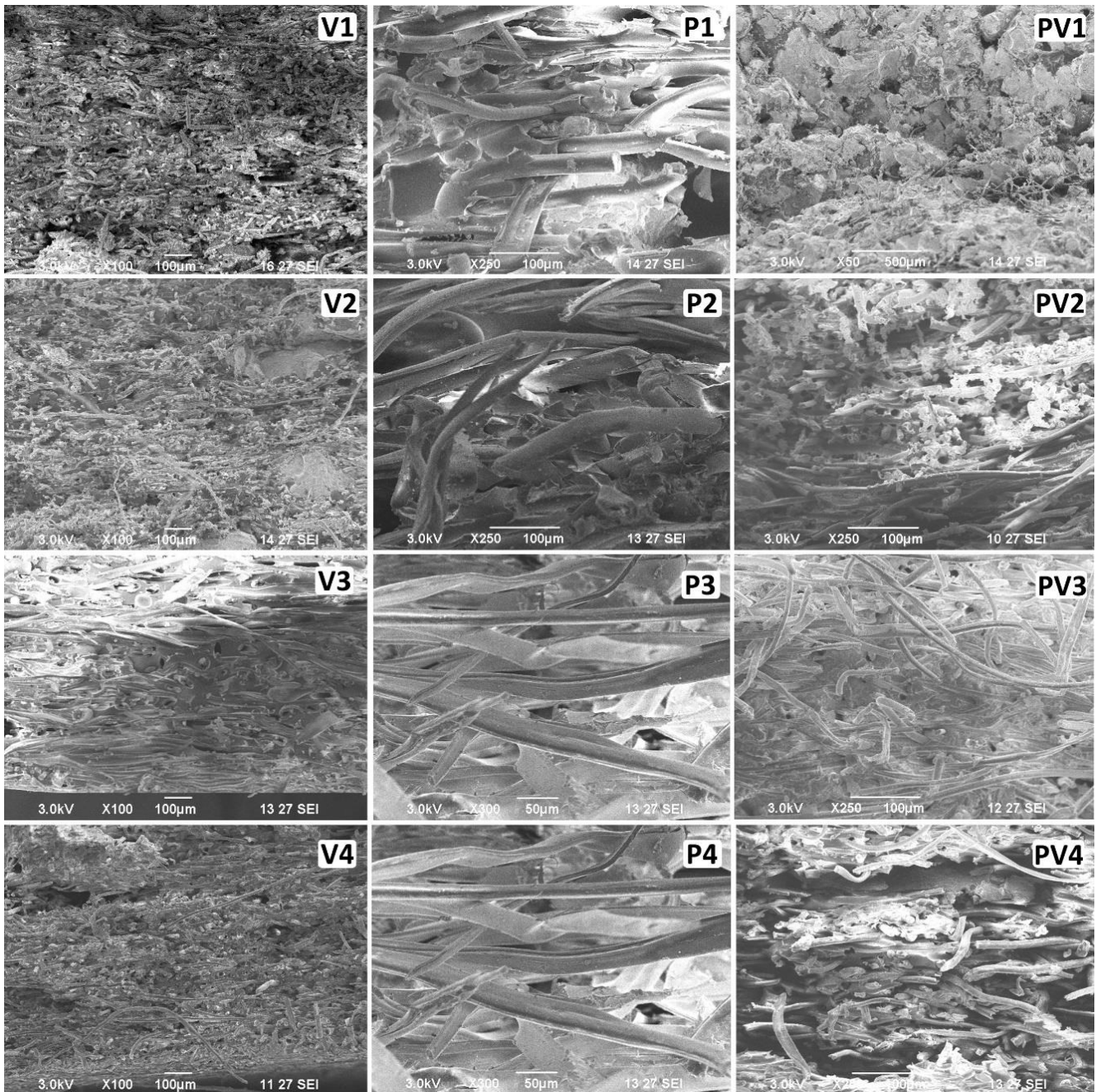
Figure 6. SEM images of different composite samples

REFERENCES

1. Bhatia D, Sharma A, Malhotra U. 2014. Recycled fibers: an overview. *International Journal of Fiber and Textile Research* 4(4), 77-82.

2. Spadea S, Farina I, Carrafiello A, Fraternali F. 2015. Recycled nylon fibers as cement mortar reinforcement. *Construction and Building Materials* 80, 200-209.

3. Muralidhar BA, Giridev VR, Raghunathan K. 2012. Flexural and impact properties of flax woven, knitted and sequentially stacked knitted/woven preform reinforced epoxy composites. *Journal of Reinforced Plastics and Composites* 31(6), 379-388.

4. Borg RP, Baldacchino O, Ferrara L. 2016. Early age performance and mechanical characteristics of recycled PET fibre reinforced concrete. *Construction and Building Materials* 108, 29-47.

5. Bandung K, Hambalang K, Suratno D, Prama Y, Suroso I, Dewi R, Subur M. 2016. Impact of different sorts of marker efficiency in fabric consumption. *International Journal of Textile Science* 5(5), 96-109.

6. Vasconcelos G, Lourenço PB, Camões A, Martins A, Cunha S. 2015. Evaluation of the performance of recycled textile fibres in the mechanical behaviour of a gypsum and cork composite material. *Cement and Concrete Composites* 58, 29-39.

7. Bhatia D, Sharma A, Malhotra U. 2014. Recycled fibers: an overview. *International Journal of Fiber and Textile Research* 4(4), 77-82.

8. Bledzki AK, Gassan J. 1999. Composites reinforced with cellulose based fibres. *Progress in Polymer Science* 24(2), 221-274.

9. Petrucci R, Nisini E, Puglia D, Sarasini F, Rallini M, Santulli C, Minak G, Kenny JM. 2015. Tensile and fatigue characterisation of textile cotton waste/polypropylene laminates. *Composites Part B: Engineering* 81, 84-90.

10. Broda J, Slusarczyk C, Fabia J, Demsar A. 2016. Formation and properties of polypropylene/stearic acid composite fibers. *Textile Research Journal* 86(1), 64-71.

11. Verma D, Gope PC, Shandilya A, Gupta A, Maheshwari MK. 2013. Coir fibre reinforcement and application in polymer composites. *Journal of Material Environmental Science* 4(2), 263-276.

12. Abtew MA, Boussu F, Bruniaux P, Loghin C, Cristian I. 2019. Ballistic impact mechanisms–a review on textiles and fibre-reinforced composites impact responses. *Composite Structures* 223, 110966.

13. Lau KT, Hung PY, Zhu MH, Hui D. 2018. Properties of natural fibre composites for structural engineering applications. *Composites Part B: Engineering* 136, 222-233.

14. Won JP, Jang CI, Lee SW, Lee SJ, Kim HY. 2010. Long-term performance of recycled PET fibre-reinforced cement composites. *Construction and Building Materials* 24(5), 660-665.

15. Spadea S, Farina I, Carrafiello A, Fraternali F. 2015. Recycled nylon fibers as cement mortar reinforcement. *Construction and Building Materials* 80, 200-209.

16. Rahman MR, Huque MM, Islam MN, Hasan M. 2009. Mechanical properties of polypropylene composites reinforced with chemically treated abaca. *Composites Part A: Applied Science and Manufacturing* 40(4), 511-517.

17. Sinha AK, Narang HK, Bhattacharya S. 2017. Mechanical properties of natural fibre polymer composites. *Journal of Polymer Engineering* 37(9), 879-895.

18. Dixit S, Goel R, Dubey A, Shivhare PR, Bhalavi T. 2017. Natural fibre reinforced polymer composite materials-a review. *Polymers from Renewable Resources* 8(2), 71-78.

19. Nils Malmgren A. B., 2009, *Epoxy Plastic General Chemical and Physical Properties*,

20. Charles Weaver, 1974, *Chemistry of Clay Minerals,* Adam Hilger Ltd, England.

Some Comfort Properties of Spacer Fabrics from Recycled and Umorfil Polyamide Fibers for Sportswear Applications

Berna Karabulut 0000-0002-9609-0316
Banu Nergis 0000-0001-6010-6497
Cevza Candan 0000-0003-2007-5758

Technical University of Istanbul, Textile Engineering Department, Gumussuyu, Istanbul, Turkiye

Corresponding Author: Banu Nergis, uygunf@itu.edu.tr

ABSTRACT

Sportswear, the clothing including footwear, worn during sports or physical exercise, has an increasing demand and the sports apparel with improved comfort properties have become more popular than ever. Enhancing the wearer's comfort is possible by engineering fabric structures by incorporating suitable fibers. For doing so, in this study, bilayered spacer fabric samples were produced from sustainable fibers namely, recycled PA66 and PA6-Umorfil yarns, together with 44 dtex elastane. A PA6 FDY monofilament yarn was employed as the spacer yarn. The results showed that comfort properties of sports apparel can be improved by using recycled and Umorfil poliamide fibers in different parts of the garments depending on the intended use and purposes. Use of such sustainable fibers in the fabric structure is not only suitable for achieving active sportswear comfort but also is respectful to the environment.

1. INTRODUCTION

Textiles have been used for centuries to meet apparel and domestic needs. Conventional textiles are used for common applications and decorative or aesthetic purposes. Technical Textile, on the other hand, is the term which refer to technical and high-performance, high-added-value products for particular end-use rather than conventional ones [1,2]. Sports textiles are a sub-branch of technical textiles and also one of the high-performance apparel used to protect the human body during sports. Sports clothing, particularly the base layer of the garments which are next to the skin, are important for providing the thermo-physiological comfort of a person and for keeping their performance high [3,4]. In all kinds of sports, which mainly are winter sports, summer sports, outdoor games, indoor games, football, cricket, climbing, cycling, flying and sailing sports, athletics, etc, several textile materials are used having different functionalities [5].

Users' main problems when using sportswear are considered as sweating, feeling hot during exercise, low stretching ability, extra weight of the fabric, injuries during falling, excessive movements, hard contact with the ground [3, 5, 6]. Depending on the type of the sports activity, the human body produces about half to one liter of sweat per hour. Sportswear apparel is expected to absorb and simultaneously disperse heat and moisture to achieve a high level of comfort [7]. Major performance requirements for sportswear are listed as follows:

- High comfort properties, easy to wear, good handling,
- Good thermal properties; cool in summer, warm in winter,
- Lightweight, high elasticity, good compressibility, movement freedom,
- Good moisture management, remove and distribute the moisture from the body and quick dry,
- High perspiration fastness, high strength and durability, good abrasion resistance,
- Easy-care
- Good skin-care; protect skin from UVA, UVB, anti-bacterial, and gentle feeling to skin.

Both natural (e.g. cotton, wool) and man-made fibers (widely polyester and, nylon, acrylic, elastane) are used in sportswear and a wide variety of woven, knitted and nonwoven fabrics are commercially available. These

fabrics' performance vary depending on the entrapped air, pore shape and size, volume and surface properties, etc. Hence, knitted fabrics are widely preferred for sportswear since they have more elasticity and stretching properties compared to woven ones, providing vast freedom of movement. In general, sportswear fabrics are made from single-layer knitted fabrics.

There are studies which focus on moisture related comfort properties of single layered fabrics, in the form of plain jersey, plaited jersey, single pique, honeycomb, from natural, synthetic and regenerated fibers [8, 9,10, 11]. Çeven and Günaydın also studied the comfort and mechanical properties of single jersey fabrics from various regenerated cellulosic fibres, among which Umorfil fiber took place [12]. They observed that the knitted fabrics made of Umorfil® yarns indicated the lowest thermal conductivity and provided the maximum air permeability.

Knitted fabrics made of cotton are considered comfortable when used under normal conditions while the ones from polyester, nylon, polypropylene and acrylic are suitable for strenuous activities because they do not retain moisture and therefore do not get heavy upon sweating like cotton does. Besides polyester, which is popular and commonly used in active wear and sportswear, nylon is also often used in sportswear because it is durable and easy to care for, dries quickly and, does not hold onto sweat or odor. Nylon, being a lightweight fiber, is an ideal option to stay comfortable and cool under hot weather conditions. These characteristics of nylon fibre make it preferable to be used in sportswear applications. [13,14]. Developments in synthetic fibre processing have opened up broad possibilities for their use in sportswear and speciality nylon fibres such as Hygra fibre, which is a core-sheath type of filament yarn composed of a water absorbing polymer and nylon, Killat N (from Kanebo Ltd.) a nylon hollow filament, Naiva yarn which is composed of 55% Eval and 45% nylon have been engineered [15]. Recycled nylon is also a preferred fiber in the production of sportswear. The reduced energy consumption for the production of the fibre, the reduced dependence on oil and the possibility of recycling the final product at the end of its life are the main benefits of recycling nylon [16]. Protection of skin against bacteria, and gentle feeling to skin also offer a high level of comfort and personal hygiene during sports activities. Umorfil N6U is a new generation sustainable protein fiber that is obtained by integrating the purified collagen peptide (amino acid) from waste fish scales with regular nylon 6 polymerization technology. The bionic nylon fiber is claimed to have better moisture regain in comparison to regular nylon, in addition to some other properties such as good hand-feeling with deep dyeable features, natural cooling effect, anti-UV function, and skin friendliness [17].

Spacer fabrics comprise two layers that are joined together and kept apart by a spacer yarn which is mostly monofilament. The distant placing of the outer surfaces creates a ventilated layer that results in good moisture and thermal performance. Spacer fabrics also provide an advantage of having low weight in proportion to their large volume [18]. The unique structure of spacer fabrics fulfills the expectations from sportswear by offering good thermal and moisture management properties as well as lightweight, high elasticity, good compressibility.

In order to meet so many aforementioned features expected from sportswear, the right fiber and structure choice such as layered (bi-layer and/or tri-layer) fabrics, is of utmost importance. In Table 1, a summary of the studies that focused on comfort properties of layered structures, namely knitted spacer fabrics, is presented.

As the literature survey suggests (Table 1), there is lack of study on multi-layered knitted structures from sustainable synthetic fibers such as recycled and Umorfil Nylon for sportswear though spacer fabrics have the potential to meet the main performance requirements for sportswear. Accordingly, the work under discussion aimed to investigate the effect of recycled and Umorfil nylon fibers in the design and development of spacer fabrics for sportswear applications.

2. MATERIAL AND METHOD

2.1 Material

78/60x1 dtex, S and Z twisted, Recycled-PA66 textured yarn (P), which was obtained from Fulgar with the relevant traceability certifications, and 78/72 dtex, and S and Z twisted, Umorfil PA6 (N6U) textured yarn (U) were used for knitting either both or one side of the spacer samples. In order to prevent the spirality problem, one S and one Z twisted yarn was placed onto the knitting machine creel consecutively. A 22/1 dtex PA6 FDY monofilament yarn was employed as the spacer yarn and a 44 dtex elastane was used while knitting front and back sides of the samples. Based on the preliminary works of the study, elastane yarn was introduced to the samples not only to facilitate efficient knitting process but also to enhance dimensional stability of the spacer fabrics. The fabric samples produced are composed of 72% recycled PA or Umorfil PA, 22% elastane, and 6% PA monofilament.

2.2 Method

The samples were produced on a Mayer & Cie Relanit 28 fine circular interlock knitting machine that is 30 inches in diameter and is equipped with 92 feeders. During the production, 90 systems were used such that 30 feeding systems were reserved for front yarns, 30 systems were employed for back and elastane yarns and finally 30 systems were used for the spacer yarn. The stitch notation of the samples is given in Figure 1.

Table 1. Studies on comfort properties of knitted spacer fabrics

Reference	Weft Spacer Fabric	Warp Spacer Fabric	Fiber Types	Air Permeability	WVP*	Drying Rate	Wicking/Wetting/ MMT	Thermal Properties
[19]		✓	Polyester (PET), meta-aramide	✓	✓			✓
[20]	✓		Polypropylene (PP), PET, viscose				✓	✓
[21]	✓		Cotton, Bamboo, high performance fiber	✓	✓			✓
[22]	✓		PET, Poliamide, Polypropylene micro filaments, soy fiber, cotton	✓	✓			✓
[23]	✓		PET	✓	✓			✓
[24]		✓	PP, PET	✓	✓			✓
[25]	✓		PET	✓	✓			✓
[26]		✓	PET, cotton, elastane			✓	✓	
[27]		✓	PET	✓	✓			✓
[28]		✓	PET		✓			
[29]	✓		Viscose, modal, bamboo, PP, micro-fiber PET and PET				✓	
[30]	✓		PET, PP, Cotton				✓	
[31]	✓		PET, PP, Cotton	✓	✓			✓
Current work	✓		Recycled PA, Umorfil	✓	✓	✓	✓	

* Water Vapour Permeability
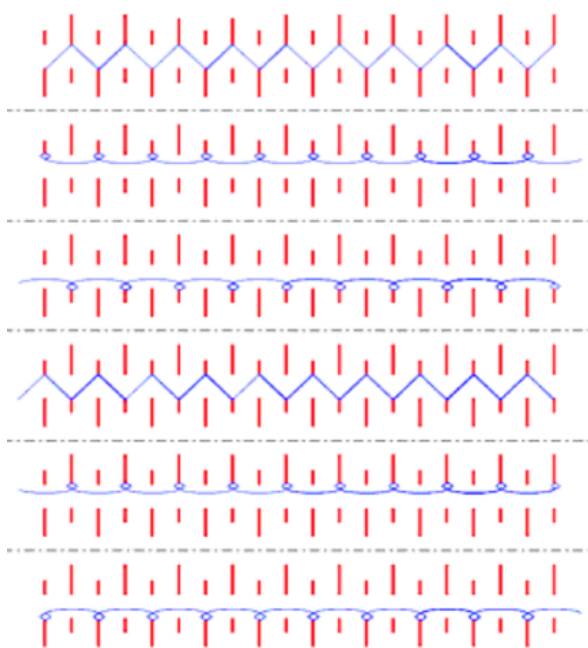
Figure 1. Stitch notation of the samples (adapted from [32])

The Recycled-PA66 textured yarn and the N6U-Umorfil textured yarn were used on both sides of the spacer samples or only on one of the sides (Table 2).

The samples were pre-washed, heat set and dyed under the following commercial conditions:

• Washing at 80 °C with wetting agents.

• Heat-setting in 10 chambers stenter machine at 90 °C for 45 sec.

• Dying in Beam Dyeing Machine at 102 °C for both Umorfil and Recycled-PA66 dyeing process.

All the tests, both for the greige and dyed fabrics, were conducted after conditioning the samples under standard atmospheric conditions (20 °C ±2, 65 % ±5%).

Coding of the samples are given in Table 2 where;

P, U, G, and D are for the recycled PA66 textured yarn, the PA6-Umorfil textured yarn, the greige fabrics, and the dyed fabrics, respectively.

Yarn count, breaking force and elongation of the yarns were tested in accordance with ISO 2060 and ISO 2062 standards, respectively. Course and wale densities were measured with a counting glass as described in TS EN 14971. Weight of the fabrics were determined according to TS EN 12127 standard. Thickness measurements were taken under a pressure of 20 g/cm^2 using R&B Cloth Thickness Tester according to ISO 5084.

When it comes to the fabric bulk density, it was calculated using equation 1 [33]. The porosity of the spacer samples was determined according to the equation 2. For the calculations, the density of the fibers employed i.e. PA, Recyled PA 66 and Umorfil PA were taken as 1,14 g/cm^3, elastane density 1,3 g/cm^3.

Table 2. Coding of the samples

Fiber Content	Greige Fabric	Dyed Fabric	Explanation
Recycled-PA66/ Recycled -PA66	PPG	PPD	Both sides of the spacer are from Recycled-PA66 yarn.
Umorfil / Umorfil	UUG	UUD	Both sides of the spacer are from Umorfil yarn.
Recycled -PA66 / Umorfil	PUG	PUD	One side of the spacer is from Recycled-PA66 yarn and the other side is from Umorfil. The front side is considered as the Recycled-PA66 side.
Umorfil / Recycled -PA66	UPG	UPD	One side of the spacer is from Recycled-PA66 yarn and the other side is from Umorfil. The front side is considered as the Umorfil side.

Bulk density (g/cm^3) = Areal density (g/m^2) /Thickness (t) (1)

Porosity (%) = [1-Fabric density (g/cm^3) /Filament density (g/cm^3)] x 100 (2)

Air and water vapor permeability tests were carried out on a 20 cm^2 test area with 200 Pa pressure according to ISO 9237 and according to BS 7209:1990 standards, respectively. During the water vapor and air permeability tests, for the PU samples, the fabric layer from Recyled PA66 was considered as the outer side whereas the layer from Umorfil was considered as the inner side of the structure. While testing the UP samples, the fabric sides were reversed.

The vertical wicking tests were applied in both course and wale directions. For the tests, 5 mm of the samples (25 mm x 200 mm) were immersed in distilled water and the rising height of the water on each side of fabric is recorded after 1 min, 5 min, 10 min, 15 min, 20 min, 25 min, and 30 minutes.

So far as evaluating transverse (lateral) wicking behavior is concerned, Sampath et al.'s approach was employed such that each sample of 10 cm diameter was mounted on an embroidery frame and 1 ml of water was dropped on the fabric surfaces with the help of a burette placed 6 mm above the surface of the fabric to measure the spreading area [34].

Contact angle of all the samples were measured using Cam 101 contact angle goniometer (KSV INSTRUMENTS). To determine the drying rate of the fabrics, similar method used by Coplan and Fourt et al. has been used [35,36].

As a final note, the analysis of variance (one way ANOVA) was used to determine the significance of the yarn combination and moisture related comfort qualities at a 95% confidence level by using IBM SPSS (Version 28) Statistical software package.

3. RESULTS AND DISCUSSION

The tested properties of the yarns and fabrics are given in Tables 3 and 4.

As may be seen in Table 3, the yarns used for knitting both layers of the spacer structure were of the same yarn count and had similar tenacity properties which means that all the samples can be knitted using the same knitting parameters.

Table 3. Yarn Properties

Yarn Type	Yarn Count dtex-(CV%)	Tenacity cN/Tex-(CV%)	Elongation %-(CV%)
Recycled-PA66 S	76-(1)	37-(3)	30,76-(9)
Recycled-PA66 Z	77-(1)	35-(2)	29,63-(6)
Umorfil-PA6 Z	76-(1)	38-(3)	39,57-(6)
Umorfil-PA6 S	77-(1)	37-(3)	31,15-(4)
Monofilament PA6	19-(3)	38-(5)	51,28-(17)
Lycra	44	-	-

Table 4. Fabric properties

Samples	Course Density (courses/cm)	Wale Density (wales/cm)	Stitch Density (loops/cm^2)	Weight (g/m^2)	Thickness (mm)	Bulk density (g/cm^3)	Porosity (%)
PUG	21,6	41	902,9	404	1,36	0,293	60
UPG	21,6	41	902,0	404	1,36	0,293	60
UUG	21,8	41	902,9	405	1,34	0,298	60
PPG	22,2	41	915,8	391	1,35	0,291	60
PUD	**21,7**	**32,8**	**711,8**	**347**	**0,69**	**0,508**	**42**
UPD	**21,7**	**32,8**	**711,8**	**347**	**0,69**	**0,508**	**42**
UUD	**21,6**	**32,0**	**682,4**	**335**	**0,68**	**0,490**	**42**
PPD	**21,7**	**31,6**	**694,5**	**346**	**0,65**	**0,536**	**40**

A comparative study of greige and dyed fabric properties showed that stitch density, weight and thickness of the samples significantly decreased after the finishing and dying processes (Table 4). This is mainly due to the stentering process which is used to fix the dimensions of the samples. Accordingly, bulk density of the samples, being the measure of fabric weight per unit volume, increased and in turn influenced the porosity values of the dyed samples. The t-test analysis conducted for the bulk density and porosity values of each fabric group (i.e. the greige and dyed samples) revealed that there is no statistically significant difference in 95% confidence limit among the samples. This enabled the comparative study of the influence of fiber type on moisture related properties of the samples.

Air Permeability

Air permeability of the samples are presented in Figure 2.

Generally speaking, fabrics' comfort properties are determined by the air circulation between the inter-yarn voids to greater extent, and accordingly the yarn type has a significant impact on how permeable a fabric is to air. As may be seen from Figure 2, irrespective of greige or dyed, the samples having Umorfil layers on both sides had the highest air permeability performance. The finer filaments in the Umorfil yarns may result in more inter-yarn voids that in turn influence the air flow through these pores. One way ANOVA test conducted to investigate the effect of yarn type on air permeability did confirm that irrespective of the processes applied, the air permeability performance of the samples are significantly effected by the yarn type employed for the work (Table 5).
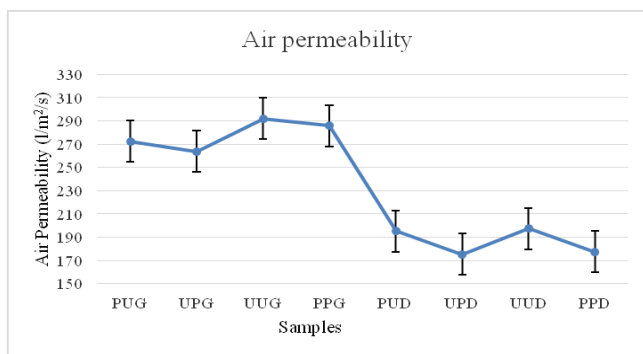

Figure 2. Air permeability of samples

The fabric's air permeability is also highly influenced by the fabric weight, porosity, and thickness. The results (Figure 2) showed that the air permeability of the greige samples was recorded to be higher than that of the dyed ones, which might be due to their higher porosity and lower density values. The air permeability performance of the dyed samples, however, markedly dropped despite the fact that they are much thinner than the corresponding greige ones (Table 4 and Figure 2).

Finally, for both the greige and dyed samples, the layer facing the air flow appears to determine the air permeability of the spacer structure. When the Umorfil layer (i.e. PU samples) faced the air flow during testing, slightly higher air permeability values were displayed than the ones for UP samples. This result is also compatible with the findings of Çeven & Günaydın who found that the dyed Umorfil sample in their study provided the highest air permeability while this was not the case for the greige ones [11]. Thus, it might be suggested that the fabric layer from Umorfil can be used as the outer side in a sportswear clothing to contribute its comfort properties.

Water Vapour Permeability

Water vapour permeability of the samples are presented in Table 6. As is well known, since the water vapor permeability is an indication of the ability of fabrics to transfer water vapour from the skin to the outer surface, it is regarded as one of the most important moisture related comfort properties. And the better WVP, the higher wearer's comfort is. As may be seen from table 6, the dyed samples demonstrated higher WVP performance than the greige ones did, and among all of the fabrics the PUD sample gave the highest WVP. A comparative study of the WVP results of the dyed samples with their air permeability ones depicted an opposite behaviour such that the air permeability of the dyed samples is much lower than that of the greige ones (Figure 2). Unlike water vapor that diffuses through not only the air spaces among the yarns but also through the structure of the fibres via free convection, air permeability takes place in the form of forced convection and hence the relatively higher porosity of the greige fabrics may have been good for air transport in these fabrics.

Table 5. One-Way ANOVA results for Air Permeability

	Sum of Squares	df	Mean Square	F	Sig.*
Between Groups	73087,218	6	12181,203	35,714	0,000
Within Groups	9550,210	28	341,079		
Total	82637,428	34			

*p value for 95 % significance ≤ 0.05

Table 6. Water Vapor Permeability results

Samples	Water Vapor Permeability (g/m²/day)
PUG	5119
UPG	5211
UUG	4903
PPG	5161
PUD	**6100**
UPD	**5406**
UUD	**5594**
PPD	**5556**

Water vapour transmission depends on the moisture absorption capacity and hygroscopic properties of the constituent fibres [37]. Umorfil® N6U is a bionic nylon fiber with higher moisture regain in comparison to regular nylon fibers. The differences in moisture absorption capacity of the fibers are expected to influence the water vapour permeability of the samples. For the greige fabrics, the lowest water vapour transmission was recorded for the UU fabrics whereas for the dyed ones the UPD sample showed the lowest performance. Mishra et. al claimed that the main points of water vapour permeability results were the wetting and wicking properties of fiber type and there were no correlation between air permeability and water vapour permeability [38]. Rajan et. al stated in their study that WVP behaviour of spacer fabrics was correlated with wicking behaviour [28]. In that respect, the WVP of the Umorfil samples that had the highest and faster wicking behavior, appeared to be in aggrement with the findings of the literature. Finally, irrespective of the processes applied on the fabrics (e.g. dying) one way ANOVA analysis showed that yarn type was an effective factor on water vapour permeability for the samples.

Vertical Wicking

Vertical wicking performance of the samples in coursewise and walewise directions are given in Figure 3 and 4, respectively. As may be seen from the figures, the wicking height for all of the samples increased sharply until the end of 20 minutes, which slightly decelerated for the last 10 minutes of the test. The data given in Figure 3 and 4 shows that independent of the testing direction, the wicking heights measured from the greige samples have been higher, when compared to those from the dyed samples. This might be due to the higher porosity, thickness and lower bulk density of the greige samples. Also, as far as the greige samples are concerned, the horizontal placement of spacer yarn, i.e. PA6 monofilament, in the middle layer appears to be influencial on the coursewise wicking performance in particular. The results also revealed that the dyed samples depicted higher wicking rates in the walewise direction, though such a tendency was not observed for the greige ones. This may suggest that the stentering (or heat-setting) as well as dyeing process, could generate more continual and less torturous pore paths in the samples which in turn caused higher capillarity in the dyed samples.

The results obtained for the samples reflected the contribution of fiber properties to the wicking behavior of the fabrics such that irrespective of the test direction, the UU fabrics, having Umorfil PA6 on both layers had the highest wicking performance, whereas the PP samples presented the lowest one. Also the PU and UP samples, layers of which were knitted from r-PA66 and Umorfil PA6, consistently showed higher wicking heights on their layers containing Umorfil PA6. The samples in which both the front and back side of the fabric is made of the same fibre, the wicking heights are comparable for both sides. During wicking, water flows through inter-fiber spaces in the yarn by the interfacial tension between the liquid and the fiber surfaces. So, the rate of wicking not only depends on the spaces among the fibers in the yarn and but also on the surface energy of the fiber [34]. Higher number of filaments in the Umorfil yarns might have resulted in higher capilarity in the yarn structure. Also, Umorfil fibers seem to contribute to vertical wicking performance due to its inherent properties. One way ANOVA analysis also demonstrated that the fiber type was statistically significant factor on vertical wicking ability of the samples (Table 8).

Table 7. One-Way ANOVA results for Water Vapour Permeability

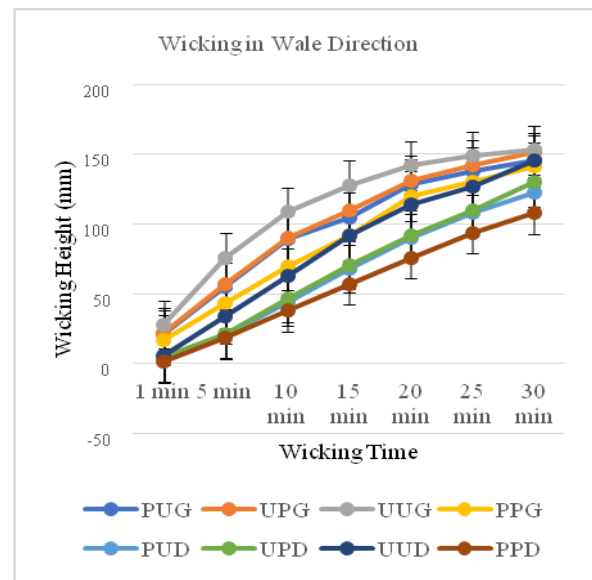|	Sum of Squares	df	Mean Square	F	Sig.
Between Groups	3184946,720	7	454992,389	5,890	0,002
Within Groups	1235939,700	16	77246,231		
Total	4420886,420	23			
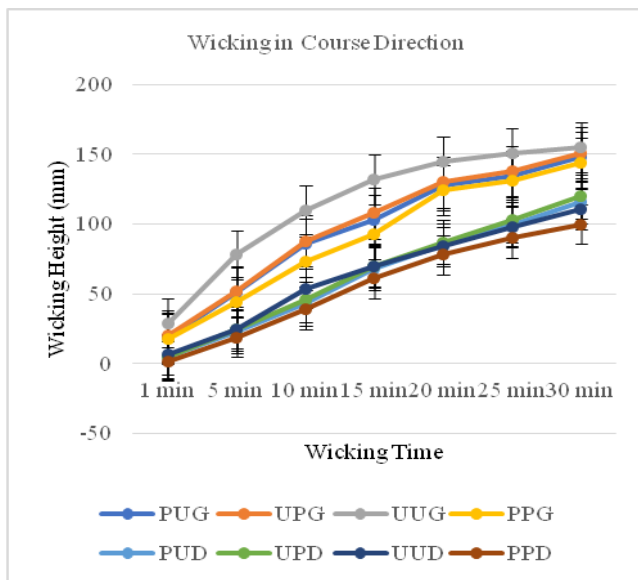
Figure 3. Vertical wicking of the samples in coursewise direction

Figure 4. Vertical wicking of the samples in walewise direction

Table 8. One-Way ANOVA results for vertical wicking of the samples

Coursewise direction					
	Sum of Squares	df	Mean Square	F	Sig.
Between Groups	5571,292	7	795,899	32,431	0,000
Within Groups	392,667	16	24,542		
Total	5963,958	23			
Walewise direction					
	Sum of Squares	df	Mean Square	F	Sig.
Between Groups	5156,958	7	736,708	35,504	0,000
Within Groups	332,000	16	20,750		
Total	5488,958	23			

Transverse Wicking

Transverse (lateral) wicking of fabrics is important because the perspiration transfer from skin involves the movement of sweat through the thickness of the fabric in the lateral direction. The transverse wicking results of the samples are given in Figure 5 and 6. Contact angle measurements are also presented in Table 9.

As may be seen from figure 5, the water absorption time is much shorter for the greige samples than that for the dyed ones, which indicated that the moisture is transferred fast between the top and bottom layers. Furthermore, the UU samples gave the shortest absorption time, which was followed by the other Umorfil PA6 containing samples (e.g. UP and PU). As a final note regarding the greige samples, the wetting areas measured from the Umorfil containing layers of the PU and UP samples were larger than the ones from the PP sample. The fibres' water holding capacities (Umorfil PA6 fibers 7,8 %, PA6 fibers 4,7%), together with the fabric properties (i.e areal density, thickness, etc.)

(Table 4), appeared to influence the wetting time of both the top and bottom surfaces as individual or in interaction. Also, the higher porosity of the samples contributed to the fabrics' transverse wicking performances. The relatively lower contact angles (Table 9) of the UPG and UUG samples, did support the aforementioned interpretations.

Table 9. Contact angle results

Samples	Contact angle (∘)
PUG	110
UPG	56
UUG	55
PPG	94
PUD	**97**
UPD	**84**
UUD	**82**
PPD	**96**
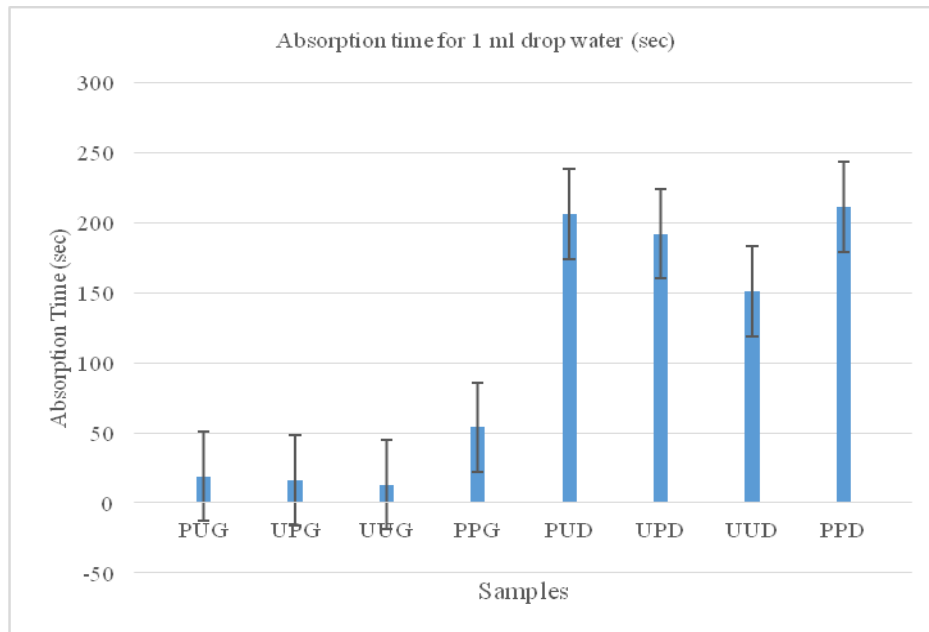
Figure 5. The time needed to absorb 1 ml of water by the samples
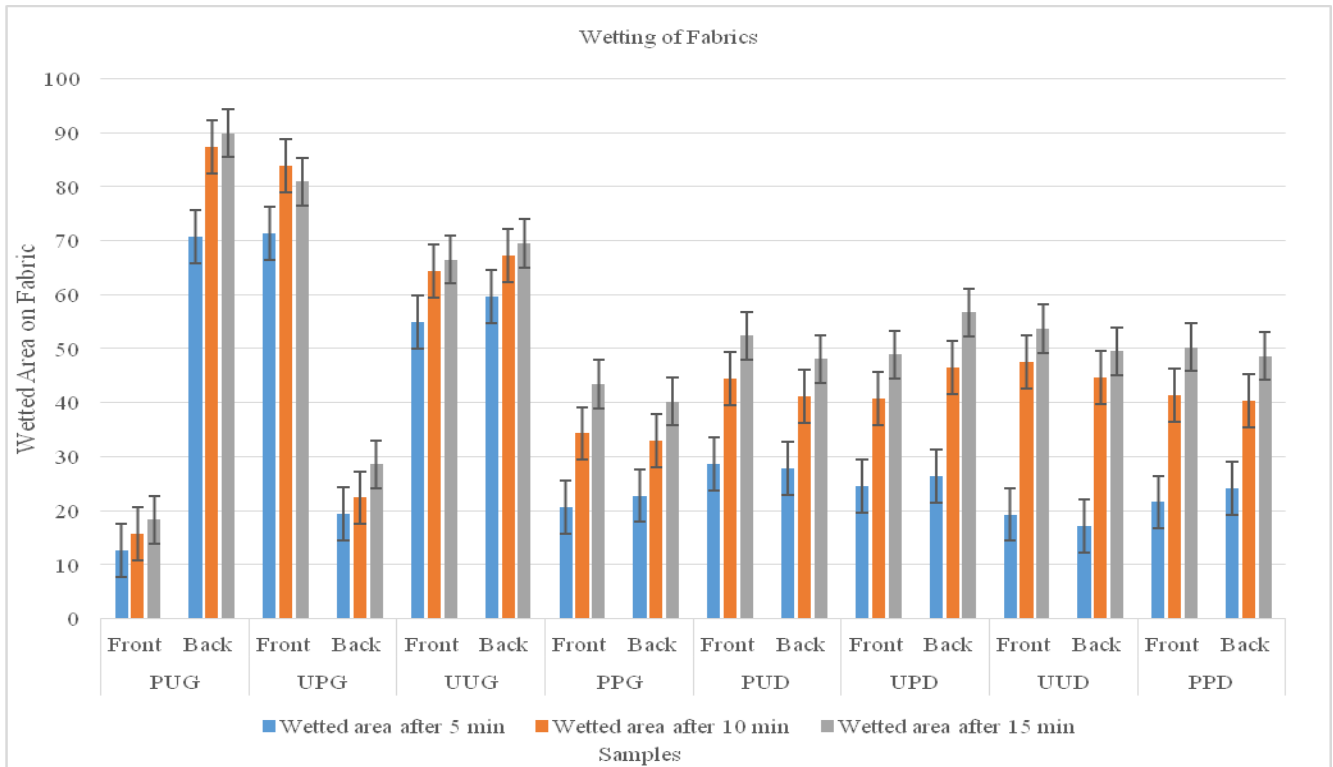
Figure 6. Wetted area on the front and back layers of the samples

Table 10. Drying rate of the samples

Samples	Thickness (mm)	Dry sample (g)	Wet Sample (g)	Drying Rate (g/m²/h)
PUG-UPG	1,35	4,04	8,61	114
UUG	1,3	4,07	8,63	113
PPG	1,4	3,91	8,17	137
PUD-UPD	**0,69**	**3,47**	**6,66**	**108**
UUD	**0,71**	**3,33**	**6,69**	**112**
PPD	**0,63**	**3,41**	**6,04**	**87**

When it comes to the transverse wicking performance of the dyed fabrics, a significant increase in the water absorption time was observed, though the UU sample still had the lowest absorption time (Fig.5). The lower porosity (Table 4) values of the dyed samples implied that the heat-setting and dyeing processes altered pore geometry, volume, and distribution in the relevant layers such that the distance of liquid advancement was limited. These processes may also have lowered the surface tension of the samples as also may be seen from the contact angle measurements. It was also noted that depending on the time, the Umorfil PA6 content in the layers of the dyed samples (e.g. PU, UP) appeared to have a positive impact on the wetted area, in comparison to the PP samples. The relatively finer Umorfil PA6 filaments in the samples may have higher surface tension which facilitates holding the water droplet and transfer it in the lateral direction against gravitational force. These filaments may also have enhanced higher water absorbency as a result of more inter-fibre space helping water better spread laterally. Finally, using the fibers having big differences in moisture affinities (i.e. r-PA 66 and Umorfil PA6) together in the structures appeared to prove as effective means for enhancing the transverse wicking properties of the knitted fabrics because the dyed PU and UP samples consistently gave larger wetting area than UU samples (Fig.6).

Drying Rate

Table 10 shows the drying rates of the samples, and from which it can be seen that the PU, UP, and UU samples absorbed more water that the PP ones, as was expected.

Among all of the fabrics, the PPG sample gave the highest drying rate, whereas the PPD one showed the lowest, which indicated that the samples initially absorbing more water tended to have higher drying rates. Also, thickness is an influential parameter for drying performance of the samples. Moreover, considering the fact that all of the dyed samples dried within 3 hours, the Umorfil contained samples held more water and evaporated faster. This may be due to higher rate of capillary migration in the relevant samples (e.g. UUD, PUD, etc.) (Figure 3-4). As is discussed in the literature, continuous liquid distribution owing to capillary migration is effective in the drying process [35,36,39-41]. According to one way ANOVA analysis, yarn type was found to be a statistically significant factor on drying ability of the samples (Table 11).

4. CONCLUSION

This study mainly focuses on the effect of the yarns from the sustainable fibers, namely Recycled-PA66 and Umorfil Polyamide (i.e. r-PA 66 and Umorfil PA6), and their composition on moisture management and air permeability properties of the spacer knitted structures for sportswear applications. These fabrics were developed such that different yarn compositions on front and back layers (e.g. r-PA 66 on the front and Umorfil PA6 on the back) were employed. Accordingly, the most important results were given as follows:

1. Generally speaking, dyeing and finishing processes did affect the properties of the fabrics.

2. Regarding the air permeability results of both the dyed and greige samples, the ones from Umorfil PA6 allowed slightly higher air permeability than those from r-PA66, which suggests that the Umorfil PA6 containing layer may be employed as the outer layer of the clothing for better air circulation performance.

3. Umorfil PA6 fibers, whether greige or dyed, have proved to be superior in terms of vertical wicking of water due to mostly its inherent properties that would ease the removal and distribute the moisture from the body.

4. Since Umorfil PA6 containing layers of the fabrics have the fastest water absorption time, irrespective of the fact that the fabric is greige or dyed, it may be suggested that the water absorption rate of hydrophobic surfaces, as in the case of the fabric layers from r-PA66, can be improved by including Umorfil PA6 based fibers into bilayered structures.

5. It appears that the approach suggested in clause 4 can be an effective way for enhancing the transverse wicking properties of the fabrics which in turn reduces the wetness feeling when r-PA66 has been used for the inner layer of the structures.

6. Giving consideration to the fact that all of the dyed samples dried within three hours, the Umorfil PA6 containing fabrics (e.g. PUD, UUD) hold more water and evaporates the absorbed moisture to the environment well through the outer layers, which makes them favorable alternatives for the intended application area, namely sportswear apparels.

Table 11. One-Way ANOVA results for vertical wicking of the samples

	Sum of Squares	df	Mean Square	F	Sig.
Between Groups	3407,333	7	486,762	8,891	0,000
Within Groups	876,000	16	54,750		
Total	4283,333	23			

7. The PA6 mono filament spacer yarn, having low affinity to absorb moisture, seems to facilitate rapid transport of moisture in the structures.

The findings of the study indicated that moisture related comfort properties of spacer knitted fabrics for sporting activities can be improved by using r-PA66 and Umorfil PA6 yarns in the inner and outer layers, respectively. However, further research is needed to engineer alternative spacer fabrics from the aforementioned sustainable fibers by focusing on both sports activity and garment types.

REFERENCES

1. McCarthy, B.J. 2016. An overview of the technical textiles sector. In Horrocks A. R., Anand S.C. (Eds). *Handbook of technical textiles*, pp.120.

2. Paul, R. (Ed.). 2019. *High performance technical textiles*. John Wiley & Sons.https://doi.org/10.1002/9781119325062.

3. Rasheed, A. 2020. Classification of Technical Textiles. In: Ahmad, S., Rasheed, A., Nawab, Y. (Eds) *Fibers for Technical Textiles. Topics in Mining, Metallurgy and Materials Engineering*. Springer, Cham. https://doi.org/10.1007/978-3-030-49224-3_3.

4. Kumar, C.S., Kumar, B.S., Rachel, D.A. 2020. Comfort aspects of sportswear base fabrics: a review. *Journal of Emerging Technologies and Innovative Research*, 7(2), pp.1071-1076.

5. Uttam, D. 2013. Active sportswear fabrics. International Journal of IT, *Engineering and Applied Sciences Research*, 2(1), pp.34-40.

6. Jhanji, Y. 2021. Sportswear: Acumen of Raw Materials, Designing, Innovative and Sustainable Concepts. *Textiles for Functional Applications*, 261.

7. Senthilkumar, M., Sampath, M. B., Ramachandran, T. 2012. Moisture Management in an Active Sportswear: Techniques and Evaluation— A Review Article. *Journal of The Institution of Engineers* (India): Series E, 93(2), 61–68.

8. Choudhary, A. K. 2020. The influence of yarn and knit structure on moisture management properties of sportswear fabric. *Journal of The Institution of Engineers* (India): Series E, 101, 77-90.

9. Soydan, A. S., Karakan Günaydin, G., Ergezer, H., Palamutcu, S. 2021. Moisture management and antimicrobial performance of collagen peptide enriched knitted fabrics. *The Journal of The Textile Institute*, 112(7), 1023-1036.

10. Suganthi, S., Pachiayappan, K. M., Priyalatha, S., Prakash, C. 2023. A Comparative Study on Moisture Management Properties of Natural and Manmade Cellulosic Fabrics Produced from Plain and Its Derivative Knitted Structures. *Journal of Natural Fibers*, 20(1).

11. Duru, S. C., Göcek, İ. 2020. Assessing Water-Related Comfort Performance of Knitted Fabrics made of Rayon Microfibers and Lyocell Fibers for Intimate Wear. *Tekstil ve Konfeksiyon*, 30(3), 220-230.

12. Çeven, E. K., Günaydın, G. K. 2021. Evaluation of Some Comfort and Mechanical Properties of Knitted Fabrics Made of Different Regenerated Cellulosic Fibres. *Fibers and Polymers*, 22(2), 567–577.

13. Sathish Babu, B., Senthil Kumar, P., Senthil Kumar, M. 2020. Effect of yarn type on moisture transfer characteristics of double-face knitted fabrics for active sportswear. *Journal of Industrial Textiles*, 49(8), 1078-1099.

14. Ahmad, F., Akhtar, K. S., Anam, W., Mushtaq, B., Rasheed, A., Ahmad, S., ... & Nawab, Y. 2023. Recent Developments in Materials and Manufacturing Techniques Used for Sports Textiles. *International Journal of Polymer Science*, Volume 2023 | Article ID 2021622 | https://doi.org/10.1155/2023/2021622.

15. Chowdhury P., Samanta K. K., Basak S. 2014. Recent Development in Textile for Sportswear Application, *International Journal of Engineering Research & Technology* (IJERT) Volume 03, Issue 05.

16. McCann, J. 2015. Environmentally conscious fabric selection in sportswear design. In Shishoo R. (Ed.). *Textiles for sportswear* (pp. 17-52). Woodhead Publishing.

17. Umorfil launches new revolution in Nylon 6. (n.d.). Retrieved December 27, 2022, from https://www.umorfil.com/download/future_textiles_Oct.pdf.

18. Chinta, S.K., Gujar, P.D. 2013. Significance of Moisture Management forHigh Performance Textile Fabrics. *International Journal of Innovative Research in Science, Engineering and Technology*, 2, 814-819.

19. Arumugam, V., Mishra, R., Militky, J., Davies, L., Slater, S. 2018. Thermal and water vapor transmission through porous warp knitted 3D spacer fabrics for car upholstery applications. *The Journal of The Textile Institute*, 109(3), 345–357.

20. Arunraj A., Thambidurai A., Sundaresan S., Ajithkumar C., Akshaya S., Manikandan K. 2022. Development of Tri-Layered Knitted Fabric For Sports Wear Application, 8(2), *IJARIIE*-ISSN(O)-2395-4396 645-649.

21. Blaga, M., Ciobanu, A. R., Marmarali, A., Ertekin, G., ÇELİK, P. 2015. Investigation of the physical and thermal comfort characteristics of knitted fabrics used for shoe linings.*Tekstil ve Konfeksiyon*, 25(2), 111-118.

22. Buhai, C., Vlad, L., Budulan, C. 2014. Comfort Properties Of Functional Spacer Fabrics. *Bulletin of The Polytechnic Institute of Iaşi*, 1(4).

23. Chen, C., Du, Z., Yu, W., Dias, T. 2018. Analysis of physical properties and structure design of weft-knitted spacer fabric with high porosity. *Textile Research Journal*, 88(1), 59–68.

24. Chen, Q., Shou, D., Zheng, R., Tang, K. P. M., Fu, B., Zhang, X., Ma, P. 2021. Moisture and Thermal Transport Properties of Different Polyester Warp-Knitted Spacer Fabric for Protective Application. *Autex Research Journal*, 21(2), 182–191.

25. Ertekin, G., Marmarali, A. 2011. Heat, air and water vapor transfer properties of circular knitted spacer fabrics. *Tekstil ve Konfeksiyon*, 21(4), 369-373.

26. Liang, X., Yu, X., Dong, Z., Cong, H. 2021. Preparation and moisture management performance of double guide bar warp-knitted fabric based on special covering structure. *Journal of Engineered Fibers and Fabrics*, 16.

27. Muthu Kumar, N., Thilagavathi, G., Periasamy, S. 2022. Development and characterization of warp knitted spacer fabrics for helmet comfort liner application. *Journal of Industrial Textiles*, 51(2_suppl), 2053S-2070S.

28. Rajan, T. P., Souza, L. D., Ramakrishnan, G., Kandhavadivu, P., Vigneswaran, C. 2016. Influence of porosity on water vapor permeability behavior of warp knitted polyester spacer fabrics. *Journal of Industrial Textiles*, 45(5), 796–812.

29. Suganthi, T., Senthilkumar, P. 2018. Moisture-management properties of bi-layer knitted fabrics for sportswear. *Journal of Industrial Textiles*, 47(7), 1447–1463.

30. Udaya Krithika, S. M., Sampath, M. B., Jebastin Rajwin, A., Prakash, C., Senthil Kumar, M., Senthil Kumar, P. 2021. Moisture management properties of bi-layer knitted fabrics. *Fibres & Textiles in Eastern Europe*, 2 (146), 81-86.

31. Babalik, E., Güneşoğlu, S., Ütebay, B., Bakadur, A. Ç., Güneşoğlu, C. 2021. A new objective method for comfort assessment of sportswear knitted fabrics. *Tekstil ve Konfeksiyon*, 31(4), 318-328.

32. Ertekin, G. 2009. Yuvarlak Örme Makinelerinde Üretilen Sandviç Kumaşların Genel Özelliklerinin Araştırılması [Master's thesis]. Ege Üniversitesi.

33. Palani, T. R., Prakash C., Ramakrishnan, G. 2019. An effect of fabrics thickness and structure on moisture management properties of 3D spacer fabrics. *International Journal of Clothing Science and Technology*, 31(6), 777–789.

34. Sampath, M., Mani, S., Nalankilli, G. 2011. Effect of filament fineness on comfort characteristics of moisture management finished polyester knitted fabrics. *Journal of Industrial Textiles*, 41(2), 160–173.

35. Coplan, M. J. 1953. Some Moisture Relations of Wool and Several Synthetic Fibers and Blends. *Textile Research Journal*, 23(12), 897–916.

36. Fourt, L., Sookne, A.M., Frishman, D. and Harris, M. 1951. The rate of drying of fabrics. *Textile Research Journal*, 21(1), pp.26-33.

37. Soares, G. M. B., Magalhães, A., Vasconcelos, A., Pinto, E., Santos, J. G. 2018. Comfort and antimicrobial properties of developed bamboo, polyester and cotton knitted spacer fabrics. *Cellulose Chemistry and Technology*, 1(2), 113–121.

38. Mishra, R., Veerakumar, A., Militky, J. 2016. Thermo-physiological properties of 3D spacer knitted fabrics. *International Journal of Clothing Science and Technology*, 28(3), 328–339.

39. Benltoufa, S., Fayala, F., BenNasrallah, S. 2008. Capillary rise in macro and micro pores of jersey knitting structure. *Journal of Engineered Fibers and Fabrics*, 3(3), 155892500800300305.

40. Laing, R. M., Wilson, C. A., Gore, S. E., Carr, D. J., Niven, B. E. 2007. Determining the drying time of apparel fabrics. *Textile Research Journal*, 77(8), 583-590.

41. Zhuang, Q., Harlock, S. C., Brook, D. B. 2002. Transfer wicking mechanisms of knitted fabrics used as undergarments for outdoor activities. *Textile Research Journal*, 72(8), 727-734.

Multi-Objective Optimization of Selected Mechanical Properties of Basalt, Carbon Fabric Reinforced Particle Additive Composites

Çiğdem Sarpkaya[1] 0000-0001-7710-1035
Ertan Özgür[2] 0000-0001-6293-0690
Emel Ceyhun Sabır[2] 0000-0002-2385-1524

[1] University of Karabuk / Department of Fashion Design / Karabük, Türkiye

[2] University of Cukurova / Department of Textile Engineering / Adana, Türkiye

Corresponding Author: Emel Ceyhun Sabır, emelc@cu.edu.tr

ABSTRACT

In this study, some of the mechanical properties of basalt fabric and carbon fabric reinforced particle additive composite materials were investigated. The effect of fabric additive ratios on tensile strength, Izod pendulum impact resistance, and three point bending properties has been tried to be revealed. In order to determine the composite material that gives the optimum mechanical properties, Taguchi Grey Relational Analysis (Taguchi based GRA) method was chosen as multi-objective optimization method and used L18 (Mixed 3-6 Level) experimental design. Input variables-factors were determined as fabric (6 levels), Al_2O_3 additive (3 levels) and SiC additive (3 levels) according to the design. Tensile strength, impact resistance, and three point bending were selected as response variables. These three tests were optimized. The optimum composite combination was determined and found 30% carbon fabric, 4% Al_2O_3 and 0% SiC. The improvement by using confirmation test was seen as 0,07 when the 3rd experiment plan was selected as the initial process parameter.

1. INTRODUCTION

Today, with the developing technology, materials that are difficult to produce, high cost and high volume have been replaced by materials with greatly increased mechanical properties, lower cost, less volume and lighter. The materials that best meet these properties are composites. The most used materials in composites technology are glass and carbon fibers. Due to their disadvantages people start to investigate new product. One of these materials is basalt fiber. Basalt has no toxic reaction with air and water, it can be found easily in the nature and has a very high resistance against acid and alkali, has a very high strength and can be operated in very high temperature ranges. Basalt fiber-reinforced composites have an increasing utilization rate nowadays. Basalt fibers also can be used as a thermal and sound insulation/protection material. And because of these properties, basalt fibers can be used as fire protection

materials [1]. Basalt fiber reinforced composites show much better properties in tensile, bending and impact tests than e-glass reinforced composites [2]. Recent research showed that they have a good thermal resistance when it is aluminized [3] and the alkali resistance and heat/humidity resistance of epoxy composites from basalt fibers are much greater than those of epoxy composites derived from E- and S-glass fibers [4]. In a study, it was concluded that basalt fiber showed better tensile strength than glass fiber, and the brittleness and brittleness of basalt fiber could be eliminated by adding more flexible fibers to basalt fiber [5]. The results obtained in a recent study pointed out that by Ovalı using of pumice stone as filling material improve thermal and sound properties of basalt composites [6]. Basalt has high elastic modulus, the thermal stability, the resistance to chemical attacks, the sound insulation properties [7]. Liu et al. (2022) were investigated both basalt fibers and glass fibers can be used as reinforced

material in fiber-reinforced polymer composites [8]. In the study, the advantages of basalt fiber over glass fiber were revealed. In a study made by Gumulcine et al (2012) showed that basalt fiber reinforced composites have much better properties in tensile, bending and impact tests than e-glass reinforced composites [9].

Today, with the development of technology and increasing consumption, expectations from composite materials have increased. In order to match with these expectation, nano and micro particles start to be added to the composites such as Al_2O_3, TiO_2, SiC, SiO_2. Nayak et al. (2014) showed that SiO_2 increased flexural strength and flexural modulus more than Al_2O_3, TiO_2 [10]. Agarwal et al. (2013) added different ratio of SiC and found the best rate of SiC to have the best mechanical properties such as Bulut (2018) and Prasanna et al. (2016) [11, 12, 13]. Ramesh et al. (2014) investigated the effect of modification with Al_2O_3 / SiO_2 / TiO_2 on the mechanical properties of glass fiber/epoxy composite [14]. Gün et al. (2017) investigated the effect of the addition of ceramic powder particles (Al_2O_3- TiO_2) on the mechanical properties of glass fiber reinforced epoxy matrix composites [15]. Vaidya and Rangaswamy (2017) tried to find the best additive among Al_2O_3, SiC, B_4C, $Mg(OH)_2$ and various chemical additives [16]. Kaybal et al. (2016) investigated the effect of adding nano Al_2O_3 to the composites' tensile properties [17]. Krzyzak et al. (2022) studied on the impact of the introduction of powder modifier into composite reinforced with carbon fabric on selected mechanical properties. Test results indicated that the increase of alumina content by weight caused the decrease of strength of polymer composites in most tests [18]. Akatsu et al. (2022) examined the mechanical properties, alumina matrix composite reinforced using homogeneously distributed carbon nanofiber [19]. In the study made by Sanusi (2020), the effectiveness of sintered alumina, developed from corundum, as a laminate component of ceramic-steel was investigated [20]. Lin (2020) was studied on the thermal conductivity, Young's modulus and hardness of the composites [21]. In the study by Kim and Park (2021), graphene oxide/graphitic nanofiber nanohybrids (GO-GNFs) were added into an epoxy matrix as a carbon fiber reinforced composite and found promising results [22]. Kim et al. (2020) studied ozone/TEPA-functionalized NDs were added to composite to improve its thermal conductivity and fracture resistance [23]. Ozgur et al (2023) added SiC and Al_2O_3 materials to carbon and basalt composites and to improve their thermal and sound insulation properties [24].

Innovative optimization techniques can be used to reduce test time, number and cost in the engineering experimental design of composite materials. Among these techniques, the Taguchi Method is a widely used technique [25]. In this study, Multi-Objective Optimization Based on Gray Relationship Analysis of this technique was applied.

2. MATERIAL AND METHOD

2.1 Material

The composite material of the study consists of epoxy resin, basalt and carbon fabric reinforcement and Al_2O_3 and SiC particle additives. Basalt and carbon fabrics used for reinforcement in the study are in plain pattern and weight 200 g/m^2. Three different ratios as %30,40,50 are used in fabric reinforcement. These two materials were chosen in order to compare basalt with carbon, which is the strongest material used in this field. Resin type is epoxy and accelerator is cobalt material. The resin accelerator percent ratio is 75:25. Mineral additive materials reinforced to the resin are in the form of SiC (micro powder, 3µm) and Al_2O_3 (nano powder, 28nm). SiC material was used in three different proportions as 0, 5, 10 and Al_2O_3 material was also used in three different proportions as 0, 2, 4. These ratios were decided according to the literature. The additives and the the resin were blended manually. The composite samples were produced with hand lay-up technique. It is known that composite materials are based on the weight ratio of the reinforcing resin.

2.2 Method

In this study, the Taguchi Method based on Grey Relational Analysis was applied as design of experiment (DOE). MINITAB 15 ® package program was used in the application of Taguchi method based on Grey Relational Analysis [26]. Experimental Design L18 (Mixed 3-6 Level) was chosen. Generally, 2- level (L4, L8, L12 and L32) and 3-level (L9, L18, L27) orthogonal arrays are used according to the experimental design. Also, some mixed orthogonal arrays used such as L18, L36, L54. In this study, 3 factors (Input Variables) were selected as fabric, additives (Al_2O_3 and SiC). The fabric factor is 6 levels, Al_2O_3 Additive is 3 levels and SiC Additive is 3 levels. Therefore, the L18 (Mixed 3-6 Level) experiment design was selected suggested by the Taguchi experimental plan. The output parameters (Response Variables) to be optimized were decided as tensile strength, Izod pendulum impact resistance and three point bending properties. Table 1 shows input parameters (factors) and their levels for L18 orthogonal layout (Mixed 3-6 Level). The factor A (Fabric) is 6 level (B30, B40, B50, C30, C40, C50). In the codes in Factor A, B refers to basalt fabric and C refers to carbon fabric. The numbers (30,40,50) next to these letters show the fabric ratio in the composite. Accordingly, for example, B30 refers to 30% basalt fabric reinforcement. The factor B (Al_2O_3 additive) is 3 level (0, 2, 4). The factor C (SiC additive) is 3 level (0, 5, 10). The number of experiments was reduced to 18 with the Taguchi Method used in the study. Table 2 shows experimental plan suggested by Taguchi method. Table 2 contains the codes of experimental plan and the factor levels. For example, experiment 5 means a combination of B40 fabric, 2% Al_2O_3 additive and 2% SiC additive.

Table 1. Factors and their levels for design L18 (mixed 3-6 level)

Factor	Factor Code	Level 1	Level 2	Level 3	Level 4	Level 5	Level 6
Fabric	**A**	B30	B40	B50	C30	C40	C50
Al$_2$O$_3$ Additive, %	**B**	0	2	4	-	-	-
SiC Additive, %	**C**	0	5	10	-	-	-

Table 2. Selected experimental design L18 (mixed 3-6 level, coded)

Experiment No	A (Fabric)	B (Al$_2$O$_3$ Additive)	C (SiC Additive)
1	1 (B30)	1 (0)	1 (0)
2	1 (B30)	2 (2)	2 (5)
3	1 (B30)	3 (4)	3 (10)
4	2 (B40)	1 (0)	1(0)
5	2 (B40)	2 (2)	2 (5)
6	2 (B40)	3 (4)	3 (10)
7	3 (B50)	1 (0)	2 (5)
8	3 (B50)	2 (2)	3 (10)
9	3 (B50)	3 (4)	1(0)
10	4 (C30)	1 (0)	3 (10)
11	4 (C30)	2 (2)	1 (0)
12	4 (C30)	3 (4)	2 (5)
13	5 (C40)	1 (0)	2 (5)
14	5 (C40)	2 (2)	3 (10)
15	5 (C40)	3 (4)	1(0)
16	6 (C50)	1 (0)	3 (10)
17	6 (C50)	2 (2)	1(0)
18	6 (C50)	3 (4)	2 (5)

The hand lay-up method used for composite production has been one of the production methods that has been widely used in low production quantities. This method is the process of giving the shape of the mold for fibres/fabrics placed in a mold with resin with a roller or brush.

After samples were produced according to test plan in Table 2, output parameters were tested. For Tensile Strength Test (MPa), test standard of DIN EN ISO 527-1was used. For Izod Pendulum Impact Resistance Test (kJ/m^2), test standard of ASTM D 256, 2005 was used. For Three Point Bending Test (MPa), test standard of DIN EN ISO 178 was used. Tensile Strength Test was made by the Zwick Roell Z010 test device with 5 mm/min device speed and 0,1 MPa preload, Izod Pendulum Impact Resistance Test was made by Zwick Roell Hit5.5P test device with 5 joule energy, Three Point Bending Test was made by the Zwick Roell Z010 test device with an 8 mm/min device speed. All tests were made in Kahramanmaraş Sütçü İmam University Forest Industry Engineering Department Laboratories (Kahramanmaraş/Türkiye).

2.3 Grey relational analysis method

Grey Relational Analysis allows the optimization of more than one performance characteristics (Output Parameters).

In this study, three mechanical performance parameters were optimized. These are tensile strength, Izod pendulum impact resistance and three-point bending. After application of the method, the method suggests optimum combination for the best three performance characteristics. While applying the Grey Relational Analysis method, the steps are followed respectively and the equations in the table 3 are used.

The steps are

1. Experimental Design and its application

2. Determination of the Reference Series

3. Normalization of data

4. Calculation of the distance matrix of the normalized series to the reference series

5. Obtaining the grey relations coefficient matrix of the series with the distance matrix calculated.

6. Weighting of Normalized Data (W) and Determination of the degree of Grey Relations

7. Determination of new levels of experimental factors,

8. ANOVA test

9. The application of Taguchi Method [27-34].

Steps	Symbols	Equations	
1	Experimental Design and its application		
2	n: experiment number n:1,2....n	$x_0 = (x_0(1), x_0(2), x_0(3), \ldots \ldots, x_0(n))$	(1)
3	For The Larger-The Better $x_i(k)$: After Normalization i. series k. value $x_i^0(k)$: i series k. original value $min\ x_i^0(k)$: Minimum value in i series $max\ x_i^0(k)$: Maximum value in i series k: k. rank in n length of series k=1,2,...,n j=1,2,...m	$x_i(k) = \dfrac{x_i^0(k) - min\ x_i^0(k)}{max\ x_i^0(k) - min\ x_i^0(k)}$	(2)
4	$x_0(k)$: the k. value in reference series $x_j(k)$: k. value in j. value $\Delta_{0i}(k)$: k. value in the series $\varepsilon(x_0(k), x_i(k))$: Grey relational coefficient at point k	$\Delta_{0i}(k) = |x_0(k) - x_j(k)|$	(3)
5	ξ: a coefficient between (0,1) Δ_{min}: Minimum value in the series Δ_{max}: Maximum value in the series $\Delta_{0i}(k)$: k. value in the series	$\varepsilon(x_0(k), x_i(k)) = \dfrac{\Delta_{min} + \xi\Delta_{max}}{\Delta_{0i}(k) + \xi\Delta_{max}}$	(4)
6	$\sum_1^n w_k = 1$ $x_i(k)$: After Normalization i. series k. value x^0: Desired ideal value x_i: m series with comparing x^0 series $\gamma(x_0, x_i)$: Grey relations degree in i. rank w_k: Total weight must be 1	If the effects of the response variables on performance are equal; $\gamma(x_0, x_i) = \dfrac{1}{n}\sum_{k=1}^{n} \varepsilon(x_0(k), x_i(k))$ If the effects of the response variables on performance are not equal; $\gamma(x_0, x_i) = \dfrac{1}{n}\sum_{k=1}^{n} w_k\varepsilon(x_0(k), x_i(k))$	(5) (6)
7	Determination of new levels of experimental factors		
8	ANOVA test		
9	y_i: Experimental results, n: Experiment number η : Grey relations degree predicted by optimum design η_m: Mean grey relations degree η_i: The value of calculated new factor levels in optimum combination	"The Larger-The Better" $s/N = -10log\dfrac{\sum_{i=1}^{n}\frac{1}{y^2}}{n}$ $\eta = \eta_m + \sum_{i=1}^{j} \eta_{i-}\ \eta_m$	(7) (8)

3. RESULTS AND DISCUSSION

3.1. Grey relational analysis method for the study

Composite plates were produced according to Table 2. Mechanical tests were carried out in accordance with the standards. The results of the mechanical tests were given as Figure 1a,b,c **(Step 1)** [35]. It was seen that the combination with the best tensile strength test value was the 9th Experiment, and the worst combination was the 3rd Experiment. It was seen that the combination with the best Izod Pendulum Impact Resistance Test value was the 12th Experiment, and the worst combination was the 1st Experiment. The combination with the best Three Point Bending Test value was the 11th Experiment, and the worst

combination was the 9th Experiment. As can be seen, when the tests are considered separately, the best combination differs.

Step 2. Using Equation 1, determination of the reference series is determined in Table 4, The reference series for three performance output variables are identified as maximum and minimum values.

Step 3. The normalization matrix for outputs is calculated using Equation 2 and calculated values are seen in Table 4.

Step 4. Distance matrix is seen in Table 4 and calculated using Equation 3.

Step 5. Grey relational coefficient matrix is seen in Table 5 and determined with Equation 4.

Step 6: Grey Relational Degree for Outputs were calculated with Equation 5 (Respectively weighted 0,35-0,35-0,30). Grey relational degree and ranking are seen in Table 5. In the table, 12th experiment has the highest grey relational degree.

The Graph of Grey Relational Degree is seen in Figure 2. Grey relation degree of Experiment No. 12 is the highest.

Step 7. New levels of experimental factors are calculated and calculated new factor levels are seen in Table 6. As seen from the table, because differences between levels are biggest, the most effective parameter is factor A (Fabric). Second effective parameter is factor B (Al_2O_3 Additive) and third effective parameter is factor C (SiC Additive)
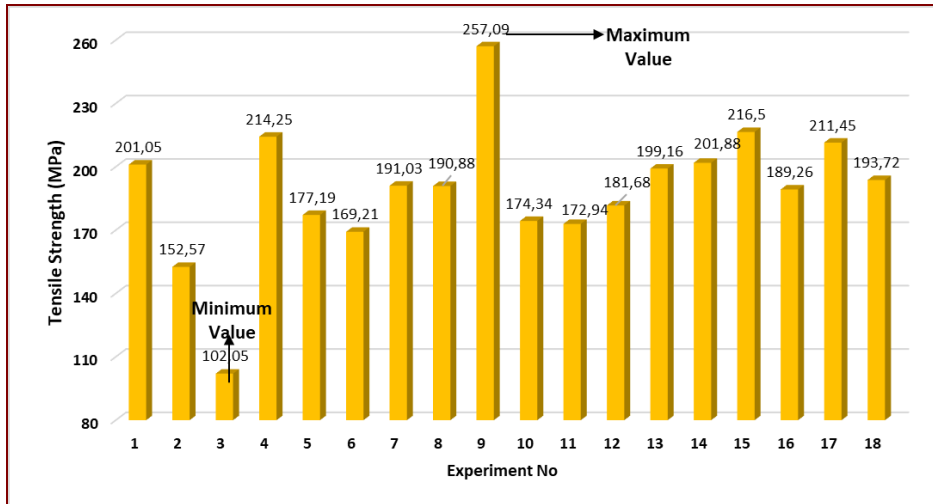
(a)
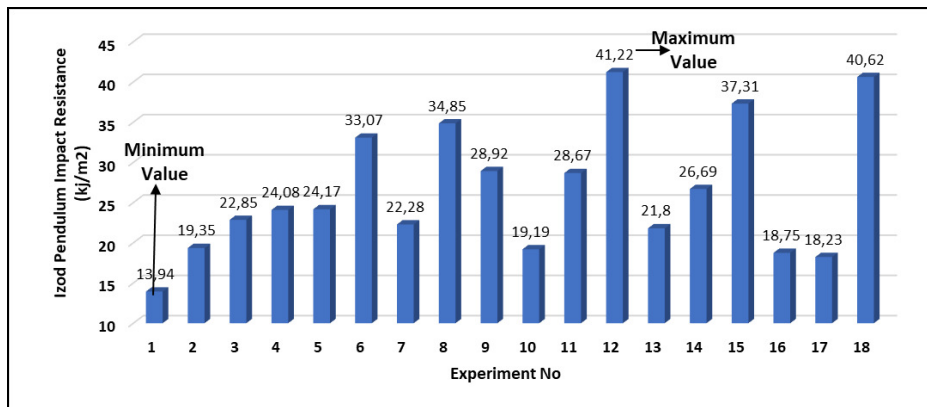
(b)

(c)

Figure 1. Results of experiments for L18 (mixed 3-6 level)

Table 4. Grey relational analysis method for step 2-4

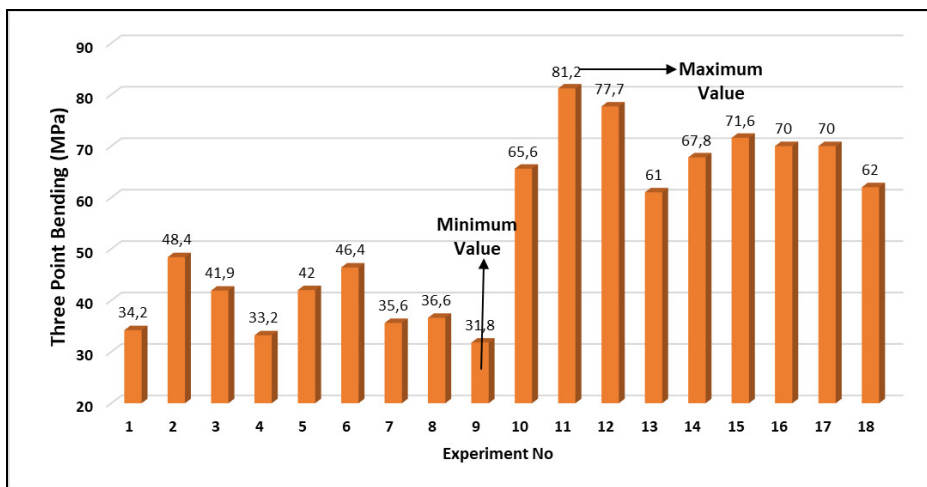|	Reference Series for Outputs			Normalization Matrix for Outputs			Distance Matrix for Outputs		
	Tensile Strength Test (MPa)	Izod Pendulum Impact Resistance (kJ/m²)	Three Point Bending Test Result (MPa)	Tensile Strength Test (MPa)	Izod Pendulum Impact Resistance (kJ/m²)	Three Point Bending Test Result (MPa)	Tensile Strength Test (MPa)	Izod Pendulum Impact Resistance (kJ/m²)	Three Point Bending Test Result (MPa)
Reference Series	257,09	41,22	81,2	1,00	1,00	1,00	1,00	1,00	1,00
1	201,05	**13,94**	34,2	0,64	0,00	0,05	0,36	1,00	0,95
2	152,57	19,35	48,4	0,33	0,20	0,34	0,67	0,80	0,66
3	**102,05**	22,85	41,9	0,00	0,33	0,20	1,00	0,67	0,80
4	214,25	24,08	33,2	0,72	0,37	0,03	0,28	0,63	0,97
5	177,19	24,17	42	0,48	0,38	0,21	0,52	0,63	0,79
6	169,21	33,07	46,4	0,43	0,70	0,30	0,57	0,30	0,70
7	191,03	22,28	35,6	0,57	0,31	0,08	0,43	0,69	0,92
8	190,88	34,85	36,6	0,57	0,77	0,10	0,43	0,23	0,90
9	**257,09**	28,92	**31,8**	1,00	0,55	0,00	0,00	0,45	1,00
10	174,34	19,19	65,6	0,47	0,19	0,68	0,53	0,81	0,32
11	172,94	28,67	**81,2**	0,46	0,54	1,00	0,54	0,46	0,00
12	181,68	**41,22**	77,7	0,51	1,00	0,93	0,49	0,00	0,07
13	199,16	21,8	61	0,63	0,29	0,59	0,37	0,71	0,41
14	201,88	26,69	67,8	0,64	0,47	0,73	0,36	0,53	0,27
15	216,5	37,31	71,6	0,74	0,86	0,81	0,26	0,14	0,19
16	189,26	18,75	70	0,56	0,18	0,77	0,44	0,82	0,23
17	211,45	18,23	70	0,71	0,16	0,77	0,29	0,84	0,23
18	193,72	40,62	62	0,59	0,98	0,61	0,41	0,02	0,39

Table 5. Grey relational analysis method for step 5-6

No	Tensile Strength Test (MPa)	Izod Pendulum Impact Resistance Test (kJ/m²)	Three Point Bending Test (MPa)	Grey Relational Degree	Ranking
1	0,73	0,50	0,51	0,59	16
2	0,60	0,56	0,60	0,59	17
3	0,50	0,60	0,56	0,55	18
4	0,78	0,61	0,51	0,64	13
5	0,66	0,62	0,56	0,61	14
6	0,64	0,77	0,59	0,66	12
7	0,70	0,59	0,52	0,60	15
8	0,70	0,81	0,53	0,67	10
9	1,00	0,69	0,50	0,73	5
10	0,65	0,55	0,76	0,66	11
11	0,65	0,68	1,00	0,78	4
12	0,67	1,00	0,93	**0,86**	**1**
13	0,73	0,58	0,71	0,68	9
14	0,74	0,65	0,79	0,73	6
15	0,79	0,87	0,84	0,83	2
16	0,70	0,55	0,82	0,69	8
17	0,77	0,54	0,82	0,72	7
18	0,71	0,98	0,72	0,79	3
	Mean Grey Relational Degree			**0,69**	

Table 6. New factor levels of inputs

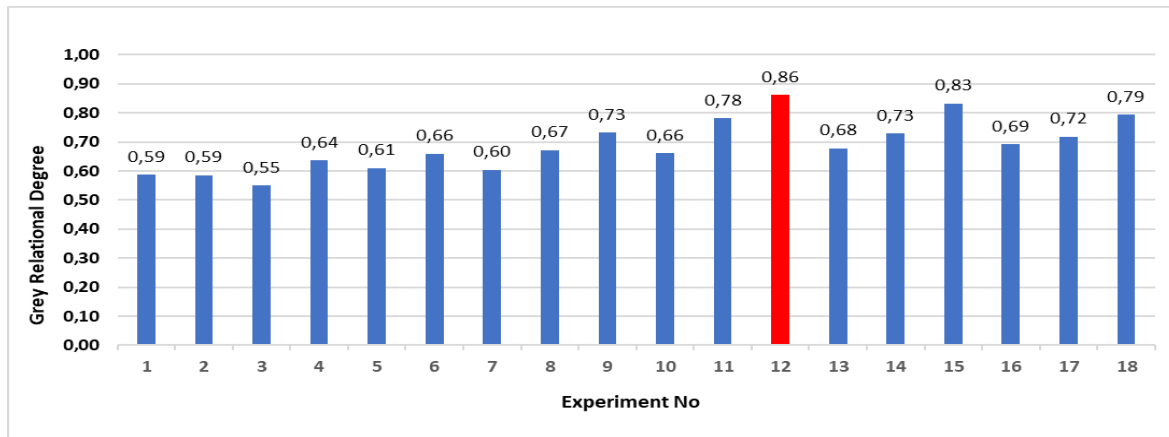| Factors	Levels						Max-Min	Rank
	1	2	3	4	5	6		
A	0,5739	0,6355	0,6696	**0,7683**	0,7468	0,7353	0,1944	1
B	0,6431	0,6832	**0,7383**				0,0952	2
C	**0,7146**	0,6893	0,6607				0,0540	3

Figure 2. The graph of grey relational degree for outputs

The graph of the parameters levels is shown in Figure 3. It is understood that optimal parameter levels are combination of A4B3C1. (The experimental plan has not this combination.)

Step 8. ANOVA test results are given in Table 7. In the table, Factor A (Fabric) has the highest F value. Factor B (Al$_2$O$_3$ Additive) has Second F value and Factor C (SiC Additive) has third F value. The highest F value means that the most effective factor is Factor A (Fabric). This value shows that when input parameter values are evaluated together, the most influential factor on output parameters is Factor A (Fabric). Figure 4 shows contribution (%) of factors in the grey relational grade.

Step 9: Finally, last step is the Taguchi Method using Grey relation degree values from Table 5 and confirmation test. In Table 8, S/N Ratio of Grey Relational Degree is seen (Equation 7 and using MINITAB 15® package program). As seen in Table 8, the lowest S/N value is in 12th experiment. This means that the most optimum sample is sample number 12 when tensile strength, Izod pendulum impact resistance, and three point bending values are evaluated together.

Figure 5 also shows the S/N ratio graph obtained from the MINITAB 15® package program.
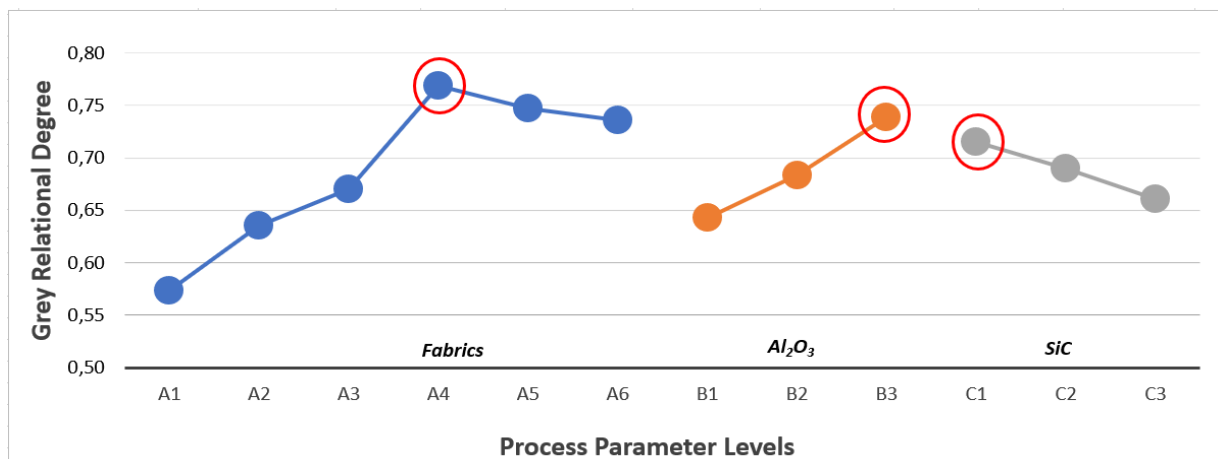
Figure 3. The graph of process parameter levels

Table 7. ANOVA of grey relational degree

Source	DF	Seq SS	Adj SS	Adj MS	F	Contribution (%)
A	5	0,081511	0,081511	0,016302	**10,34**	**62,94**
B	2	0,026311	0,026311	0,013156	8,35	20,32
C	2	0,009078	0,009078	0,004539	2,88	7,01
Residual Error	8	0,012611	0,012611	0,001576		9,74
Total	17	0,129511				

Figure 4. Contribution (%) of factors in the grey relational grade

Table 8. Determination S/N ratio

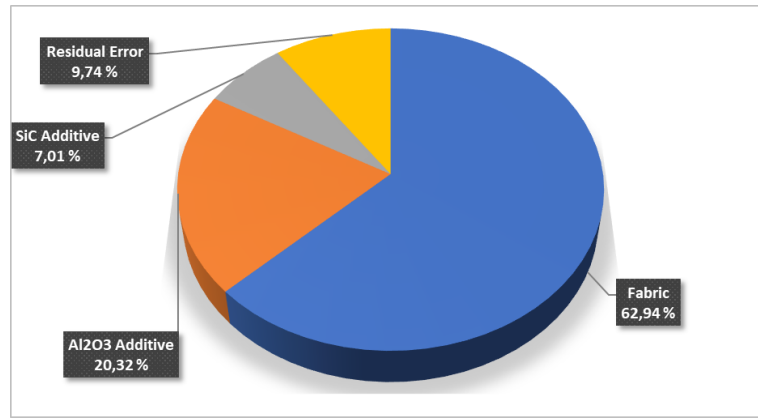| Experiment No	A (Fabric)	B (Al$_2$O$_3$ Additive)	C (SiC Additive)	S/N (dB)
1	1 (B30)	1 (0)	1 (0)	-4,58296
2	1 (B30)	2 (2)	2 (5)	-4,58296
3	1 (B30)	3 (4)	3 (10)	-5,19275
4	2 (B40)	1 (0)	1(0)	-3,87640
5	2 (B40)	2 (2)	2 (5)	-4,29340
6	2 (B40)	3 (4)	3 (10)	-3,60912
7	3 (B50)	1 (0)	2 (5)	-4,43697
8	3 (B50)	2 (2)	3 (10)	-3,47850
9	3 (B50)	3 (4)	1(0)	-2,73354
10	4 (K30)	1 (0)	3 (10)	-3,60912
11	4 (K30)	2 (2)	1 (0)	-2,15811
12	4 (K30)	3 (4)	2 (5)	**-1,31003**
13	5 (K40)	1 (0)	2 (5)	-3,34982
14	5 (K40)	2 (2)	3 (10)	-2,73354
15	5 (K40)	3 (4)	1(0)	-1,61844
16	6 (K50)	1 (0)	3 (10)	-3,22302
17	6 (K50)	2 (2)	1(0)	-2,85335
18	6 (K50)	3 (4)	2 (5)	-2,04746
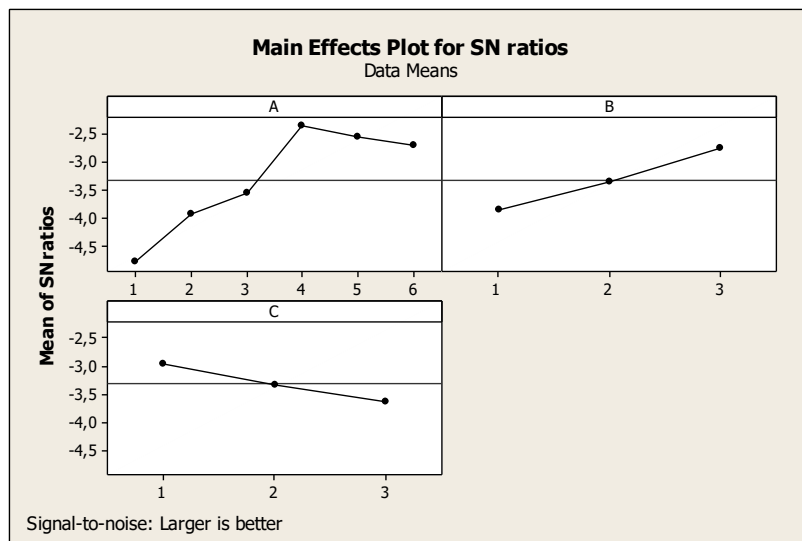
Figure 5. The S/N Ratio Graph Obtained from The MINITAB 15® Package Program

3.2 Confirmation test

As seen in Grey Relational Taguchi test results (Figure 3), optimum sample is the sample containing, 30% carbon fabric, 4% Al_2O_3 and 0% SiC when tensile strength, Izod pendulum impact resistance and three point bending values are evaluated together.

It is an expected result that the mechanical properties of composites containing carbon fabric are better. The reason for this is that the mechanical properties of carbon fabric are better than basalt fabric.

Since the optimum combination sample suggested by the Grey Relational Taguchi Method was not included in the experimental plan, it was reproduced. After that, tensile strength test, Izod pendulum impact resistance test and three point bending test were done on the optimum combination sample. The Grey Relational Degree was calculated for the estimation and the experiment. Improvement in Grey Relational Grade was also found. These findings are seen collectively in Table 9. In this table, the initial process parameter was chosen as the first experiment and the degree of improvement in Grey Relational Grade was calculated accordingly. Likewise, the improvement in Grey Relational Grade for the values below

the Grey Relational Degree obtained in the calculations for the experimental result of the optimum process parameter are calculated and given in Table 10 collectively. The highest recovery rate is seen as 0,07 when the 3rd experiment plan is selected as the initial process parameter.

Experiment (1) (A1B1C1) is chosen as the initial design. Grade of Grey Relations = 0,59 calculated for this experiment. Average Grey Relationship Grade for weighting coefficient of Tensile Strength 0,35- Izod Pendulum Impact Resistance 0,35- Three Point Bending 0,30 is η_m, 0,69 (Table 5) Optimum levels of factors are $\eta_{A4} = 0,7683$, $\eta_{B3} = 0,7383$ ve $\eta_{C1} = 0,7146$.

For the experiment performed at optimum process parameters (A4B3C12), the Grey Relationship Degree is calculated as follows by applying the 1st Step, 2nd Step, 3rd Step, 4th Step, 5th Step and 6th Step in the method and is found as 0,62.

The difference between the Grey Relationship Degree (0,62) calculated for the experiment performed at the optimum process parameters and the Grey Relationship Degree (0,59) calculated for the Initial process parameters gives the improvement in the Grey Relationship Degree. This value is seen as 0,03 in the Table 9.

Table 9. Tensile strength, izod pendulum impact resistance and three point bending of samples produced using initial and optimum composite components (for weighting coefficient tensile strength 0,35- izod pendulum impact resistance 0,35- three point bending 0,30)

	Initial Process Parameter	Optimum Process Parameter	
		Prediction	*Experiment*
Level	A1B1C1	A4B3C1	A4B3C1
Tensile Strength (MPa)	201,05		178,98
Izod Pendulum Impact Resistance (kJ/m^2)	13,94		12,51
Three Point Bending (MPa)	34,2		60,06
Grey Relational Degree	0,59	0,84	0,62
Improvement in Grey Relational Grade		0,03	

$$\eta = \eta_m + \left(\eta_{A4} - \eta_m\right) + \left(\eta_{B3} - \eta_m\right) + \left(\eta_{C1} - \eta_m\right)$$

$$\eta = 0,69 + (0,7683 - 0,69) + (0,7383 - 0,69) + (0,7146 - 0,69 = 0,84$$
$$\eta = 0,8$$

Table 10. Improvement in Grey Relational Grade for The Values Below The Grey Relational Degree Obtained in The Calculations For The Experimental Result of The Optimum Process Parameter

Experiment No	Initial Process Parameter Grey Relational Degree	Optimum Process Parameter Grey Relational Degree *(for Experiment) (A4B3C1)*	Improvement in Grey Relational Grade
1	0,59	0,62	0,03
2	0,59	0,62	0,03
3	**0,55**	**0,62**	**0,07**
5	0,61	0,62	0,01
7	0,60	0,62	0,02

4. CONCLUSION

In this study, mechanical properties (Tensile strength, Izod pendulum impact resistance and three point bending) of basalt, carbon fabric reinforced particle additive composites were investigated using Grey Taguchi orthogonal experimental design. For this, 18 different composite containing basalt and carbon fabric (at the rate of 30, 40 and 50%), Al_2O_3 (Alumina) (at the rate of 0, 2 and 4%) and SiC (Silicon carbide) (at the rate of 0, 5 and 10%) were produced. Tensile strength, Izod pendulum impact resistance and three point bending tests were performed on the samples. According to the Grey Taguchi orthogonal experimental design, optimum combination for mechanical properties was 30% carbon fabric, 4% Al_2O_3 and 0% SiC. The improvement was seen as 0,07 when the 3rd experiment plan was selected as the initial process parameter. In this designed experimental study, it was seen that the optimum composite in terms of selected mechanical properties is not basalt fabric, but carbon fabric, and at the same time, SiC has no effect. Thus, carbon and basalt fabric reinforced particle added composite plates could be compared in terms of mechanical properties. Although there is no similar study in the literature in which the reinforcement is basalt or carbon fabric and Al_2O_3 and SiC powders are added to the resin, there are studies to increase the mechanical properties of these powders. In the optimum composite combination obtained, Al_2O_3 was included with carbon fabric. In the study of Kaybal et al. (2016), it was concluded that adding Al_2O_3 to the epoxy composite significantly improved the tensile property of the composite [36]. It can be interpreted that SiC has no effect on optimum mechanical properties, this particle is micro-sized and has sharp corners due to its crystal structure, thus creating discontinuity in its contact with the fibers in the fabric and weakening the mechanical property. SiC can improve the mechanical properties of the composite if the reinforcement material is irregular fibers and not fabric. As a study supporting this in the literature, Özsoy et al. (2015) can be given. In the study conducted by Özsoy et al. (2015), it was seen that adding micro and nano ceramic particles to the epoxy resin composite improves the mechanical properties of the composite [37]. Investigation of these particle reinforcements in terms of properties such as tribological and hardness may be recommended in future studies.

This study can be developed with experimental studies in which carbon and basalt fabric are designed not as a single layer, but as a multi-layer. Again, using more than 4% Al_2O_3 particle ratio can be investigated. In the continuation of the study, instead of multi-objective optimization, studies in which each mechanical property is optimized separately can be done.

REFERENCES

1. Van de Velde K, Kiekens P, Van Langenhove L. 2003. Basalt fibres as reinforcement for composites. *Proceedings of 10th International Conference on Composites/Nano Engineering,* 20-26. Zwijnaarde, Belgium.

2. Singha K. 2012. A Short Review on Basalt Fiber. *International Journal of Textile Science*, 1(4): 19-28.

3. Gilewicz P, Dominiak J, Cichocka A, Frydrych, I. 2013. Change in structural and thermal properties of textile fabric packages containing basalt fibres after fatigue bending loading. *Fibres & Textiles in Eastern Europe*, 21, 5(101): 80-84.

4. Dalinkevich AA, Gumargalieva KZ, Marakhovsky SS, Soukhanov, AV. 2009. Modern Basalt Fibrous Materials and Basalt Fiber-Based Polymeric Composites. *Journal of Natural Fibers,* 6:3, 248-271. doi: 10.1080/15440470903123173

5. Fragassa C, Paola SD, Minak G. 2013. Improving Mechanical Properties of Green Composites by Hybridization. *4th Conference on Natural Fibre Composites,* Rome 17-18 October 2013.

6. Ovalı S. 2015. Bazalt Lifi ve Dolgu Malzemesi Takviyeli Termoplastik Esaslı Kompozit Yapıların Isı ve Ses Yalıtım Özelliklerinin İncelenmesi. *Master's Thesis, University of Marmara, Institute of Science, Department of Textile Engineering (In Turkish).*

7. Chuvashov Y, Jashchenko O, Diduk I, Gulik, V. 2020. The Investigation of Fiber Surface Condition from Basalt-like Rocks for Enhanced Industrial Applications. *Journal of Natural Fibers,* doi: 10.1080/15440478.2020.1838987

8. Liu J, Chen M, Yang J, Wu Z. 2022. Study on Mechanical Properties of Basalt Fibers Superior to E-glass Fibers, *Journal of Natural Fibers*, 19:3, 882-894.

9. Gümülcine T, Bekem A, Doğu M, Gemici Z, Ünal A. 2013. İzoftalik Polyester Matrisli Sürekli E-Camı Ve Bazalt Fiber Takviyeli Kompozitlerin Mekanik Özellikleri Üzerine Deneysel Bir Çalışma. *YTU Engineering and Science Journal*, Volume: 5, Issue: 1, (APR 2013), 104-115.

10. Nayak RK, Dasha A, Ray BC. 2014. Effect of epoxy modifiers (Al2O3/SiO2/TiO2) on mechanical performance of epoxy/glass fiber hybrid composites. *Procedia Materials Science,* 1359 – 1364.

11. Agarwal G, Patnaik A, Sharma RK. 2013. Thermo-mechanical properties of silicon carbide-filled chopped glass fiber-reinforced epoxy composites. *International Journal of Advanced Structural Engineering,* 5:21.

12. Bulut M. 2018. Vibration analysis of carbon and Kevlar fiber reinforced composites containing SiC particles. *Sakarya University Journal of Science,* 22 (5), 1423-1431.

13. Prasanna SM, Vitala HR, Madhusudhan T, Raju BR. 2016. Evaluation of mechanical and tribological characterization of glass-basalt hybrid composites. *International Journal of Engineering Research And Advanced Technology,* Special Volume 02, Issue 01.

14. Ramesh K, Nayak AD, Ray BC. 2014. Effect of epoxy modifiers (Al2O3/SiO2/TiO2) on mechanical performance of epoxy/glass elyaf hybrid composites. *Procedia Materials Science,* 6, 1359–1364.

15. Gün H, Asi D. 2017. Al2O3- TiO2 (%97-3) Seramik Tozparçacık İlaveli Cam Elyaf Takviyeli Epoksi Matrisli Kompozit Malzemelerin Mekaniksel Özelliklerinin İncelenmesi. *Uşak University Journal of Science and Natural Sciences,* 33-40.

16. Vaidya RU, Rangaswamy T. 2017. A review on e-glass/ epoxy composite combined with various filler materials and its mechanical behaviour under different thermal conditions. *American Journal of Materials Science,* 7(4): 83-90.

17. Kaybal HB, Ulus H, Avcı A. 2016. Characterization of tensile properties and toughness mechanisms on nano-Al2O3 epoxy

nanocomposites. *International Journal of Innovative Research in Science, Engineering and Technology,* Vol. 5, Special Issue 12.

18. Krzyzak A, Relich S, Kosicka E, Szczepaniak, R, Mucha, M. 2022. Selected Construction Properties of Hybrid Epoxy Composites Reinforced with Carbon Fabric and Alumina. *Advances in Science and Technology Research Journal,* 16 (2), 240–248.

19. Akatsu T, Umehara Y, Shinoda Y, Wakai, F, Muto, H. 2022. Mechanical properties of alumina matrix composite reinforced with carbon nanofibers affected by small interfacial sliding shear stress. *Ceramics International,* 48. 8466–8472.

20. Sanusi OM, Oyelaran OA, Badmus JA. 2020. Ballistic study of alumina ceramic-steel composite for structural applications. *Journal of Ceramic Processing Research,* Vol. 21, No. 4, 501-507.

21. Lin JL, Su SM, He YB, Kang, FY. 2020. Improving thermal and mechanical properties of the alumina filled silicone rubber composite by incorporating carbon nanotubes. *New Carbon Materials,* 35(1): 66-72.

22. Kim SH, Park SJ. 2021. Effect of graphene oxide/graphitic nanofiber nanohybrids on interfacial properties and fracture toughness of carbon fibers-reinforced epoxy matrix composites. *Composites Part B: Engineering*, 227, 109387.

23. Kim S, Rhee KY, Park SJ. 2020. Amine-terminated chain-grafted nanodiamond/epoxy nanocomposites as interfacial materials: Thermal conductivity and fracture resistance. *Composites Part B: Engineering*, 192 ,107983.

24. Özgür E., Sabır EC, Sarpkaya Ç. 2023. Multi-objective Optimization of Thermal and Sound Insulation Properties of Basalt and Carbon Fabric Reinforced Composites Using the Taguchi Grey Relations Analysis. *Journal of Natural Fibers*, 20:1, DOI: 10.1080/15440478.2023.2178580.

25. Jamshaid H, Ahmad N, Hussain U, Mishra, R. 2022. Parametric optimization of durable sheeting fabric using Taguchi Grey Relational Analysis. *Journal of King Saud University – Science,* Volume 34, Issue 4,102004, ISSN 1018-3647.

26. Minitab User's Guide2, *Minitab Inc*., 2000.

27. Sarpkaya Ç. 2014. Taguchi metoduna dayalı gri ilişkiler analizi ile haşıl prosesinin optimizasyonu, *PhD Thesis, Institute of Natural and Applied Sciences, Department of Textile Engineering, University of Çukurova/Türkiye* (in Turkish), 141.

28. KuoY, Yang T, Huang GW. 2008. The Use of a Grey Based Taguchi Method for Optimizing Multi Response Simulation Problems. *Engineering Optimization,* Vol 40. No.6, 517-528.

29. Khan ZA, Siddiquee AN, Kamaruddin S. 2012. Optimization of In-feed Centreless Cylindrical Grinding Process Parameters Using Grey Relational Analysis. *Pertanika Journal of Science and Technology,* Vol 20 (2), 257 – 268.

30. Sarpkaya Ç, Sabır EC. 2016. Optimization of the sizing process with grey relational analysis. *Fibres & Textiles in Eastern Europe,* Vol. 24, 1(115). 49-55.

31. Pawade RS, Joshi SS. 2011. Multi-objective Optimization of Surface Roughness and Cutting Forces in High-speed Turning of Inconel 718 Using Taguchi Grey Relational Analysis (TGRA). *The International Journal of Advanced Manufacturing Technology,* Volume 56, 47-62.

32. Sarpkaya Ç, Özgür E, Sabır EC. 2015. The Optimization of woven fabric tensile strength with Taguchi method based on grey relational analysis, *Tekstil ve Konfeksiyon,* Year 25, Vol 4, 293-299.

33. Palanikumar K, Latha B, Senthilkumar VS, Paulo Davim J. 2012. Analysis on Drilling of Glass Fiber–Reinforced Polymer (GFRP) Composites Using Grey Relational Analysis, *Materials and Manufacturing Processes,* 27:3, 297-305, DOI: 10.1080/10426914.2011.577865

34. Tang L, Du YT. 2014. Multi-Objective Optimization of Green Electrical Discharge Machining Ti–6Al–4V in Tap Water via Grey-Taguchi Method, *Materials and Manufacturing Processes,* 29:5, 507-513, DOI: 10.1080/10426914.2013.840913

35. Özgür E. 2022. Bazalt, karbon kumaş takviyeli parçacık katkılı kompozitlerin üretimi ve mekanik, ısı ve ses yalıtım özelliklerinin optimizasyonu. *PhD Thesis, Institute of Natural and Applied Sciences, Department of Textile Engineering, University of Çukurova/Türkiye (*In Turkish*).*

36. Kaybal HB, Ulus H, Avcı A. 2016. Characterization of Tensile Properties And Toughness Mechanisms on Nano-Al2O3 Epoxy Nanocomposites. *International Journal of Innovative Research in Science, Engineering and Technology*, Vol. 5, Special Issue 12.

37. Özsoy N. 2015. Polimer esaslı fiber takviyeli kompozit malzemelerin tribolojik ve mekanik özelliklerinin incelenmesi. *PhD Thesis, Sakarya University, Institute of Science, Department of Mechanical Engineering, Sakarya/ Türkiye (In Turkish).*

Morphological and Mechanical Assessment of Electrospun PLGA Vascular Scaffolds

Suzan Özdemir [ID] 0000-0001-7369-2907
Janset Öztemur [ID] 0000-0002-7727-9172
Hande Sezgin [ID] 0000-0002-2671-2175
İpek Yalçın Eniş [ID] 0000-0002-7215-3546

Istanbul Technical University / Textile Engineering Department / Istanbul, Turkiye

Corresponding Author: Suzan Özdemir, ozdemirsu@itu.edu.tr

ABSTRACT

Cardiovascular disorders are the leading cause of global mortality and necessitate bypass surgery to replace the damaged blood vessels. Currently used grafts are insufficient to replace small-diameter blood vessels due to the scarcity and harsh harvesting procedures of autologous vessels and the shortcomings in the clinical performance of synthetic grafts. Therefore, there is a critical need for tissue-engineered vascular grafts that can meet morphological, mechanical, and biological characteristics. In this study, poly(lactic-co-glycolic acid) tubular scaffolds with randomly distributed or radially oriented fibers were produced by electrospinning, and the effect of fiber orientation on morphological, physical, and mechanical properties was investigated. Also, instrumental assessments were conducted to perform a comprehensive analysis of the polymeric material, encompassing evaluations of its toxicity and thermal properties. The findings demonstrate that, while successful implementation of radial fiber orientation with high rotational speed production enhanced burst strength and radial tensile strength values, it was unfavorable for compliance.

1. INTRODUCTION

Tissue engineering confronts a significant problem in replicating the particular architecture and mechanical properties of the arterial wall in order to meet the basic requirements of the native vessels with diameters smaller than 6 mm [1, 2]. The commonly employed synthetic materials in commercial applications include expanded polytetrafluoroethylene (ePTFE, Gore-Tex) and polyethylene terephthalate (PET, Dacron) [3]. These materials have demonstrated successful outcomes as substitutes for large-caliber arterial grafts like the carotid or common femoral artery, exhibiting favorable long-term results. However, their usage is limited to smaller diameter vascular grafts (< 6mm), such as coronary arteries, due to observed challenges such as poor patency rates resulting from neointimal hyperplasia in peri-anastomotic regions, as well as concerns related to thrombogenicity and compliance mismatch [4, 5]. An efficient vascular graft ought to possess a suitable topology, be biocompatible, antithrombogenic, bioactive, have good mechanical characteristics, and instantly adapt to the existing hemodynamic environment [6]. The mechanical characteristics of vascular prostheses influence biological activities such as the growth of smooth muscle and endothelial cells and accelerate extracellular matrix (ECM) synthesis via enhanced macrophage activity [7]. The ECM deposition is crucial as it is a three-dimensional (3D) network of molecules that provides structural and biochemical support for cells and promotes cell survival, adhesion, proliferation, communication, and differentiation, playing a vital role in cellular processes [8]. Thus, vascular grafts with inadequate mechanical characteristics create an unfavorable microenvironment for neotissue formation [7]. Through the technique of electrospinning, it is feasible to fabricate fibers using biopolymers that closely resemble the complex 3D microenvironment of the ECM. This approach allows for the control and manipulation of various fiber characteristics, such as morphology, diameter, orientation, porosity, pore size, wall thickness, and the creation of multilayered structures [9, 10]. These capabilities enable the replication of the distinct layers present in native blood

vessels, including the *tunica intima*, *media*, and *adventitia* [9]. The design criteria that affect the properties of vascular grafts can be categorized under two topics: material selection and constructional components such as fiber diameter, pore size, fiber orientation, and wall thickness [11]. For instance, fiber alignment influences how cells grow, how they build their morphologies on scaffolds, and how they align through the vessel wall. Moreover, radial fiber orientation is known to have a beneficial impact on the values of modulus, tensile strength in the same direction, and burst strength, whereas it reduces compliance [12]. On the other hand, excessive wall thickness within the vascular scaffolds creates a disadvantageous situation in terms of cell activities and proliferation, as it restricts features such as porosity and compliance [13]. Compliance, expressed as a percentage of diameter change per 100 mmHg, serves as a measure of flexibility or stiffness [14]. The mismatch in compliance between a rigid vascular graft and the native vessel at the anastomosis sites can lead to issues such as turbulent blood flow and reduced blood flow rates in small grafts. This, combined with the thrombogenic nature of foreign materials used in the graft and the absence of endothelialization, contributes to thrombosis and narrowing of the blood vessel (luminal constriction) due to intimal hyperplasia. Consequently, these factors result in poor graft patency rates [15]. Also, the choice of biomaterials is critical in establishing the framework for mechanical qualities, cellular activities, biocompatibility, biodegradability, and anti-toxicity [16]. In this regard, poly(lactic-co-glycolic acid) (PLGA) is a synthetic biopolymer which supports the biological activities and has tunable mechanical strength and biodegradation rate [17]. Malik et al. (2021), produced tubular fibrous scaffolds with oriented fibers consisting of various biopolymers such as PLGA, polycaprolactone (PCL) and polyvinyl acetate (PVA). PLGA vascular grafts outperformed other polymers in terms of tensile strength (9.1 ± 0.6 MPa), suture retention strength, and burst pressure (350 ± 50 mmHg). These scaffolds have also been discovered to have appropriate porosity and elongation characteristics (87% and 183%, respectively), making them viable materials for vascular grafts. When the aligned scaffolds were compared with their counterparts, remarkable improvements in the mechanical properties such as tensile strength, strain, and burst strength were observed in all the samples (2 MPa vs. 9.1 MPa, 120% vs. 183%, and 350 mmHg vs. 680 mmHg, respectively, for PLGA) [18]. In another study of Johnson et al. (2015) the effect of polymer selection and wall thickness on the mechanical features of the vascular prosthesis was investigated. First of all, the biomechanical characteristics of electrospun vascular grafts made of various biopolymers were examined. The bursting strength of the scaffold made of PLGA showed the highest value with 3.3 MPa, which is slightly higher than the burst pressure of commercially used Dacron graft with 3.2 MPa. However, compliance results revealed that PLGA grafts demonstrate a relatively low compliance value of 1.9%/mmHg [19].

Within the scope of this study, electrospun vascular prostheses consisting of randomly distributed and radially oriented PLGA fibers were fabricated for the purpose of assessing both the effect of fiber arrangement on the mechanical properties in terms of tensile strength and strain, burst strength, and compliance, as well as determining the suitability of PLGA scaffolds in regards to physical, morphological, chemical, thermal, and mechanical characteristics.

2. MATERIAL AND METHOD

2.1 Material

PLGA (Mw: 50,000–75,000 g/mol, PLA/PGA:85/15) was used as a polymer, whereas chloroform (CH), acetic acid (AA), and ethanol (ETH) were utilized as the solvent system components. The chemicals were purchased from Sigma-Aldrich.

2.2 Method

Fabrication of PLGA vascular grafts

PLGA was dissolved in CHL/ETH/AA (8/1/1 wt.) at a concentration of 18% wt. based on preliminary studies [20]. The tubular samples were produced using an electrospinning unit (Nanospinner, Ne100+) provided by Inovenso, Turkey. The PLGA solutions were delivered by using a feeding rate of 2.25 ± 0.25 ml/h and subjected to 11 ± 2 kV voltage by using 20 cm needle to collector distance. Rotating rod collectors with 5 mm diameter and different rotational speeds of 200 rpm and 10,000 rpm were used to achieve samples with randomly distributed (PLGA_R) and radially oriented fibers (PLGA_O). The spinning time for all samples was set at 40 minutes to achieve the adequate wall thickness expected from vascular grafts.

Morphological and physical characterization

SEM Analysis

The surface morphologies of electrospun surfaces were investigated by using a scanning electron microscope (SEM). The SEM images of tubular scaffolds were taken with magnifications of 1kx.

Fiber diameter and wall thickness measurement

The Image J Software System was used to calculate average fiber diameters from SEM images of at least 50 distinct fibers. The wall thickness of samples was measured with a Standard Gage Electronic External Micrometer (Hexagon Metrology, Turkey).

Water contact angle assessment

The KSV Attension Optical Contact Angle Meter is employed to measure the water contact angles on scaffold

surfaces using the sessile drop measurement technique, enabling the evaluation of surface hydrophilicity. The contact angle serves as a valuable indicator, conveying insights into surface hydrophilicity and wettability. A higher contact angle on the surface corresponds to reduced hydrophilicity and wettability [21].

Chemical and thermal characterization

Fourier-transform infrared spectroscopy analysis (FTIR)

FTIR analysis was conducted employing Fourier-transform infrared spectrometry (UATR Two, Perkin Elmer) to detect the presence of characteristics peaks of PLGA. This analysis also serves to substantiate the absence of any residual solvents within the fibrous scaffolds subsequent to their production. The infrared absorption spectra of the samples were obtained within the range of 500–4000 cm^{-1}.

Differential scanning calorimetry (DSC) analysis

The Perkin Elmer DSC400 was used to conduct the thermal analysis and also the confirm the amorphous structure of the PLGA webs. The analysis took place under atmospheric pressure in a nitrogen atmosphere, with a sample weight of 5 mg. The PLGA webs were subjected to a heating rate of 7°C/min, starting from 30°C and reaching a maximum temperature of 400°C. By measuring the heat flow during the temperature ramp, the DSC provides valuable data for determining both the glass transition temperature (T_g) and the maximum decomposition rate of the PLGA webs [22, 23].

Mechanical assessment

Tensile strength and strain

Tensile testing was performed by using Zwick-Roell Z005 universal testing machine (ZwickRoell, Germany) for the assessment of the mechanical performance of the tubular grafts. The tubular samples were tested in axial (0°) and radial (90°) directions in both planar (_P) and tubular form (_T). The planar test samples were cut into 10mm x 15mm (width x length) dimensions from tubular scaffolds whereas tubular samples with 1.5 cm length were cut for testing in tubular manner. Testing the samples in tubular shape along the longitudinal direction arises from simulating the position of vascular grafts in the body and examining how they respond to mechanical forces in its own shape. The cross-head speed was set at 10 mm/min while the distance between the gauges was 5 mm.

Burst pressure measurement

The burst strength measurement is utilized to assess the maximum pressure that a vascular prosthesis can endure before experiencing failure [24]. The burst pressure properties of the tubular graft structures were measured by custom design burst tester (Inovenso, Turkey). The balloon was placed into the tubular samples cut in 4 cm length. Then, the sample ends were fastened into the air nozzles with the help of sleeves, and pressurized air flow was provided. The burst pressure value was recorded when the sample fails as a result of supplied air pressure from the nozzles.

Compliance

The custom-designed device (Inovenso, Turkey) with provided air flow used to measure the compliance at a physiologically equivalent pressure of 80–120 mmHg as specified in ISO 7198:2016 [25]. The photographs of the samples under provided pressure ranges were captured using a camera system. The Image J software system was then utilized to measure the diameters of the samples at each pressure. Then, the compliance values were calculated by the formula given in Equation (1).

$$\%compliance = \frac{\frac{R_{p_2}-R_{p_1}}{R_{p_1}}}{p_2-p_1} \times 10^4 \qquad \text{Eq. 1}$$

where R_{p2} is a pressurized radius at diastolic pressure (mm), R_{p1} is a pressurized radius at systolic pressure (mm), p_1 is a diastolic pressure (mmHg), and p_2 is a systolic pressure (mmHg). To ensure accuracy and reliability, compliance measurements for each vascular graft were repeated a minimum of three times

3. RESULTS AND DISCUSSION

3.1 SEM analysis

SEM images, which are represented in Figure 1, revealed that both scaffolds consist of smooth, homogenous, and bead-free fibers. In the research conducted by Stojko et al. (2020), electrospun wound dressings with PLGA consisting of different proportions of lactic acid (LA) and glycolic acid (GA) (50/50, 70/30, and 85/15) was produced by using chloroform based solvent system and polymer concentrations of 15-18% wt. SEM examinations showed that the resulting fibers exhibited a consistent, elongated, and smooth structure [26]. On the other hand, the radial fiber orientation was achieved when the collector speed was set at 10,000 rpm. The high collector speed causes a higher linear velocity of the mandrel, which supports the fiber alignment in the circumferential direction [27]. The attainment of randomly distributed fibers on the collector can be accomplished by adjusting the rotational speed to a value below the take-up speed of the fibers. This ensures that the fibers are not aligned in a specific orientation, leading to a random arrangement on the collector surface [28]. Hu et al. (2012) also produced vascular grafts with electrospun PCL fibers, achieving various fiber orientations by altering the collector's rotation speed. Through optical microscopy, they determined that faster collector rotation resulted in higher degree of fiber alignment [29].
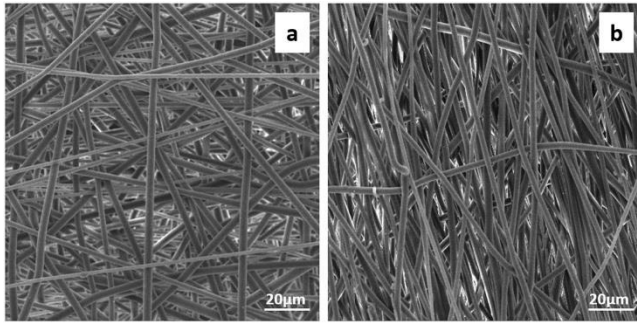
Figure 1. SEM images at 1kx magnification of neat PLGA samples produced on tubular collector with rotational speeds of 200 rpm and 10,000 rpm (a) PLGA_R and (b) PLGA_O.

3.2 Fiber diameter and wall thickness measurement

The fiber diameters of the produced scaffolds, as presented in Table 1, range between 2.3 and 2.6 µm. Fiber diameters are affected by many parameters in electrospinning, such as voltage, solvent systems, polymer concentration, flow rate, spinneret diameter, rotational speed, and so on [30, 31]. In a study of Milleret et al. (2012), PLGA vascular grafts were manufactured by employing chloroform as a solvent and modifying electrospinning parameters. They measured fiber diameters, which spanned from 0.63 µm to 5.02 µm, contingent upon the chosen parameters [32]. Similarly, Ko et al. (2016) generated electrospun PLGA surfaces using various solvents, resulting in fiber diameters ranging between 0.2 µm and 5 µm. Notably, surfaces produced with chloroform exhibited the largest fiber diameter at 5 µm [33]. In a separate study, You et al. (2005) examined the fiber diameters of samples produced from polyglycolic acid (PGA), polylactic acid (PLA), and PLGA. PLGA exhibited thicker fiber diameters, ranging from 0.2 to 1.8 µm. This variation was attributed to solvent properties, including electrical conductivity and polarity [34]. Existing literature highlights that the use of non-polar solvents like chloroform or dichloromethane leads to an increase in fiber diameters [35]. Also, it can be seen from the fiber diameter values that the PLGA_O sample has thinner fibers than the PLGA_R sample. This situation can be explained by the stretching of the fibers because of the rotational movement and speed of the rotating collector [36, 37]. Fibrous webs generated at higher rotational speeds result in thinner fiber diameters compared to those produced at lower collector speeds due to the application of stretching force [38]. On the other hand, the wall thickness values measured in both grafts are sufficient and fall within the wall thickness range given for vascular grafts in the literature (200 µm-600 µm) [39]. It is also emphasized that the wall thickness of the vascular grafts should be as thin as possible if they can demonstrate enough mechanical endurance and biodegradation [40]. In the current investigation, despite employing identical production systems and durations, variations in wall thickness were observed, particularly in relation to different collector rotation speeds. This suggests that the collector speed can influence the wall thickness of the produced fibers. It is hypothesized that a high-speed rotating collector rapidly draws in the fibers, limiting their dispersion and resulting in a thicker wall structure.

Table 1. Wall thicknesses, fiber diameters, and fiber diameter histograms of PLGA vascular grafts.

Samples	Wall thickness (µm)	Fiber diameter (µm)	Fiber diameter distribution
PLGA_R	208 ± 33	2.579 ± 0.782	
PLGA_O	245 ± 28	2.372 ± 0.407	

3.3 Analysis of surface wetting properties

Table 2 displays the water contact angles observed on the PLGA scaffolds. Both samples exhibit hydrophobic characteristics, as indicated by their relatively high contact angles, impacting the surfaces' wettability. Notably, there isn't a substantial difference between the contact angles of the two samples. Furthermore, it's worth mentioning that the contact angle and surface hydrophilicity aren't linked to the orientation of the fibers but are instead related to the nature of the polymer itself. This aligns with the expected hydrophobic behavior of PLGA, as supported by prior research [41, 42], which can be attributed to the high content of lactic acid within the polymer (85%). The existence of methyl side groups in lactic acid increases its hydrophobicity compared to glycolic acid. As a result, copolymers of PLGA rich in lactide are less prone to absorbing water due to their reduced hydrophilicity, which leads to a slower degradation process [43]. In a study of Ji Lee et al. (2014), the fibrous webs consisting of neat PLGA showed a hydrophobic character with a water contact angle of 143° [44]. As it is widely recognized that increased hydrophilicity enhances surface polarity and adhesion, facilitating cell attachment and proliferation [45], existing experimental studies also demonstrate that cells can adhere to and thrive on PLGA surfaces characterized by high contact angles [46, 47].

3.4 FTIR analysis

Figure 2 confirms the presence of characteristic peaks in the PLGA fibrous webs. Analysis of the FTIR spectra reveals prominent features in specific wavenumber ranges. A distinct broad band between 1700 cm^{-1} and 1800 cm^{-1}, corresponding to the carbonyl (C=O) groups present in both monomers, is observed [48]. Additionally, a grouping band (C-O) between 1300 cm^{-1} and 1150 cm^{-1}, indicative of ester groups, is evident [49]. Moreover, the spectrum clearly exhibits stretching vibrations of the CH, CH$_2$, and CH$_3$ groups (2850–3000 cm^{-1}) [50]. Notably, the absence of characteristic peaks from chloroform, ethanol, and acetic acid in the FTIR analysis indicates the absence of residue from these solvents on the fibrous webs. Specifically, chloroform, the primary solvent, does not exhibit its characteristic peaks, including CCl$_3$ stretching at 680 and 774 cm^{-1}, and C-H stretching at 3034 cm^{-1} [51]. Similarly, ethanol, with its characteristic peaks of C-O stretching at 2055 cm^{-1}, symmetric CH stretching at 2850 cm^{-1}, and asymmetric C-H stretching at 2850 cm^{-1}, was not observed in the PLGA sample [45]. Likewise, acetic acid, with its peaks of C-O and OH vibrations at 1292 cm^{-1}, and C-H

vibrations at 1424 cm^{-1}, was not detected in the FTIR spectra of PLGA webs [52]. FTIR analysis conducted in preliminary studies further substantiated the absence of chloroform, ethanol, and acetic acid on the fibrous web [45, 53].
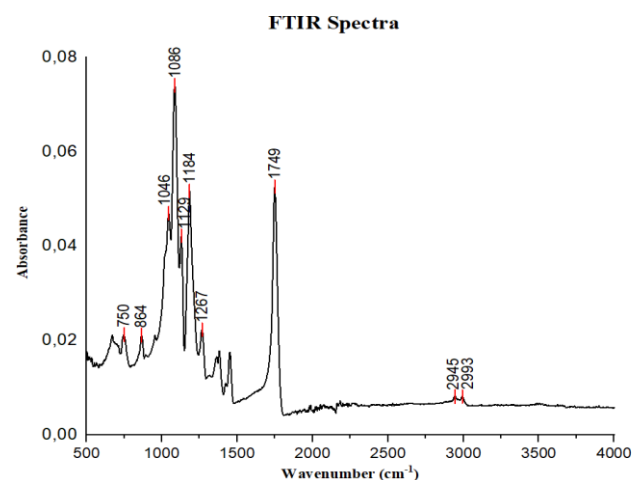

Figure 2. FTIR Spectra of PLGA web

3.5 DSC analysis

The results of the differential scanning calorimetry (DSC) performed on pure PLGA webs is displayed in Figure 3. Thermal and chemical analyses were conducted on both scaffolds, but the results are given in single curves since it is observed that the rotational speed does not have a significant impact on the thermal and chemical properties of the produced webs, which is also supported by existing literature [54]. The DSC analysis revealed an endothermic event at 52.9°C, indicating a thermal transition within the material. Additionally, an endothermic decomposition peak was observed, which centered around 334.4°C. The obtained results are consistent with previous findings reported in the literature [55, 56, 57]. The glass transition temperature of PLGA is higher than the physiological temperature, indicating that the mobility and elasticity of the polymeric material are low and that the material shows brittle behavior within the human body [58, 59]. It is also important to note that since the PLGA used in this study is in an amorphous form, it does not exhibit a melting point. Melting behavior is characteristic of polymers with a semi-crystalline structure, whereas amorphous polymers lack the ordered arrangement necessary for melting to occur [60]. Therefore, the absence of a melting point in the DSC spectra supports the amorphous nature of the PLGA utilized in this study.

Table 2. Contact angle measurements of the PLGA scaffolds.

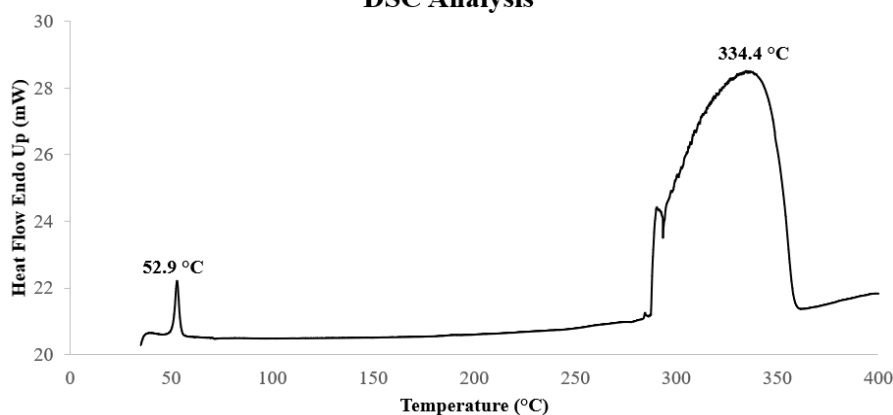| Samples	Contact Angle Mean (°)	Water Droplet Image
PLGA_R	137.12 ± 0.64	
PLGA_O	138.30 ± 0.64	

DSC Analysis

Figure 3. DSC curve of PLGA

3.6 Tensile strength and elongation

When the tensile strength and strain values (Table 3) are investigated, it has been seen that the radial fiber orientation contributed to the strength values in the radial direction with an increment from 3.81 MPa to 6.23 MPa, whereas it caused a decrement in the tensile strength values in the longitudinal direction as the fibers were all aligned in the radial direction, which enabled them to resist the applied stress collectively [61]. The findings of Wu et al. (2010) offer further support to the aforementioned observation. In their study on PCL vascular grafts, they manipulated the electrical field and adjusted the rotational speeds to generate grafts with either radial or axial fiber orientations. Their results demonstrated a notable reduction in strength along the axial direction in the radially oriented scaffolds, indicating the fibers' inability to withstand the applied load in that axial orientation [62]. On the other hand, the elongation values were improved in all directions with radial fiber orientation. In a study conducted by Malik et al. (2021), when the tensile testing results of the scaffolds with oriented and non-oriented PLGA fibers are compared, it was found that the tensile strength values for non-oriented scaffolds are lower, and the strain values are also lower. It is reported that the PLGA scaffolds with randomly distributed fibers have a tensile strength and strain of around 2 MPa and 125%, while the ones with oriented fibers have a tensile strength of 9.1 MPa and 150% [18]. In addition, the strain value of PLGA_O in the radial direction was much lower than that in the longitudinal direction because, as the oriented fibers are already under stress in their alignment direction and there are fewer junctions of fibers, they cannot be stretched too much in that direction [63]. Upon conducting a comprehensive examination of the orientation's effect, considering the test direction, it becomes evident that the tensile strength results of PLGA scaffolds with randomly distributed fibers exhibit different mechanical behavior compared with scaffolds with radial fiber orientation. Specifically, the radial (90°) direction demonstrated the lowest tensile strength values of 3.81

MPa, whereas the longitudinal (0°) direction displayed the highest strength values of 4.53 MPa and 5.89 MPa. This phenomenon can be attributed to the greater alignment of fibers in the longitudinal direction, as a consequence of the low rotational speed, which hinders their radial alignment and promotes their accumulation and alignment on the collector surface in the longitudinal direction [38]. The tensile strength and elongation values obtained from the PLGA scaffolds surpassed the literature-reported tensile testing results of the human coronary artery, with axial and radial tensile strengths measuring 1.02 MPa and 1.05 MPa, respectively, and the elongation values ranging from 45% to 99% [64, 65].

3.7 Burst strength and compliance

The burst strength and compliance measurement results are given in Table 4. The values show that the fiber orientation resulted in improved burst strength, whereas it slightly reduced the compliance levels. The orientation of fibers plays a crucial role in controlling compliance and burst pressure of grafts [66]. Aligned fibers, when subjected to strain along their alignment direction, demonstrate increased modulus, tensile strength, and burst pressure values but reduced compliance due to their stiffer structure [63]. Therefore, for an optimal balance between compliance and burst pressure resistance, particularly in the anastomotic region, a multilayer approach using carefully selected fiber orientations is necessary [67]. This approach has been advocated for achieving desired mechanical properties in vascular replacements. This situation is also supported by the study of Grasl et al. (2021), which showed that the burst strength of polylactic acid scaffolds increased from 570 ± 188 mmHg to 7641 ± 902 mmHg with radial fiber orientation, whereas compliance was reduced from 29.7%/100 mmHg to 4.1%/100 mmHg by fiber orientation in the radial direction for the polyurethane samples because of the increased stiffness of the scaffolds [68]. The results showed that the mechanical properties satisfy the minimum limits for the human saphenous vein (1599 mmHg and 0.6-1.5 %/100 mmHg) [69].

Table 3. The tensile strength and strain values of the PLGA planar and tubular samples with randomly distributed and radially oriented fibers.

	Test direction	Tensile Strength (MPa)	Strain (%)		Test direction	Tensile Strength (MPa)	Strain (%)
PLGA_R	0º_P	4.53 ± 0.80	60.41 ± 17.09	PLGA_O	0º_P	1.85 ± 0.42	851.01 ± 115.39
	90º_P	3.81 ± 0.07	48.34 ± 5.61		90º_P	6.23 ± 0.42	54.61 ± 20.84
	0º_T	5.89 ± 0.96	116.26 ± 55.85		0º_T	2.89 ± 0.23	1085.39 ± 83.10

Table 4. The burst strength and compliance values of the PLGA tubular samples with randomly distributed and radially oriented fibers.

Samples	Burst Strength (mmHg)	Compliance (%/100 mmHg)
PLGA_R	1873.50 ± 136.47	1.416 ± 0.025
PLGA_O	2889.00 ± 32.53	1.345 ± 0.082

4. CONCLUSION

The morphological analyses provided compelling evidence of successful fibrous surface production. Furthermore, the chemical analysis of the surface revealed the absence of solvent residue, as evident from the lack of characteristic peaks in the FTIR spectra. Notably, the FTIR spectra exhibited distinct characteristic peaks that correspond to PLGA, confirming its presence on the surface. Additionally, the DSC analysis demonstrated that the glass transition temperature of PLGA exceeds the physiological temperature, implying its propensity for exhibiting brittle behavior within the human body and at room temperature. Also, optimizing the design of the PLGA scaffolds by fiber orientation has proven to be a useful solution in regards to mechanical properties. Radial fiber orientation was successfully achieved in the produced fibrous vascular grafts, which also have sufficient wall thickness for mechanical tests. Alignment of the fibers along the periphery of the graft contributed to the tensile strength values in the radial direction and burst strength, resulting in a decrease in the compliance values. At the same time, the difference between the elongation values in the longitudinal and radial directions dramatically increased in the scaffolds with a radial orientation. The overall results showed that the manufactured scaffolds are promising for use in vascular grafts and can mimic the mechanical response of the native blood vessels if the stiffness problem in the radial direction can be eliminated by polymer blending or a multi-layered design approach for taking advantage of more ductile polymers.

Acknowledgement

REFERENCES

1. A Nerem, R. M., & Seliktar, D. (2001). Vascular tissue engineering. *Annual Review of Biomedical Engineering,* 3, 225–243. https://doi.org/10.1146/annurev.bioeng.3.1.225

2. Awad, N. K., Niu, H., Ali, U., Morsi, Y. S., & Lin, T. (2018). Electrospun fibrous scaffolds for small-diameter blood vessels: A review. *Membranes* 8(1) https://doi.org/10.3390/membranes8010015

3. Ravi, S., & Chaikof, E. L. (2010). Biomaterials for vascular tissue engineering. In *Regenerative Medicine* (Vol. 5, Issue 1, pp. 107–120). https://doi.org/10.2217/rme.09.77

4. Carrabba, M., & Madeddu, P. (2018). Current strategies for the manufacture of small size tissue engineering vascular grafts. In *Frontiers in Bioengineering and Biotechnology* (Vol. 6, Issue APR). Frontiers Media S.A. https://doi.org/10.3389/fbioe.2018.00041

5. Teebken, O. E., & Haverich, A. (2002). *Tissue Engineering of Small Diameter Vascular Grafts*. http://www.idealibrary.com

6. Obiweluozor, F. O., Emechebe, G. A., Kim, D. W., Cho, H. J., Park, C. H., Kim, C. S., & Jeong, I. S. (2020). Considerations in the Development of Small-Diameter Vascular Graft as an Alternative for Bypass and Reconstructive Surgeries: A Review. *Cardiovascular Engineering and Technology*, 11(5), 495–521. https://doi.org/10.1007/s13239-020-00482-y

7. Zhao, L., Li, X., Yang, L., Sun, L., Mu, S., Zong, H., Li, Q., Wang, F., Song, S., Yang, C., Zhao, C., Chen, H., Zhang, R., Wang, S., Dong, Y., & Zhang, Q. (2021). Evaluation of remodeling and regeneration of electrospun PCL/fibrin vascular grafts *in vivo*. *Materials Science and Engineering C* 118(August 2020). https://doi.org/10.1016/j.msec.2020.111441

8. Safak, S., Vatan, O., Cinkilic, N., & Karaca, E. (2020). In vitro evaluation of electrospun polysaccharide based nanofibrous mats as surgical adhesion barriers. *Tekstil ve Konfeksiyon*, 30(2), 99–107. https://doi.org/10.32710/tekstilvekonfeksiyon.548460

9. Chen, Y., Dong, X., Shafiq, M., Myles, G., Radacsi, N., & Mo, X. (2022). Recent Advancements on Three-Dimensional Electrospun Nanofiber Scaffolds for Tissue Engineering. In *Advanced Fiber Materials* (Vol. 4, Issue 5, pp. 959–986). Springer. https://doi.org/10.1007/s42765-022-00170-7

10. Sancak, E. , Ozen, M. S. , Erdem, R. , Yılmaz, A. C. , Yuksek, M. , Soın, N. & Shah, T. (2018). PA6/SILVER BLENDS: INVESTIGATION OF MECHANICAL AND ELECTROMAGNETIC SHIELDING BEHAVIOUR OF ELECTROSPUN NANOFIBERS. *Tekstil ve Konfeksiyon*, 28 (3), 229-235. Retrieved from https://dergipark.org.tr/tr/pub/tekstilvekonfeksiyon/issue/39534/466846

11. Yalcin Enis, I., & Gok Sadikoglu, T. (2018). Design parameters for electrospun biodegradable vascular grafts. *Journal of Industrial Textiles* 47 (8), 2205–2227. https://doi.org/10.1177/1528083716654470

12. Ozdemir, S., Yalcin-Enis, I., Yalcinkaya, B., & Yalcinkaya, F. (2022). An Investigation of the Constructional Design Components Affecting the Mechanical Response and Cellular Activity of Electrospun Vascular Grafts. *Membranes* 12(10), 929. https://doi.org/10.3390/membranes12100929

13. Meng, X., Wang, X., Jiang, Y., Zhang, B., Li, K., & Li, Q. (2019). Suture retention strength of P(LLA-CL) tissue-engineered vascular grafts. *RSC Advances* 9(37), 21258–21264. https://doi.org/10.1039/c9ra04529e

14. Pérez-Aranda, C., Gamboa, F., Castillo-Cruz, O., Cauich-Rodríguez, J. v., & Avilés, F. (2019). Design and analysis of a burst strength device for testing vascular grafts. *Review of Scientific Instruments*, *90*(1). https://doi.org/10.1063/1.5037578

15. Hiob, M. A., She, S., Muiznieks, L. D., & Weiss, A. S. (2017). Biomaterials and Modifications in the Development of Small-Diameter Vascular Grafts. *ACS Biomaterials Science and Engineering*, *3*(5), 712–723. https://doi.org/10.1021/acsbiomaterials.6b00220

16. Yu, E., Mi, H. Y., Zhang, J., Thomson, J. A., & Turng, L. S. (2018). Development of biomimetic thermoplastic polyurethane/fibroin small-diameter vascular grafts via a novel electrospinning approach. *Journal of Biomedical Materials Research - Part A* 106(4), 985–996. https://doi.org/10.1002/jbm.a.36297

17. In Jeong, S., Kim, S. Y., Cho, S. K., Chong, M. S., Kim, K. S., Kim, H., Lee, S. B., & Lee, Y. M. (2007). Tissue-engineered vascular grafts composed of marine collagen and PLGA fibers using pulsatile perfusion bioreactors. *Biomaterials* 28(6), 1115–1122. https://doi.org/10.1016/j.biomaterials.2006.10.025

18. Malik, S., Sundarrajan, S., Hussain, T., Nazir, A., & Ramakrishna, S. (2021). Fabrication of highly oriented cylindrical polyacrylonitrile, poly(Lactide-co-glycolide), polycaprolactone and poly(vinyl acetate) nanofibers for vascular graft applications. *Polymers*, *13*(13). https://doi.org/10.3390/polym13132075

19. Johnson, J., Ohst, D., Groehl, T., Hetterscheidt, S., & Jones, M. (2015). Development of Novel, Bioresorbable, Small-Diameter Electrospun Vascular Grafts. *Journal of Tissue Science & Engineering* 6(2). https://doi.org/10.4172/2157-7552.1000151

20. Ozdemir, S. (2023). *INVESTIGATION OF MECHANICAL PROPERTIES OF SMALL CALIBER FIBROUS VASCULAR GRAFTS*. Istanbul Technical University.

21. Kung, C. H., Sow, P. K., Zahiri, B., & Mérida, W. (2019). Assessment and Interpretation of Surface Wettability Based on Sessile Droplet Contact Angle Measurement: Challenges and Opportunities. In *Advanced Materials Interfaces* (Vol. 6, Issue 18). Wiley-VCH Verlag. https://doi.org/10.1002/admi.201900839

22. Miranda, M. I. G., Bica, C. I. D., Nachtigall, S. M. B., Rehman, N., & Rosa, S. M. L. (2013). Kinetical thermal degradation study of maize straw and soybean hull celluloses by simultaneous DSC-TGA and MDSC techniques. *Thermochimica Acta*, *565*, 65–71. https://doi.org/10.1016/j.tca.2013.04.012

23. Rasoulianboroujeni, M., Fahimipour, F., Shah, P., Khoshroo, K., Tahriri, M., Eslami, H., Yadegari, A., Dashtimoghadam, E., & Tayebi, L. (2019). Development of 3D-printed PLGA/TiO 2 nanocomposite scaffolds for bone tissue engineering applications. *Materials Science and Engineering C*, *96*, 105–113. https://doi.org/10.1016/j.msec.2018.10.077

24. Kim, S. H., Mun, C. H., Jung, Y., Kim, S. H., Kim, D. I., & Kim, S. H. (2013). Mechanical properties of compliant double layered poly(L-lactide-co-ε- caprolactone) vascular graft. *Macromolecular Research*, *21*(8), 886–891. https://doi.org/10.1007/s13233-013-1095-5

25. British Standards Institution. (2017). *Cardiovascular implants and extracorporeal systems - vascular prostheses - tubular vascular grafts and vascular patches*. British Standards Institution.

26. Stojko, M., Włodarczyk, J., Sobota, M., Karpeta-Jarząbek, P., Pastusiak, M., Janeczek, H., Dobrzyński, P., Starczynowska, G., Orchel, A., Stojko, J., Batoryna, O., Olczyk, P., Komosińska-Vassev, K., Olczyk, K., & Kasperczyk, J. (2020). Biodegradable electrospun nonwovens releasing propolis as a promising dressing material for burn wound treatment. *Pharmaceutics*, *12*(9), 1–18. https://doi.org/10.3390/pharmaceutics12090883

27. Nitti, P., Gallo, N., Natta, L., Scalera, F., Palazzo, B., Sannino, A., & Gervaso, F. (2018). Influence of nanofiber orientation on morphological and mechanical properties of electrospun chitosan mats. *Journal of Healthcare Engineering* 2018 (November). https://doi.org/10.1155/2018/3651480

28. Baji, A., Mai, Y. W., Wong, S. C., Abtahi, M., & Chen, P. (2010). Electrospinning of polymer nanofibers: Effects on oriented morphology, structures and tensile properties. In *Composites Science and Technology* (Vol. 70, Issue 5, pp. 703–718). Elsevier Ltd. https://doi.org/10.1016/j.compscitech.2010.01.010

29. Hu, J. J., Chao, W. C., Lee, P. Y., & Huang, C. H. (2012). Construction and characterization of an electrospun tubular scaffold for small-diameter tissue-engineered vascular grafts: A scaffold membrane approach. *Journal of the Mechanical Behavior of Biomedical Materials*, *13*, 140–155. https://doi.org/10.1016/j.jmbbm.2012.04.013

30. Duan, Y., Kalluri, L., Satpathy, M., & Duan, Y. (2021). Effect of Electrospinning Parameters on the Fiber Diameter and Morphology of PLGA Nanofibers. *Dental Oral Biology and Craniofacial Research*, 1–7. https://doi.org/10.31487/j.dobcr.2021.02.04

31. Xu, Y., Zou, L., Lu, H., & Kang, T. (2017). Effect of different solvent systems on PHBV/PEO electrospun fibers. *RSC Advances*, *7*(7), 4000–4010. https://doi.org/10.1039/c6ra26783a

32. Milleret, V., Hefti, T., Hall, H., Vogel, V., & Eberli, D. (2012). Influence of the fiber diameter and surface roughness of electrospun vascular grafts on blood activation. *Acta Biomaterialia*, *8*(12), 4349–4356. https://doi.org/10.1016/j.actbio.2012.07.032

33. Ko, Y. G., Park, J. H., Lee, J. B., Oh, H. H., Park, W. H., Cho, D., & Kwon, O. H. (2016). Growth behavior of endothelial cells according to electrospun poly(D,L-lactic-co-glycolic acid) fiber diameter as a tissue engineering scaffold. *Tissue Engineering and Regenerative Medicine*, *13*(4), 343–351. https://doi.org/10.1007/s13770-016-0053-7

34. You, Y., Min, B. M., Lee, S. J., Lee, T. S., & Park, W. H. (2005). In vitro degradation behavior of electrospun polyglycolide, polylactide, and poly(lactide-co-glycolide). *Journal of Applied Polymer Science*, *95*(2), 193–200. https://doi.org/10.1002/app.21116

35. Herrero-Herrero, M., Gómez-Tejedor, J. A., & Vallés-Lluch, A. (2018). PLA/PCL electrospun membranes of tailored fibres diameter as drug delivery systems. *European Polymer Journal*, *99*, 445–455. https://doi.org/10.1016/j.eurpolymj.2017.12.045

36. Alfaro De Prá, M. A., Ribeiro-do-Valle, R. M., Maraschin, M., & Veleirinho, B. (2017). Effect of collector design on the morphological properties of polycaprolactone electrospun fibers. *Materials Letters* 193, 154–157. https://doi.org/10.1016/j.matlet.2017.01.102

37. Yuan, H., Zhou, Q., & Zhang, Y. (2017). Improving fiber alignment during electrospinning. Mehdi Afshari (Ed), *Electrospun Nanofibers*, Woodhead Publishing - Elsevier Inc., 125–147. https://doi.org/10.1016/B978-0-08-100907-9.00006-4

38. Robinson, A. J., Pérez-Nava, A., Ali, S. C., González-Campos, J. B., Holloway, J. L., & Cosgriff-Hernandez, E. M. (2021). Comparative analysis of fiber alignment methods in electrospinning. In *Matter* (Vol. 4, Issue 3, pp. 821–844). Cell Press. https://doi.org/10.1016/j.matt.2020.12.022

39. Konig, G., McAllister, T. N., Dusserre, N., Garrido, S. A., Iyican, C., Marini, A., Fiorillo, A., Avila, H., Wystrychowski, W., Zagalski, K., Maruszewski, M., Jones, A. L., Cierpka, L., de la Fuente, L. M., & L'Heureux, N. (2009). Mechanical properties of completely autologous human tissue engineered blood vessels compared to human saphenous vein and mammary artery. *Biomaterials* 30(8), 1542–1550. https://doi.org/10.1016/j.biomaterials.2008.11.011

40. Jin, X., Geng, X., Jia, L., Xu, Z., Ye, L., Gu, Y., … Feng, Z. G. (2019). Preparation of Small-Diameter Tissue-Engineered Vascular Grafts Electrospun from Heparin End-Capped PCL and Evaluation in a Rabbit Carotid Artery Replacement Model. *Macromolecular Bioscience* 19(8). https://doi.org/10.1002/mabi.201900114

41. Yu, Y. H., Lee, D., Hsu, Y. H., Chou, Y. C., Ueng, S. W. N., Chen, C. K., & Liu, S. J. (2020). A three-dimensional printed polycaprolactone scaffold combined with co-axially electrospun vancomycin/ceftazidime/bone morphological protein-2 sheath-core nanofibers for the repair of segmental bone defects during the masquelet procedure. *International Journal of Nanomedicine*, *15*, 913–925. https://doi.org/10.2147/IJN.S238478

42. Zhan, J., Xu, H., Zhong, Y., Wu, Q., & Liu, Z. (2020). Surface modification of patterned electrospun nanofibrous films via the adhesion of DOPA-bFGF and DOPA-ponericin G1 for skin wound healing. *Materials and Design*, *188*. https://doi.org/10.1016/j.matdes.2019.108432

43. Hua, Y., Su, Y., Zhang, H., Liu, N., Wang, Z., Gao, X., Gao, J., & Zheng, A. (2021). Poly(lactic-co-glycolic acid) microsphere production based on quality by design: a review. *Drug Delivery*, *28*(1), 1342–1355. https://doi.org/10.1080/10717544.2021.1943056

44. Ji Lee, E., Ho Lee, J., Cheol Shin, Y., Hwang, D.-G., Soo Kim, J., Seong Jin, O., Jin, L., Won Hong, S., & Han, D.-W. (2014). Graphene Oxide-decorated PLGA/Collagen Hybrid Fiber Sheets for Application to Tissue Engineering Scaffolds. In *Biomater. Res* (Vol. 18, Issue 1).

45. Oztemur, J., Ozdemir, S., & Yalcin-Enis, I. (2022). Effect of blending ratio on morphological, chemical, and thermal characteristics of PLA/PCL and PLLA/PCL electrospun fibrous webs. *International Journal of Polymeric Materials and Polymeric Biomaterials*. https://doi.org/10.1080/00914037.2022.2090356

46. Mehrasa, M., Asadollahi, M. A., Ghaedi, K., Salehi, H., & Arpanaei, A. (2015). Electrospun aligned PLGA and PLGA/gelatin nanofibers embedded with silica nanoparticles for tissue engineering. *International Journal of Biological Macromolecules*, *79*, 687–695. https://doi.org/10.1016/j.ijbiomac.2015.05.050

47. Zamani, F., Latifi, M., Amani-Tehran, M., & Shokrgozar, M. A. (2013). Effects of PLGA nanofibrous scaffolds structure on nerve cell directional proliferation and morphology. *Fibers and Polymers*, *14*(5), 698–702. https://doi.org/10.1007/s12221-013-0698-y

48. Nath, S. D., Son, S., Sadiasa, A., Min, Y. K., & Lee, B. T. (2013). Preparation and characterization of PLGA microspheres by the electrospraying method for delivering simvastatin for bone regeneration. *International Journal of Pharmaceutics*, *443*(1–2), 87–94. https://doi.org/10.1016/j.ijpharm.2012.12.037

49. Silva, A. T. C. R., Cardoso, B. C. O., Silva, M. E. S. R. e, Freitas, R. F. S., & Sousa, R. G. (2015). Synthesis, Characterization, and Study of PLGA Copolymer *in Vitro* Degradation. *Journal of Biomaterials and Nanobiotechnology*, *06*(01), 8–19. https://doi.org/10.4236/jbnb.2015.61002

50. Masaeli, R., Kashi, T. S. J., Dinarvand, R., Tahriri, M., Rakhshan, V., & Esfandyari-Manesh, M. (2016). Preparation, Characterization and Evaluation of Drug Release Properties of Simvastatin-loaded PLGA Microspheres. In *Shaheed Beheshti University of Medical Sciences and Health Services Iranian Journal of Pharmaceutical Research*.

51. Enis, I. Y., Vojtech, J., & Sadikoglu, T. G. (2017). Alternative solvent systems for polycaprolactone nanowebs via electrospinning. *Journal of Industrial Textiles*, *47*(1), 57–70. https://doi.org/10.1177/1528083716634032

52. Hasan, M. A., Zaki, M. I., & Pasupulety, L. (2002). *Oxide-catalyzed conversion of acetic acid into acetone: an FTIR spectroscopic investigation*.

53. Oztemur, J., & Yalcin-Enis, I. (2021). Development of biodegradable webs of PLA/PCL blends prepared via electrospinning: Morphological, chemical, and thermal characterization. *Journal of Biomedical Materials Research - Part B Applied Biomaterials*, *109*(11), 1844–1856. https://doi.org/10.1002/jbm.b.34846

54. Hadjizadeh, A., Ajji, A., & Bureau, M. N. (2011). Nano/micro electro-spun polyethylene terephthalate fibrous mat preparation and characterization. *Journal of the Mechanical Behavior of Biomedical Materials*, *4*(3), 340–351. https://doi.org/10.1016/j.jmbbm.2010.10.014

55. Helling, A. L., Viswanathan, P., Cheliotis, K. S., Mobasseri, S. A., Yang, Y., El Haj, A. J., & Watt, F. M. (2019). Dynamic Culture Substrates That Mimic the Topography of the Epidermal-Dermal Junction. *Tissue Engineering - Part A*, *25*(3–4), 214–223. https://doi.org/10.1089/ten.tea.2018.0125

56. Sechi, M., Vanna, S., Roggio, A. M., Siliani, Massimo, P., Salvatore, M., & Mariani, A. (2012). Development of novel cationic chitosan- and anionic alginate–coated poly(D,L-lactide-co-glycolide) nanoparticles for controlled release and light protection of resveratrol. *International Journal of Nanomedicine*, 5501-5516. https://doi.org/10.2147/IJN.S36684

57. Vasita, R., Mani, G., Agrawal, C. M., & Katti, D. S. (2010). Surface hydrophilization of electrospun PLGA micro-/nano-fibers by blending with Pluronic® F-108. *Polymer*, *51*(16), 3706–3714. https://doi.org/10.1016/j.polymer.2010.05.048

58. Cohn, D., & Hotovely Salomon, A. (2005). Designing biodegradable multiblock PCL/PLA thermoplastic elastomers. *Biomaterials*, *26*(15), 2297–2305. https://doi.org/10.1016/j.biomaterials.2004.07.052

59. Park, P. I. P., & Jonnalagadda, S. (2006). Predictors of glass transition in the biodegradable polylactide and poly-lactide-co-glycolide polymers. *Journal of Applied Polymer Science*, *100*(3), 1983–1987. https://doi.org/10.1002/app.22135

60. Peng, Z., Ye, L., & Ade, H. (2022). Understanding, quantifying, and controlling the molecular ordering of semiconducting polymers: From novices to experts and amorphous to perfect crystals. In *Materials Horizons* (Vol. 9, Issue 2, pp. 577–606). Royal Society of Chemistry. https://doi.org/10.1039/d0mh00837k

61. Yalcin Enis, I., Horakova, J., Gok Sadikoglu, T., Novak, O., & Lukas, D. (2017). Mechanical investigation of bilayer vascular grafts electrospun from aliphatic polyesters. *Polymers for Advanced Technologies* 28(2), 201–213. https://doi.org/10.1002/pat.3875

62. Wu, H., Fan, J., Chu, C. C., & Wu, J. (2010). Electrospinning of small diameter 3-D nanofibrous tubular scaffolds with controllable nanofiber orientations for vascular grafts. *Journal of Materials Science: Materials in Medicine*, *21*(12), 3207–3215. https://doi.org/10.1007/s10856-010-4164-8

63. Nezarati, R. M., Eifert, M. B., Dempsey, D. K., & Cosgriff-Hernandez, E. (2015). Electrospun vascular grafts with improved compliance matching to native vessels. *Journal of Biomedical Materials Research - Part B Applied Biomaterials* 103(2), 313–323. https://doi.org/10.1002/jbm.b.33201

64. Rodriguez-Soto, M. A., Suarez, N. A., Riveros, A., Garcia-Brand, A. J., Munoz-Camargo, C., Cruz, J. C., & Briceno, J. C. (2021). Mechanical characterization of novel vascular grafts: Approaching to the native vessel behavior. *2021 IEEE 2nd International Congress of Biomedical Engineering and Bioengineering, CI-IB and BI 2021*. https://doi.org/10.1109/CI-IBBI54220.2021.9626102

65. Tang, J., Bao, L., Li, X., Chen, L., & Hong, F. F. (2015). Potential of PVA-doped bacterial nano-cellulose tubular composites for artificial blood vessels. *Journal of Materials Chemistry B*, *3*(43), 8537–8547. https://doi.org/10.1039/c5tb01144b

66. Caves, J. M., Kumar, V. A., Martinez, A. W., Kim, J., Ripberger, C. M., Haller, C. A., & Chaikof, E. L. (2010). The use of microfiber composites of elastin-like protein matrix reinforced with synthetic collagen in the design of vascular grafts. *Biomaterials*, *31*(27), 7175–7182. https://doi.org/10.1016/j.biomaterials.2010.05.014

67. Chaparro, F. J., Matusicky, M. E., Allen, M. J., & Lannutti, J. J. (2016). Biomimetic microstructural reorganization during suture retention strength evaluation of electrospun vascular scaffolds. *Journal of Biomedical Materials Research - Part B Applied Biomaterials*, *104*(8), 1525–1534. https://doi.org/10.1002/jbm.b.33493

68. Grasl, C., Stoiber, M., Röhrich, M., Moscato, F., Bergmeister, H., & Schima, H. (2021). Electrospinning of small diameter vascular grafts with preferential fiber directions and comparison of their mechanical behavior with native rat aortas. *Materials Science and Engineering C* 124. https://doi.org/10.1016/j.msec.2021.112085

69. Ercolani, E., del Gaudio, C., & Bianco, A. (2015). Vascular tissue engineering of small-diameter blood vessels: Reviewing the electrospinning approach. *Journal of Tissue Engineering and Regenerative Medicine* 9(8), 861–888. https://doi.org/10.1002/term.1697

Environmentally Friendly Approach for Decolorization Textile Wastewater by Nanobubble Water Technology and Enzymes

Pervin Anis[1] 0000-0002-6295-637X
Tuba Toprak-Cavdur[1*] 0000-0001-8475-3197
Sibel Şardağ[1] 0000-0001-9177-0059
Bilge İncekara[2] 0000-0003-3263-7869

[1] Bursa Uludag University / College of Engineering / Department of Textile Engineering / Bursa / Türkiye
[2] Bursalı Grubu / R&D center / Bursa / Türkiye

Corresponding Author: Tuba Toprak-Cavdur, tubatoprak@uludag.edu.tr

ABSTRACT

One of the most important issues about textile industry is its negative environmental impacts because of the pollution produced. Herein, decolorization processes of different-colored reactive dyeing baths using eco-friendly ways; nanobubbles and enzymes, was discussed. Decolorizations were evaluated by examining the transmittance and chemical oxygen demands of the treated wastewater baths were measured. The results showed that nanobubbles could be used in decolorization while laccase and peroxidase enzymes increased the decolorization effect of nanobubbles. In addition to the decolorizing effect of nanobubbles, it was an important environmental advantage that the corresponding process provided lower chemical oxygen demand than that in the untreated wastewater. The results of the study reveal that it is possible to use nanobubble in decolorization and this technology is an important wastewater treatment technology in protecting the environment by reducing the chemical oxygen demand of wastewater.

1. INTRODUCTION

The history of nanobubbles (NBs), which are fine bubbles less than 1 μm in diameter [1], began in 1950 with the Epstein-Plesset theory [2]. Research studies and discussions about NBs still continue today. Examples of these are the longevity of NBs in water and short-life paradox predicted in Epstein-Plesset theory [3–6]. A successful theoretical model was developed by Epstein and Plesset in 1950 that explained the dissolution of gas bubbles in liquids using Laplace equation and diffusion theory [7]. According to this theory, which seems to deny the stable existence of nanoscale gas bubbles in liquids, a 100 nm radius bubble with an internal pressure of approximately 14.4 times atmospheric pressure cannot stay for less than 1 μs [2]. Many studies have been conducted on this subject in the following years. The concept of nanobubbles was reproposed [8]. The aim of this proposal was to provide an explanation about the long-range attractive forces between two hydrophobic surfaces in aqueous solution. In the 2000s, direct observations of surface NBs were conducted [9,10] and they were found to be quite stable on surfaces in water solutions [11–13]. NBs are characterized by mass transfer efficiency, high zeta potential, producing high dissolved oxygen concentration, and large specific surface area [1,14,15]. The nanobubble (NB) technology has been used in health protection, mineral flotation, aquaculture, agricultural cultivation, and many other fields in recent years [16–20]. It is generally used in wastewater treatment in textile [21–24] because NBs decompose organic substances by generating free radicals, such as hydroxyl (•OH) [25]. Their high oxidizing power can degrade even pollutants that do not readily decompose under normal

To cite this article: Anis P, Toprak-Cavdur T, Şardağ S, İncekara B. 2024. Environmentally friendly approach for decolorization textile wastewater by nanobubble water technology and enzymes. *Tekstil ve Konfeksiyon,* 34(3), 231-243.

conditions [26]. In addition, NBs have recently been used in dyeing and finishing processes [27–29].

The increasing demand for dyes derived only from natural sources before 1856 and the exorbitant costs of extracting dyes led to the discovery of the first synthetic dye in 1856 [30]. Since then, the industries depended on synthetic dyes have expanded, producing approximately 8×10^5 tons of dye per year [31,32]. Textile has an approximate share of 75% in this market and contains about ten thousand different dyes [30,33].

Reactive dyes, as the most popular dye class for cotton dyeing [34], due to the variety of brilliant shades, ease of application, excellent color fastness, and low price [35–37], are used in more than 50% of cotton dyeing [38]. In reactive dyeing, exhaustion agents are used to overcome the repulsion between dye - fiber [39,40]. Dye molecules that form covalent bonds with the hydroxyl groups of the cellulose under alkaline conditions provide high wet fastness [41,42]. In reactive dyeing performed in alkaline conditions, fixation and hydrolysis of reactive dyes are in competition, and a high fixation/hydrolysis ratio is required for efficient dyeing [43]. Hydrolyzed dyes that lose their power to react with the fiber are loosely held on the fiber. If these dyes and superficial dyes are not removed during soaping and washing, involving various rinses and washings [44], low washing fastnesses are obtained [45]. The wastewater from the reactive dyeing process of cotton contains 20-50% of the applied dyes in hydrolyzed forms, which cannot be recovered [41]. That is, reactive dyeing is characterized not only by high electrolyte and alkali concentrations [46,47], but also by color [48,49]. In addition, dyeing cotton with reactive dyes consumes the ighest volume of water per kilogram of any fiber [50]. Consequently, in terms of environmental impact, reactive dyeing is a water-intensive dyeing and its wastewater discharged is highly polluted.

Dye-containing wastewater in textile industries is a major threat to humans and the environment due to the complex chemical structures of dyes, high pH, biological and chemical oxygen demands, and their presence in all kinds of complex matrices [51,52]. Recently, reuse, recovery and decolorization of dyeing wastewater has attracted great attention due to water scarcity in addition to these reasons. Textile dye wastewater treatment techniques have been categorized as chemical, physical, biological and their combinations [53,54]. While the physical treatment of industrial wastewater is oxidation, ion exchange, adsorption, and filtration [55]; chemical treatment includes various processes, including ozonation, coagulation, flocculation and chemical oxidation [56]. The biodegradation process occurs naturally through various microorganisms found in wastewater [57] and enzymes [58].

The motivation of this study is to examine the decolorization of reactive dyeing wastewater generated in the industry as one of the four important stakeholders (consumers, retailers, industry, and policymakers) for a more sustainable textile production by various methods. In this context, the decolorization of dyeing wastewater with NBs, as a new water technology, and enzymes, as a completely environmentally friendly technology, were examined. The effects of the decolorization processes on the wastewater of the dyeings carried out in three different shades with different colors were evaluated by transmittance measurements. Chemical oxygen demand measurements of some bathrooms were used to analyze decolorization methods from an environmental perspective.

2. MATERIAL AND METHOD

2.1 Material

The hydrogen peroxide (H_2O_2-50%) used in decolorization has a concentration of 50% and was obtained from Akkim. Sodium hydroxide (NaOH) and acetic acid (CH_3COOH) were also obtained from the same company. Two different enzymes used for decolorization, laccase (Novalite Cold) and peroxidase (Denilite Cold), were purchased from Alfa Kimya. It has been suggested that laccase should be used at pH 4.5–5.5 at 65°C–70°C and peroxidase at pH 4.5–5 at 20°C–55°C. Names and content of dyes are given in Table 1. Everzol, which was one of the reactive dyes, was obtained from İlteks Boya ve Kimyevi Maddeler San. ve Tic. A.Ş. (Istanbul, Turkey), Synazol and Kimsoline from Eksoy Kimya (Adana, Turkey) and Itofix from ITK Tekstil Kimya Ltd. Şti. (Istanbul, Turkey).

Nanobubble generator was obtained from BSTWATER company. In the generator, the air flow was 3 L/min, the water flow was 5 m³/hour, the water pressure was 2-2.2 bar and the air pressure was 7-8 bar. Air and water flow rates were controlled by flowmeters, and air and water pressures were controlled by manometers.

2.2 Method

The temperature-time diagram of the reactive dyeing of cotton products is given in Figure 1, and that of the reactive washing process is shown in Figure 2.

Composite wastewater samples (C) were prepared by taking 10 ml from each of the dyeing bath and subsequent washing baths, that is, the ratio of each bath in the composite sample was 12.5%. The decolorization processes applied to these composite samples were nanobubbles (NBs) and nanobubbles+enzymatic (NBs-E) processes. In the NBs process, composite samples were passed through the NB generator at 30' (NBs-30'), 60' (NBs-60') and 90' (NBs-90'). NBs-E decolorization of the composite wastewater samples prepared by passing 60 minutes through the NB generator was performed with laccase (NBs-E-L),

peroxidase (NBs-E-P) and hydrogen peroxide+peroxidase (NBs-H$_2$O$_2$-E-P). In the NBs-E-L and NBs-E-P processes, laccase and peroxidase enzymes were added at the concentrations of 1 g/L, 2 g/L and 4 g/L to NBs-60' and composite wastewater sample baths whose pH was adjusted to 4.5 with acetic acid. These baths were treated with laccase and peroxidase enzymes for one hour at 65°C and 50°C, respectively. The only difference of the NBs-H$_2$O$_2$-E-P from the NBs-E-P was the addition of 3g/L H$_2$O$_2$ to the baths as well as the enzyme. For comparison, all decolorization processes were performed with the addition of enzymes/hydrogen peroxide at similar concentrations to the composite sample without NBs applied (C-E-L, C-E-P, C-H$_2$O$_2$-E-P). Wet treatments were carried out in ATAC HT-16 sample dyeing machine at a liquor ratio of 50:1.

Table 1. Details of colors

| Color	Shade	Content of the color	% Dye conc.
Fuchsia	Light	Synazol Red HF-3B Kimsolin Red HF 6BN %150 (Reactive Red 195)	0.032
Navy blue		Everzol Yellow ED-R Everzol Red ED7BN Everzol Navy ED (Reactive Blue 222)	0.02
Green	Medium	Synazol Yellow HF 4 GL %150 (Reactive Yellow 160) Synazol Blue K BR Itofix Turq Blue G (N) 266% (Reactive Blue 21)	1.64
Purple		Everzol Yellow ED-R Everzol Red ED-3B (Reactive Red 195) Everzol Blue L-ED (Reactive Blue 221)	1.66
Red	Dark	Everzol Yellow ED-R Everzol Red ED-3B (Reactive Red 195)	2.97
Blue		Everzol Yellow ED-R Everzol Red ED7BN Everzol Navy ED (Reactive Blue 222)	2.77
Black		Everzol Yellow ED-R Everzol Red ED7BN Everzol Black ED-G	2.66
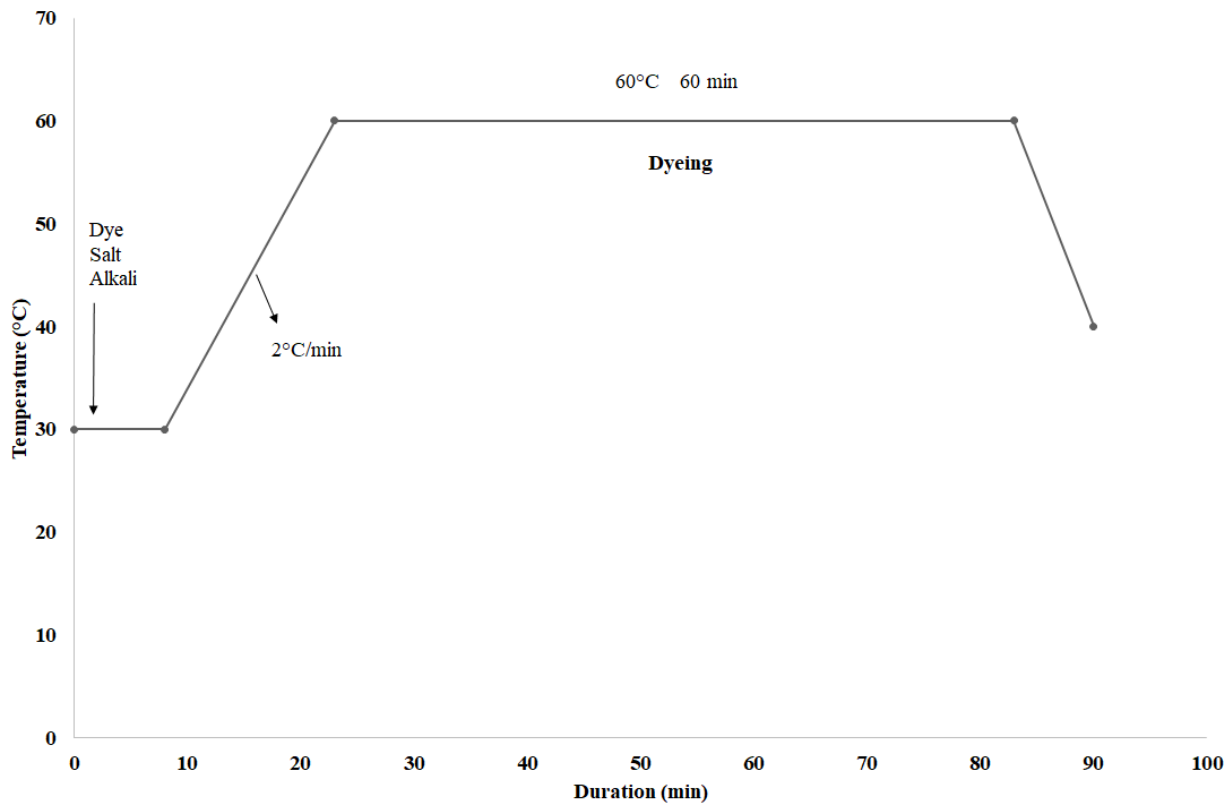
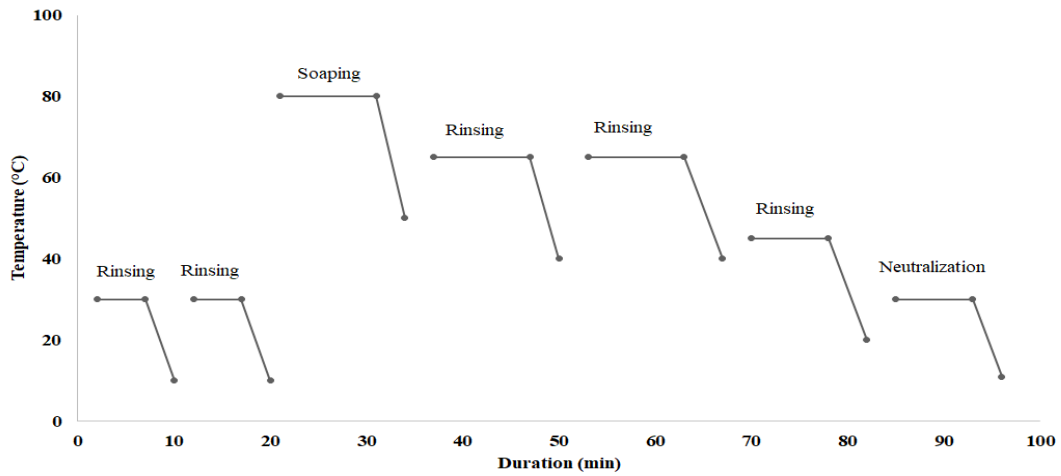**Figure 1.** Temperature-time diyagram of reactive dyeing

Figure 2. Temperature-time diagram of reactive washing

The transmittance measurements of the samples after decolorization processes were measured in the wavelength range of 400-700 nm using the Datacolor 800 L spectrophotometer. Measurements were recorded at 5 nm intervals. The differences between the transmittance values of the baths were calculated according to Equation (1).

$$\%\Delta T = [(T_2 - T_1) / T_1] \times 100 \tag{1}$$

In this equation, T_1 and T_2 were transmittance values before and after decolorization processes, respectively.

Chemical oxygen demand (COD) measurements of some wastewater samples after decolorization processes were conducted using Merck Millipore COD cell test, WTW CR 2200 thermoreactor, and photoLab S12 photometer.

3. RESULTS AND DISCUSSION

3.1 Decolorization

3.1.1 Decolorization of light shade dyeings

Transmittance values and baths images of the decolorization processes performed with different methods after the light shade dyeings are shown in Figure 3 and Figure 4, respectively. The wavelengths at which the maximum absorbance values of baths were taken in this study were 520 nm and 410 nm, for fuchsia and navy blue, respectively.
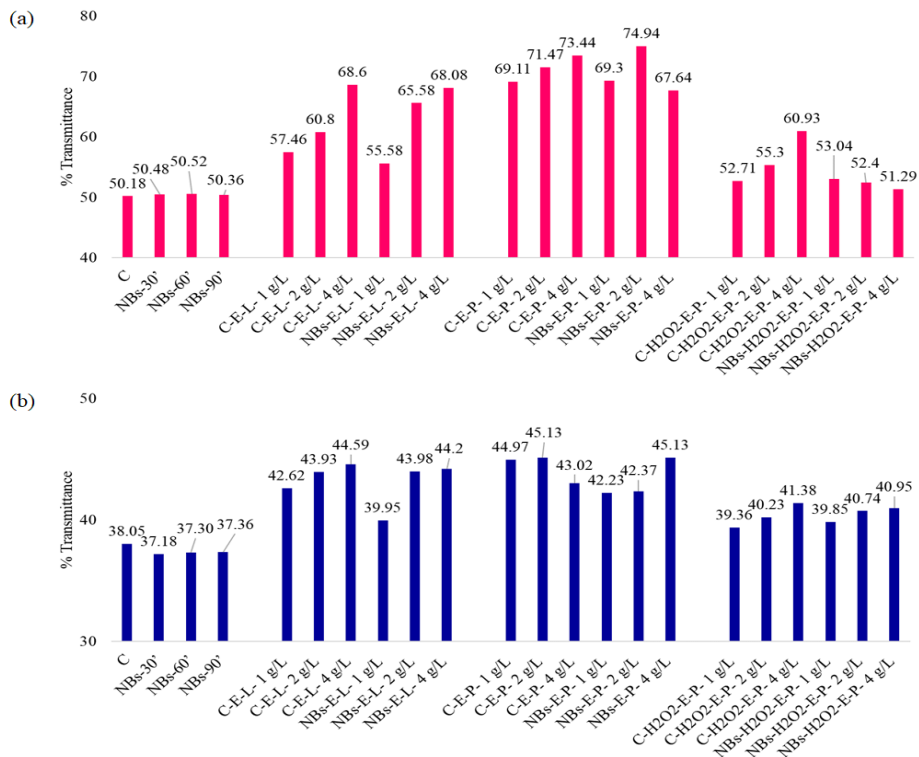

Figure 3. Transmittance values of the decolorization processes of light shade dyeings: (a) fuchsia, (b) navy blue

Figure 4. Images of the decolorization processes of light shade fuchsia (top) and navy blue (bottom) dyeings:
(a) NBs, (b) C/NBs-E-L, (c) C/NBs-E-P, (d) C/NBs-H$_2$O$_2$-E-P

All of the decolorization methods performed after fuchsia and dark blue dyeing increased the transmittance values compared to the C. The effectiveness of nanobubbles in color removal increased with their use with enzymes. Especially, enzymes increased the transmittance values of the baths in which they were used. Peroxidase enzymes were more effective in color removal than laccases. There was information in the literature that higher decolorization levels were achieved with peroxidases than with laccases [59]. The highest transmittance values were obtained from treatments with peroxidase (C/NBs-E-P-). Hydrogen peroxide added to the decolorization baths along with the peroxidase enzyme produced lower transmittance than the process in which enzyme was used alone. It was seen that hydrogen peroxide could have inactivated peroxidase enzyme as stated in literature [60,61]. In addition, increasing concentrations of enzymes generally increased bath transmittance. Transmittance values obtained from C-E- and NBs-E- processes were generally similar. Comparison of decolorization by color showed that overall higher transmittance values were obtained from fuchsia compared to navy blue. The color removal effect of enzymes at different level for two colors could have explained by the substrate specificity of the enzymes [62].

It was thought that the chemical structure of fuchsia was more compatible with the substrate on which the peroxidase enzyme was effective. In fuchsia, especially after decolorization with peroxidase, it was observed that the colors of the baths were almost completely removed (Figure 4). The highest transmittance value in fuchsia 74.94 was obtained from the bath treated with 2 g/L peroxidase in the presence of NBs. For dark blue, it was interpreted that NBs could not effective in decolorization, which was evaluated according to transmittance, due to the color shifts that occurred especially after decolorization with NBs-. Overall, 60 minutes would be sufficient for decolorization with NBs.

3.1.2 Decolorization of medium shade dyeings

Transmittance values and baths images of the decolorization processes performed with different methods after the medium shade dyeings are shown in Figure 5 and Figure 6, respectively. The wavelengths at which the maximum absorbance values of baths were 420 nm and 540 nm for green and purple, respectively.

All of the decolorization methods performed after dyeing increased the transmittance values of both colors compared to C. The use of NBs- with enzymes (NBs-E-) on the decolorization efficiency was more effective than the process in which NBs used alone. It has been stated in the literature that NBs increase enzyme activity because they are very effective in oxygen mass transfer in the liquid phase [63]. It was also thought that the color removal efficiency would be higher if NBs were used with a positive charge[21]. Similar to the decolorization processes carried out with enzymes in light shade dyeings (Figure 3), the highest transmittance values of medium shade dyeings were obtained from the decolorization with peroxidase. This case could have been explained by the substrate specificity of the enzymes [62]. This result suggested that the chemical structure of green and purple were more suitable to the substrate of the peroxidase enzyme compared to those of laccase. Moreover, it was thought that the activity of laccase and even peroxidase could have been further improved in the presence of a mediator [59]. The bath images in Figure 6 showed that NBs/C-E-P 4g/L treated bath had the lowest colorfulness. With hydrogen peroxide+peroxidase (C/NBs-H_2O_2-E-P-), lower transmittance values were obtained compared to the decolorization in which peroxidase (C/NBs-E-P-) was used alone. Hydrogen peroxide could have effected peroxidase by inactivating [60,61]. Increasing concentrations of enzymes generally increased the bath transmittance of both colors. Although, the transmittance data of NBs-E- and C-E- processes were comparable, higher values were obtained from the NBs-E- process than that of the C-E- in the decolorization of green.
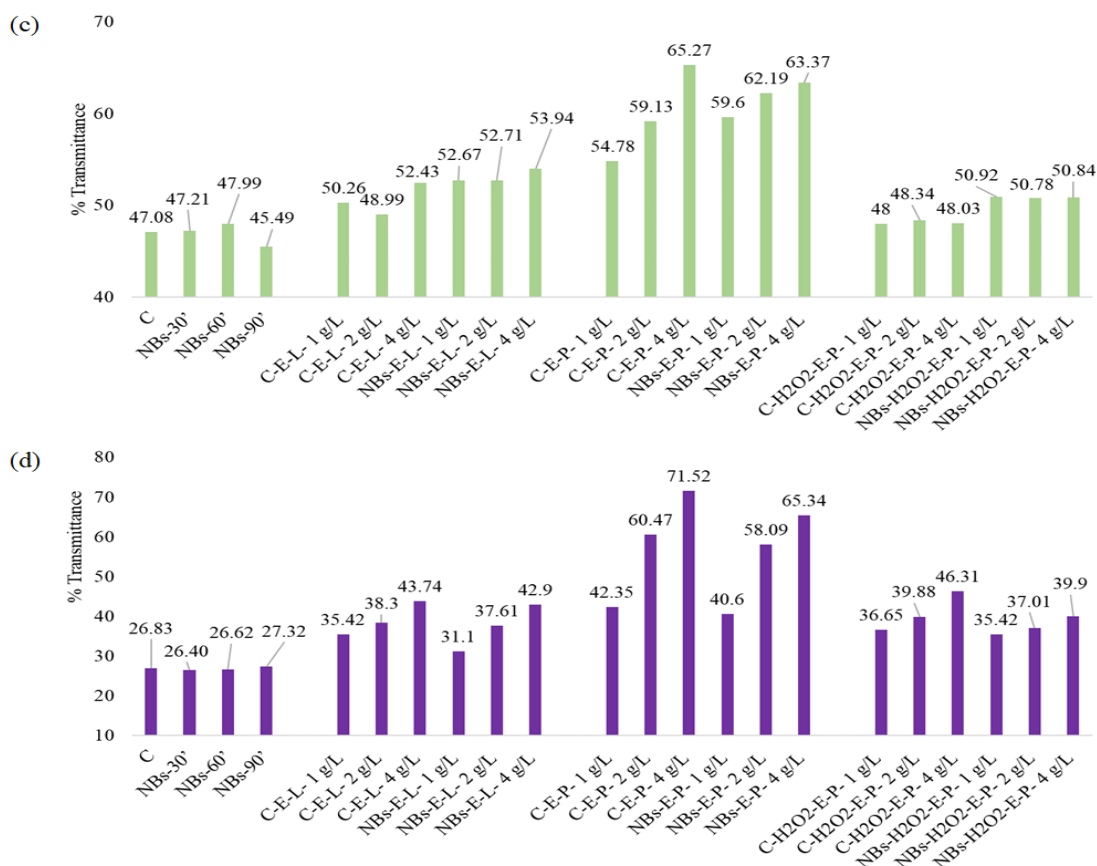

Figure 5. Transmittance values of the decolorization processes of medium shade dyeings: (c) green, (d) purple
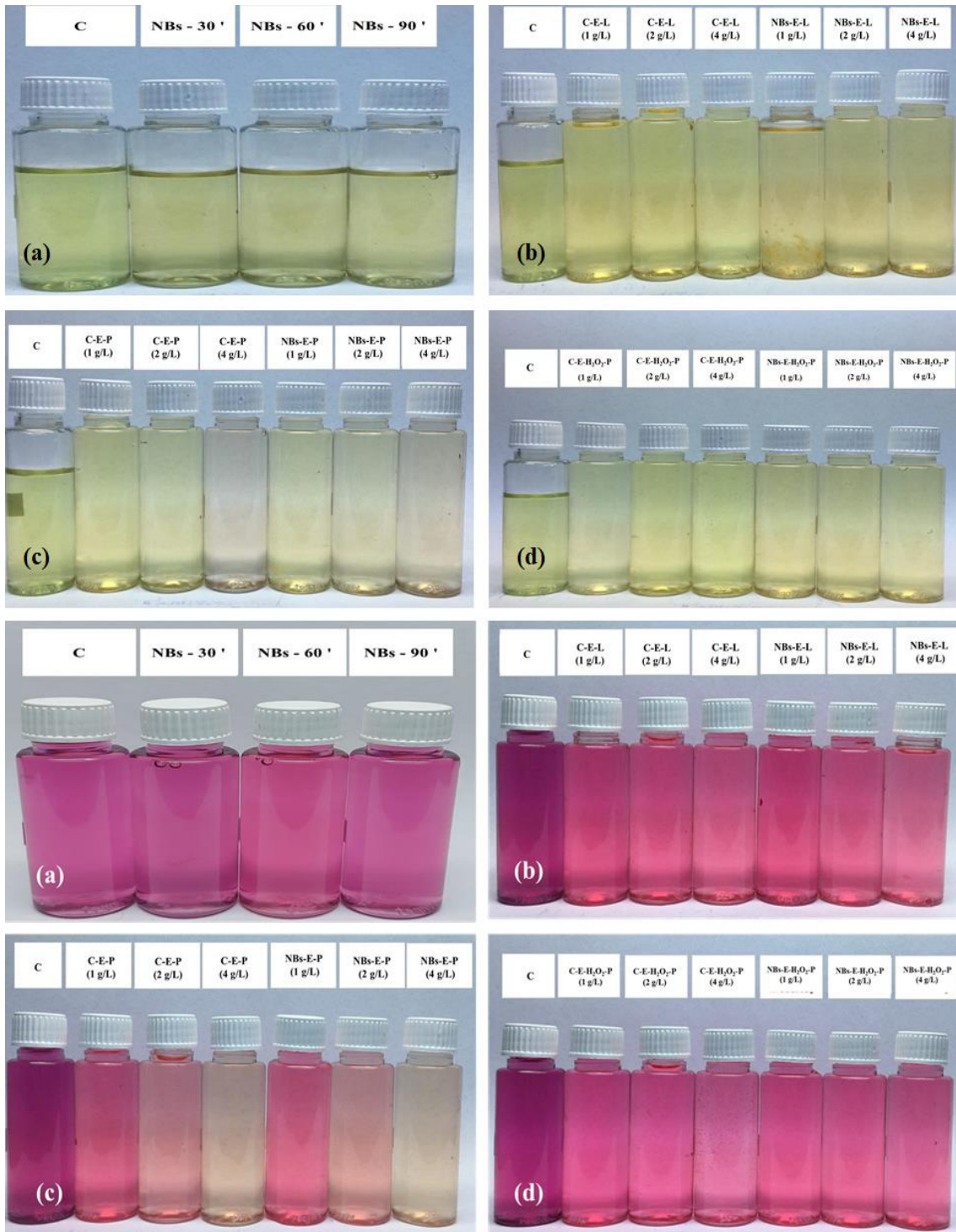
Figure 6. Images of the decolorization processes of medium shade green (top) and purple (bottom) dyeings:
(a) NBs, (b) C/NBs-E-L, (c) C/NBs-E-P, (d) C/NBs-H$_2$O$_2$-E-P

3.1.3 Decolorization of dark shade dyeings

Transmittance values and baths images of the decolorization processes performed with different methods after the dark shade dyeings are shown in Figure 7 and Figure 8, respectively. The maximum absorbance wavelengths used in transmittance measurements are as follows, according to colors: 590 nm for blue, 420 nm for red, 590 nm for black.
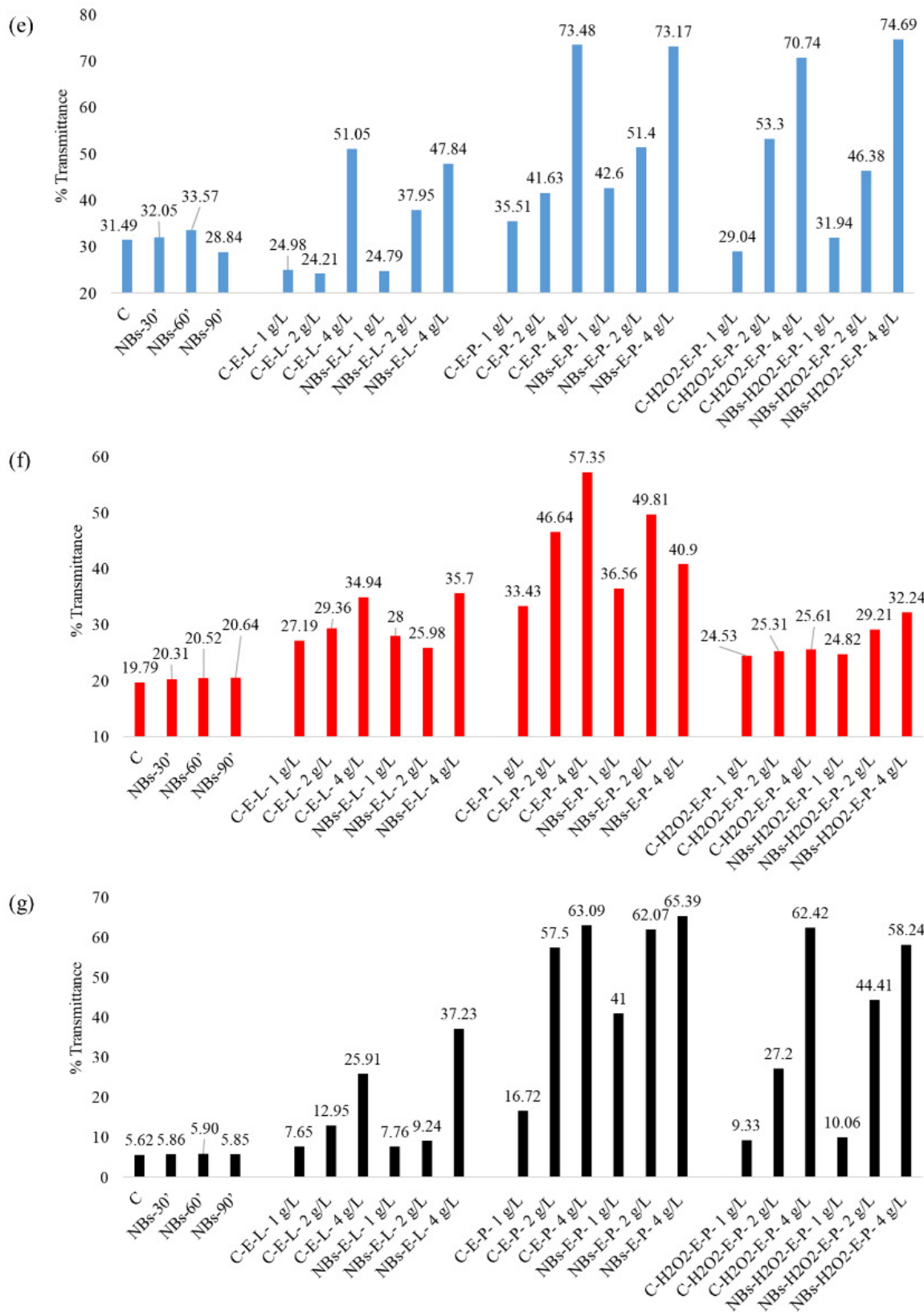
Figure 7. Transmittance values of the decolorization processes of dark shade dyeings: (e) blue, (f) red, (g) black

Figure 8. Images of the decolorization processes of dark shade blue (top), red (middle), and black (bottom) dyeings: (a) NBs, (b) C/NBs-E-L, (c) C/NBs-E-P, (d) C/NBs-H₂O₂-E-P

Each of the decolorization methods increased the transmittance values of red and black colors compared to C. The reason why this case was not true for blue color was interpreted as decolorization caused color changes rather than color removing (Figure 8). The decolorization efficiency of NBs when used alone could have been increased by making them positively charged [21]. It was observed that usage of enzymes with NBs (NBs-E-) increased the decolorization efficiency. Since NBs increased enzyme activities, the use of enzymes with NBs provided higher rates of color removal [63]. The highest transmittance values in red and black colors were obtained from decolorization with peroxidase (C/NBs-E-P-) as other shades. The reason for this was thought to be enzyme-substrate compatibility [62]. There was also the possibility that laccase enzyme would provide higher color removal by using it in the presence of mediator [59]. In general, the use of enzymes with hydrogen peroxide adversely affected the activity of enzymes [60,61]. Although lower transmittance values were obtained with C/NBs-H_2O_2-E-P- in red and black compared to C/NBs-E-P-, the highest transmittance for blue was obtained from NBs-H_2O_2-E-P 4 g/L. It was also observed that 60 minutes was the optimum process time for decolorization with NBs.

Overall, except for navy blue and red, approximately 60% - 70% color removal was achieved in C/NBs-E-P- processes at the highest enzyme concentration (4g/L).

3.1 Chemical Oxygen Demand (COD)

COD values of some baths are given in Figure 9. In the COD measurement after decolorization, fuchsia was chosen for the light and black for the dark shade dyeings. In this figure, the COD values of the samples treated with NBs for 60 minutes were examined.
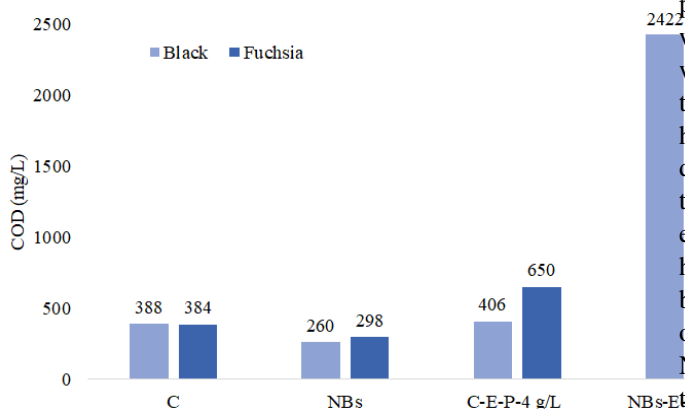

Figure 9. COD values of some decolorization baths

It was determined that the COD values of the wastewater samples (C) obtained after fuchsia and black dyeing were close to each other before they were subjected to the decolorization process. The COD value of the black "C" decreased from 388 mg/L to 260 mg/L after NBs decolorization processes, and that of fuchsia C from 384 mg/L to 298 mg/L. It is known that NBs provide degrading

of organic compounds [64] by producing hydroxyl free radical (•OH) in water [15]. Comparison of dark (5.9 %) and light (50.52 %) shade decolorized with NBs showed that lower COD values were obtained from the dark shade. This could have been explained by the color removal of the dark shade dyeing, that is, the degrading molecules, was lower than the light shade dyeing. The increase in the COD values of the processes in which enzymes were used in decolorization compared to C and NBs was thought to be due to higher decolorization rate. Higher COD values were obtained in the NBs-E-P 4 g/L process compared to that of the C-E-P 4 g/L. Although these decolorization processes had similar decolorization rates, COD values were much higher in the processes using NBs. This could have been interpreted as enzymes whose activities increased with the use of NBs [63] could also cause degradation of numerous chemical structures. It was determined that the lowest COD value was obtained from the black NBs-60' decolorization process.

4. CONCLUSION

In the midst of the worldwide environmental movement towards a more sustainable and greener future, textile, as a completely integrated industry, is one of the focal points with a global market size of 1000.3 billion USD in 2020. Looking at the environmental impacts of the textile industry of this size reveals that wastewater is a major environmental barrier to the growth of the textile industry alongside other minor issues such as solid waste. Textile wet processing requires large quantities of fresh water such that about 50 L to 100 L of water is needed to make 1 kg of textiles. Annual textile production consumes about 93 billion cubic meters of water per year, which is equivalent to total water amount in 37 million olympic swimming pools. Considering the wastewater generated in each textile wet process is highly polluted, it is obvious that textile wastewater poses a great threat to the environment. When textile wastewater is not treated properly, it endangers both human health and the environment. In this article, the decolorization of textile dyeing wastewater with NBs technology, as a new water technology, and environmentally friendly enzymes (laccase and peroxidase) has been investigated. We found that the decolorization behavior of different dyes could be improved with the use of NBs technology as well as enzymes. The effectiveness of NBs in decolorization could have been increased by making their charge positive [21]. Processes using enzymes with NBs were very effective in color removal. These effects could have even been improved with the use of mediators [59]. As enzymes were used in increasing concentrations, their effectiveness in decolorization also increased. Hydrogen peroxide used together with peroxidase did not increase the color removal efficiency; on the contrary, it decreased the effect of the enzyme. It was interpreted as the hydrogen peroxide could have effected negatively peroxidase activity as stated in the literature [60,61]. While

NBs used alone in decolorization caused a decrease in COD values compared to those of the untreated samples, when used with enzymes, COD values increased. This could have been interpreted as a synergistic effect between enzymes and NBs. The use of NBs could have increased the activities of the enzymes [63], caused more molecules to be degraded and thus increased the COD.

In the literature, researchers have proposed various mechanisms related to the role of reactive species and hydroxyl radicals released in solutions on oxidizing dyes, supercritical reactions at the interface of the bubbles, and the degradation of dyes within the bubbles [25,65]. In other words, there are still many issues to be investigated regarding NBs. In the future, it is planned to develop this study in detail on the subjects mentioned below:

There is information in the literature that the highest color removal is achieved with the combined use of NBs with hydrogen peroxide [21]. In the next study, the combination of NBs-hydrogen peroxide will also be examined.

-Since it is known that electrostatic interaction between NBs, whose zeta potential can be controlled (negative or positive), and dye components is effective on decolorization [66,67], it is planned to examine the effects of adding various surfactants or salts to solutions in future studies.

-It is known that the effect of NBs on decolorization is reduced as a result of rapid bursting due to excessive heat [64]. Since NBs was used with enzymes in this study, decolorization process temperatures were chosen according to the optimum operating temperatures of the enzymes. It was revealed that temperature optimization of decolorization process should also be done in future studies.

- Considering that laccase and peroxidase enzymes generally degrade azo dyes [68], it would be beneficial to select dyes by controlling their structures in future studies.

Acknowledgement

REFERENCES

1. Haris S, Qiu X, Klammler H, Mohamed MMA. 2020. The Use of Micro-Nano Bubbles in Groundwater Remediation: A Comprehensive Review. *Groundwater for Sustainable Development*, 11, 100463.

2. Zhou L, Wang S, Zhang L, Hu J. 2021. Generation and Stability of Bulk Nanobubbles: A Review and Perspective. *Current Opinion in Colloid & Interface Science,* 53, 101439.

3. Yasui K, Tuziuti T, Kanematsu W, Kato K. 2016. Dynamic Equilibrium Model for a Bulk Nanobubble and a Microbubble Partly Covered with Hydrophobic Material. *Langmuir,* 32(43), 11101–11110.

4. Weijs JH, Seddon JRT, Lohse D. 2012. Diffusive Shielding Stabilizes Bulk Nanobubble Clusters. *ChemPhysChem,* 13(8), 2197–2204.

5. Yasui K, Tuziuti T, Kanematsu W. 2018. Mysteries of Bulk Nanobubbles (Ultrafine Bubbles); Stability and Radical Formation. *Ultrasonics Sonochemistry,* 48, 259–266.

6. Meegoda JN, Hewage SA, Batagoda JH. 2019. Application of the Diffused Double Layer Theory to Nanobubbles. *Langmuir,* 35 (37), 12100–12112.

7. Epstein PS, Plesset MS. 1950. On the Stability of Gas Bubbles in Liquid-gas Solutions. *J Chem Phys* 18, 1505–1509.

8. Parker JL, Claesson PM, Attard P. 1994. Bubbles, Cavities, and The Long-ranged Attraction between Hydrophobic Surfaces. *The Journal of Physical Chemistry*, 98, 8468–8480.

9. Lou S-T, Ouyang Z-Q, Zhang Y, Li X-J, Hu J, Li M-Q, Yang F-J. 2000. Nanobubbles on Solid Surface Imaged by Atomic Force Microscopy. *Journal of Vacuum Science & Technology B: Microelectronics and Nanometer Structures Processing, Measurement, and Phenomena,* 18, 2573–2575.

10. Ishida N, Inoue T, Miyahara M, Higashitani K. 2000. Nano bubbles on a Hydrophobic Surface in Water Observed by Tapping-Mode Atomic Force Microscopy. *Langmuir,* 16, 6377–6380.

11. Borkent BM, Dammer SM, Schönherr H, Vancso GJ, Lohse D. 2007. Superstability of Surface Nanobubbles. *Physical Review Letters,* 98, 204502.

12. Alheshibri M, Qian J, Jehannin M, Craig VSJ. 2016. A History of Nanobubbles. *Langmuir,* 32, 11086–11100.

13. Lohse D, Zhang X. 2015. Surface Nanobubbles and Nanodroplets. *Reviews of Modern Physics,* 87, 981–1035.

14. Qian J, Craig VSJ, Jehannin M. 2019. Long-Term Stability of Surface Nanobubbles in Undersaturated Aqueous Solution. *Langmuir,* 35(3), 718–728.

15. Takahashi M, Chiba K, Li P. 2007. Free-radical Generation from Collapsing Microbubbles in the Absence of A Dynamic Stimulus. *The Journal of Physical Chemistry B,* 111 (6), 1343–1347.

16. Ma P, Han C, He Q, Miao Z, Gao M, Wan K, Xu E. 2022. Oxidation of Congo Red by Fenton Coupled with Micro and Nanobubbles. *Environmental Technology,* 44(17), 2539-2548.

17. Azevedo A, Oliveira H, Rubio J. 2019. Bulk Nanobubbles in the Mineral and Environmental Areas: Updating Research and Applications. *Advances in Colloid and Interface Science,* 271, 101992.

18. Minamikawa K, Makino T. 2020. Oxidation of Flooded Paddy Soil through Irrigation with Water Containing Bulk Oxygen Nanobubbles. *Science of The Total Environment,* 709, 136323.

19. Zhou Y, Li Y, Liu X, Wang K, Muhammad T. 2019. Synergistic Improvement in Spring Maize Yield and Quality with Micro/Nanobubbles Water Oxygation. *Scientific*

Reports, 9(1), 5226.

20. Endo-Takahashi Y, Negishi Y. 2020. Microbubbles and Nanobubbles with Ultrasound for Systemic Gene Delivery. *Pharmaceutics,* 12 (964), 1–14.

21. Bui TT, Han M. 2020. Decolorization of Dark Green Rit Dye Using Positively Charged Nanobubbles Technologies. *Separation and Purification Technology,* 233, 116034.

22. Anis P, Toprak-Cavdur T, Çalışkan N. 2022. Oxygen-enriched Nanobubbles for a Green Reactive Washing Process. *AATCC Journal of Research,* 9 (3), 152–160.

23. Wu J, Zhang K, Cen C, Wu X, Mao R, Zheng Y. 2021. Role of Bulk Nanobubbles in Removing Organic Pollutants in Wastewater Treatment. *AMB Express,* 11 (96), 1–13.

24. Rojviroon O, Rojviroon T. 2022. Photocatalytic Process Augmented with Micro/Nano Bubble Aeration for Enhanced Degradation of Synthetic Dyes in Wastewater. *Water Resources and Industry,* 27, 100169.

25. Sakr M, Mohamed MM, Maraqa MA, Hamouda MA, Aly Hassan A, Ali J, Jung J. 2022. A Critical Review of the Recent Developments in Micro–nano Bubbles Applications for Domestic and Industrial Wastewater Treatment. *Alexandria Engineering Journal,* 61 (8), 6591–6612.

26. Liu C, Tang Y. 2019. November. Application Research of Micro and Nano Bubbles in Water Pollution Control. In T.Y. Fang, V. Khaletski (Ed.), Proceedings of the 2019 International Conference on Building Energy Conservation, Thermal Safety and Environmental Pollution Control (ICBTE 2019) (1-3), Hefei, China

27. Mohsin M, Rasheed A, Farooq A, Ashraf M, Shah A. 2013. Environment Friendly Finishing of Sulphur, Vat, Direct and Reactive Dyed Cotton Fabric. *Journal of Cleaner Production,* 53, 341–347.

28. Mohsin M, Sardar S, Hassan M, Akhtar N, Hassan A, Sufyan M. 2020. Novel, Sustainable and Water Efficient Nano Bubble Dyeing of Cotton Fabric. *Cellulose,* 27 (10), 6055–6064.

29. Mohsin M, Sardar S, Hasan M, Akhtar KS, Anam W, Ijaz S, Hassan A. 2022. Water Efficient, Eco-friendly and Effluent Free Nano bubble Finishing of Cotton Fabric. *Journal of Natural Fibers,* 19(6), 12586-12595.

30. Slama H Ben, Bouket AC, Pourhassan Z, Alenezi FN, Silini A, Cherif-Silini H, Oszako T, Luptakova L, Golinska P, Belbahri L. 2021. Diversity of Synthetic Dyes from Textile Industries, Discharge Impacts and Treatment Methods. *Applied Sciences,* 11(14), 6255.

31. Bhatia D, Sharma NR, Singh J, Kanwar RS. 2017. Biological Methods for Textile Dye Removal from Wastewater: A Review. *Critical Reviews in Environmental Science and Technology,* 47 (19), 1836–1876.

32. Jamee R, Siddique R. 2019. Biodegradation of Synthetic Dyes of Textile Effluent by Microorganisms: An Environmentally and Economically Sustainable Approach. *European Journal of Microbiology and Immunology,* 9 (4), 114–118.

33. Thakur S, Chauhan MS. 2018. Treatment of Dye Wastewater from Textile Industry by Electrocoagulation and Fenton Oxidation: A Review. In V. Singh, S. Yadav, R. Yadava (Ed.), Water Qual. Manag. Singapore:Springer, 117–129.

34. Gopalakrishnan M, Punitha V, Saravanan D. 2019. Water Conservation in Textile Wet Processing. In S.S. Muthu (Ed.), Water Text. Fash. Consum. Footprint, Life Cycle Assess. Cambridge: Woodhead Publishing, 35–53.

35. Dong X, Gu Z, Hang C, Ke G, Jiang L, He J. 2019. Study on the Salt-free low-Alkaline Reactive Cotton Dyeing in High Concentration of Ethanol in Volume. *Journal of Cleaner Production,* 226, 316–323.

36. Ma W, Meng M, Yan S, Zhang S. 2016. Salt-free Reactive Dyeing of Betaine-modified Cationic Cotton Fabrics with Enhanced Dye Fixation. *Chinese Journal of Chemical Engineering,* 24 (1), 175–179.

37. Siddiqua UH, Ali S, Iqbal M, Hussain T. 2017. Relationship Between Structure and Dyeing Properties of Reactive Dyes for Cotton Dyeing. *Journal of Molecular Liquids,* 241, 839–844.

38. Grancarić AM, Ristić N, Tarbuk A, Ristić I. 2013. Electrokinetic Phenomena of Cationised Cotton and Its Dyeability with Reactive Dyes. *Fibres & Textiles in Eastern Europe,* 21 (6), 106–110.

39. Varadarajan G, Venkatachalam P. 2016. Sustainable Textile Dyeing Processes. *Environmental Chemistry Letters,* 14 (1), 113–122.

40. Arivithamani N, Giri Dev VR. 2018. Characterization and Comparison of Salt-free Reactive Dyed Cationized Cotton Hosiery Fabrics with that of Conventional Dyed Cotton Fabrics. *Journal of Cleaner Production,* 183, 579–589.

41. Khatri A, Peerzada MH, Mohsin M, White M. 2015. A Review on Developments in Dyeing Cotton Fabrics with Reactive Dyes for Reducing Effluent Pollution. *Journal of Cleaner Production,* 87 (1), 50–57.

42. Khattab TA, Abdelrahman MS, Rehan M. 2020. Textile Dyeing Industry: Environmental Impacts and Remediation. *Environmental Science and Pollution Research,* 27 (4), 3803–3818.

43. Klančnik M. 2000. The Influence of Temperature on the Kinetics of Concurrent Hydrolysis and Methanolysis Reactions of a Monochlorotriazine Reactive Dye. *Dyes and Pigment* 46 (1), 9–15.

44. Amin MN, Blackburn RS. 2015. Sustainable Chemistry Method to Improve the Wash-off Process of Reactive Dyes on Cotton. *ACS Sustainable Chemistry & Engineering,* 3 (4), 725–732.

45. Chattopadhyay DP. 2011. Chemistry of Dyeing. In M. Clark (Ed.), Handb. Text. Ind. Dye. Vol. 1 Princ. Process. Types Dye. Cambridge: Woodhead Publishing, 150–183.

46. Zhang Y, Shahid-ul-Islam, Rather LJ, Li Q. 2022. Recent Advances in the Surface Modification Strategies to Improve Functional Finishing of Cotton with Natural Colourants - A review. *Journal of Cleaner Production,* 335, 130313.

47. Khatri A, Padhye R, White M. 2013. The Use of Trisodium Nitrilo Triacetate in the Pad-steam Dyeing of Cotton with Reactive Dyes. *Coloration Technology,* 129 (1), 76–81.

48. Ramasamy M, Kandasaamy P V. 2005. Effect of Cationization of Cotton on It's Dyeability. *Indian J Fibre Text Res* 30 (3), 315–323.

49. Burkinshaw SM, Mignanelli M, Froehling PE, Bide MJ. 2000. The Use of Dendrimers to Modify the Dyeing

Behaviour of Reactive Dyes on Cotton. *Dyes and Pigments* 47, 259–267.

50. Khatri A, White M. 2016. Sustainable Dyeing Technologies. In R. Blackburn R (Ed.), Sustain. Appar. Prod. Process. Recycl. Cambridge: Woodhead Publishing, 135–160.

51. Holkar CR, Jadhav AJ, Pinjari D V., Mahamuni NM, Pandit AB. 2016. A Critical Review on Textile Wastewater Treatments: Possible Approaches. *Journal of Environmental Management,* 182, 351–366.

52. Benkhaya S, M'rabet S, Lgaz H, El-Bachiri A, El-Harf A. 2022. Dyes: Classification, Pollution, and Environmental Effects. In S.S. Muthu, A. Khadir (Ed), Dye Biodegrad. Mech. Tech. Recent Adv. Singapore: Springer, 1–50.

53. Madhav S, Ahamad A, Singh P, Mishra PK. 2018. A Review of Textile Industry: Wet Processing, Environmental Impacts, and Effluent Treatment Methods. *Environmental Quality Management*, 27 (3), 31–41.

54. Labiadh L, Barbucci A, Carpanese MP, Gadri A, Ammar S, Panizza M. 2017. Direct and Indirect Electrochemical Oxidation of Indigo Carmine using PbO2 and TiRuSnO2. *Journal of Solid State Electrochemistry,* 21 (8), 2167–2175.

55. Gita S, Hussan A, Choudhury TG. 2017. Impact of Textile Dyes Waste on Aquatic Environments and its Treatment. *Environment & Ecology,* 35 (3C), 2349–2353.

56. Eslami H, Shariatifa A, Rafiee E, Shiranian M, Salehi F, Hosseini SS, Eslami G, Ghanbari R, Ebrahimi A A. 2019. Decolorization and Biodegradation of Reactive Red 198 Azo Dye by A New Enterococcus faecalis–Klebsiella variicola Bacterial Consortium Isolated From Textile Wastewater Sludge. *World Journal of Microbiology and Biotechnology,* 35 (3), 1–10.

57. Singh P, Jain R, Srivastava N, Borthakur A, Pal DB, Singh R, Madhav S, Srivastava P, Tiwary D, Mishra P K. 2017. Current and Emerging Trends in Bioremediation of Petrochemical Waste: A Review. *Critical Reviews in Environmental Science and Technology,* 47 (3), 155–201.

58. Toprak T, Anis P. 2018. Enzymatic Decolorization of Reactive Dyeing Baths. *Journal of Textile Engineering & Fashion Technology,* 4 (4), 308–311.

59. Champagne PP, Ramsay JA. 2005. Contribution of Manganese Peroxidase and Laccase to Dye Decoloration by Trametes versicolor. *Applied Microbiology and Biotechnology,* 69, 276–285.

60. Arnao MB, Acosta M, del Rio JA, García-Cánovas F. 1990. Inactivation of Peroxidase by Hydrogen Peroxide and Its Protection by A Reductant Agent. *Biochimica et Biophysica Acta (BBA) - Protein Structure and Molecular Enzymology,* 1038 (1), 85–89.

61. Nicell JA, Wright H. 1997. A Model of Peroxidase Activity with Inhibition by Hydrogen Peroxide. *Enzyme and Microbial Technology,* 21 (4), 302–310.

62. Kokol V, Doliška A, Eichlerová I, Baldrian P, Nerud F. 2007. Decolorization of Textile Dyes by Whole Cultures of Ischnoderma resinosum and by Purified Laccase and Mn-Peroxidase. *Enzyme and Microbial Technology,* 40 (7), 1673–1677.

63. Patel AK, Singhania RR, Chen CW, Tseng YS, Kuo CH, Wu CH, Dong C D. 2021. Advances in Micro- and Nano Bubbles Technology for Application in Biochemical Processes. *Environmental Technology & Innovation,* 23, 101729.

64. Selihin NM, Tay MG. 2022. A review on Future Wastewater Treatment Technologies: Micro-Nanobubbles, Hybrid Electro-Fenton Processes, Photocatalytic Fuel Cells, and Microbial Fuel Cells. *Water Science and Technology,* 85 (1), 319–341.

65. Han G, Chen S, Su S, Huang Y, Liu B, Sun H. 2022. A Review and Perspective on Micro and Nanobubbles: What They Are and Why They Matter. *Minerals Engineering,* 189, 107906.

66. Temesgen T, Bui TT, Han M, Kim T il, Park H. 2017. Micro and Nanobubble Technologies as A New Horizon for Water-treatment Techniques: A Review. *Advances in Colloid and Interface Science* 246, 40–51.

67. Bui TT, Nguyen DC, Han M. 2019. Average Size and Zeta Potential of Nanobubbles in Different Reagent Solutions. *Journal of Nanoparticle Research,* 21, 1–11.

68. Imran M, Crowley DE, Khalid A, Hussain S, Mumtaz MW, Arshad M. 2015. Microbial Biotechnology for Decolorization of Textile Wastewaters. *Reviews in Environmental Science and Bio/Technology,* 14 (1), 73–92.

Investigation of the Release of Growth Factors from Apheresis Platelet Concentrate (APC) Loaded Three Layered Composite Nanofiber Surface

Hülya Yılmaz[1,2] 0000-0003-4729-1987
Cansu Aras[3] 0000-0003-0773-4560
Mehmet Karaçay[4] 0000-0002-5301-6626
Merve İlkay Altuntuğ Cesur[5] 0000-0003-2239-3493
Esra Karaca[3] 0000-0003-1777-3977
Şehime Gülsün Temel[2,6,7] 0000-0002-9802-0880
Emel Bülbül Başkan[8] 0000-0002-0144-3263
Haluk Barbaros Oral[5] 0000-0003-0463-6818
Ekrem Kaya[9] 0000-0002-9562-4195

[1]Bursa Uludag University/Department of Fundamentals of Nursing, Faculty of Health Sciences/Gorukle, 16059 Bursa, Turkiye
[2]Bursa Uludag University/Department of Translational Medicine, Institute of Health Sciences/Gorukle, 16059 Bursa, Turkiye
[3]Bursa Uludag University/Department Textile of Engineering, Faculty of Engineering/Gorukle, 16059 Bursa, Turkiye
[4]Bursa Uludag University/Department of Immunology, Faculty of Medicine/Gorukle, 16059 Bursa, Turkiye
[5]Bursa Uludag University/Department of Biomaterials, Graduate School of Natural and Applied Science/Gorukle, 16059 Bursa, Turkiye
[6]Bursa Uludag University/Department of Medical Genetics, Faculty of Medicine/Gorukle, 16059 Bursa, Turkiye
[7]Bursa Uludag University/Department of Histology & Embryology, Faculty of Medicine/Gorukle, 16059 Bursa, Turkiye
[8]Bursa Uludag University/Department of Dermatology, Faculty of Medicine/Gorukle, 16059 Bursa, Turkiye
[9]Bursa Uludag University/Department of General Surgery, Faculty of Medicine/Gorukle, 16059 Bursa, Turkiye

Corresponding Author: Hülya Yılmaz, hlyyilmaz@uludag.edu.tr

ABSTRACT

In this study, a nanofiber surface loaded with apheresis platelet concentrate (APC) was produced for the first time to develop a bioactive wound dressing design. Nanofiber surface (n=5) consisting of polyurethane polymer outer layer, polyvinyl alcohol polymer middle layer, and polycaprolactone polymer matrix inner layer were produced via the electrospinning method. The surface morphologies of the produced nanofiber surfaces were examined by scanning electron microscopy. Quantitative analyzes of growth factors released from the APC-loaded composite nanofiber surfaces into phosphate-buffered saline at certain time intervals were performed with the ELISA. When the release amounts between bFGF, EGF, and PDGF-AA groups were compared, a significant difference was found in all periods (p<0.05). When the time-dependent release changes of each group were examined, there was no statistically significant difference in the bFGF group (p>0.05), but there was a significant difference between the EGF and PDGF-AA growth factors (p<0.05).

1. INTRODUCTION

Acute and chronic wound and wound care generally is costly due to its complex etiology, prolonged disease duration, very high treatment costs, depletion of medical resources, and reduced quality of life which is a significant burden for society [1,2]. To provide a moist environment to support the healing process in the clinic, wound dressings such as films, sponges, hydrogels, hydrocolloids, and alginates are widely used as the main treatment strategies in wound care [3,4]. Modern wound care approaches and innovations in tissue engineering have accelerated the development of bioactive dressings such as cellular and/or tissue-based products. Bioactive dressings can be diversified stem cell-based therapeutics, placental

To cite this article: Yılmaz H, Aras C, Karaçay M, Altuntuğ Cesur M İ, Karaca E, Temel Ş G, Bülbül Başkan E, Oral H B, Kaya E. 2024. Investigation of the release of growth factors from apheresis platelet concentrate (APC) loaded three layered composite nanofiber surface. *Tekstil ve Konfeksiyon* 34(3), 244-252.

dressings; bio printed dressings, and acellular dermal substitutes. Bioactive or interactive dressings categorized by the Food and Drug Administration (FDA) may contain various biological agents such as growth factors necessary for rapid healing and prevention of scar formation by keeping the wound area moist [5-7]. These biological agents can be derived from xenogeneic, allogeneic, and autologous sources. Although platelets obtained from allogeneic or autologous sources are relatively small molecules compared to other red blood cells, they contain secretory vesicles that can secrete various factors called granules, and many proteins, cytokines, and growth factors that initiate wound healing and regulate basic reactions [8,9]. In the cellular phase of wound healing, polypeptide growth factors secreted from α-granules accumulate in the wound area to activate chemotaxis, differentiation, mitogenesis, and secretory proteins of cells and initiate healing [10]. Membrane-bound α-granules in the structure of the platelets make intracellular storage and release platelet-derived growth factors (PDGF), transforming growth factors (TGF-β), epidermal growth factor (EGF), and vascular endothelial growth factor (VEGF), which are vital for wound healing, and insulin-like growth factors (IGF-I) [8,11,12]. Growth factors are critically important biomolecules that provide the necessary interaction for tissue repair at the cellular stage of wound healing, improving cellular behavior and tissue regeneration. However, in clinical practice, the degradation of growth factors by hydrolytic enzymes in the wound content causes application limitations [13-15].

It is obtained by separating only platelets from a single donor using apheresis devices and special sets in the APC blood bank containing growth factors. Cells are separated from the donor in an anticoagulant solution and separated by centrifugation according to density and other filtration parameters, and other blood products are returned to circulation after the selected product is separated [16]. Under normal conditions, there are 150,000/ μl – 350,000/ μl platelets in the peripheral blood. 3×10^{11} or more platelets are collected from a donor by apheresis. Typically, one unit of APC is derived from whole blood, providing $3-6 \times 10^{11}$ platelets equivalent to 6 or more units [17]. This means a large number of growth factors. The platelet-rich part obtained by centrifuging the peripheral blood in anticoagulant tubes at a certain speed and time is called Platelet Rich Plasma (PRP). PRP is an autologous clinical treatment proven to accelerate wound healing. It is used in various clinical applications such as orthodontics, osteogenic care, orthopedics, acute and chronic wounds, and cosmetics [18-20]. In the literature, there are studies on PRP-loaded nanofiber surface models. Farzamfar et al. developed Polylactic Acid (PLA)/Gelatin (GT) nanofibrous surfaces containing PRP for peripheral nerve regeneration. As a result, cell attachment, in vitro viability, and porosity were found to be better when PRP was included on gelatin nanofiber surfaces compared to pure PLA surfaces [21]. In another study, the authors used PCL nanofibrous scaffolds

for wound healing. In this study, the researchers explained that the covalently bound components of PRP significantly reduced fibroblast apoptosis and increased cell proliferation compared to unmodified PCL nanofibers or PRP to non-covalent polycaprolactone (PCL) nanofibers [22]. Zhang et al. developed a sodium alginate-based PRP-loaded double-layer hydrogel dressing. In vivo, evaluations showed that the gel promoted wound healing in terms of rapid re-epithelialization, increased growth factor levels, wound healing, and early transitions in angiogenesis [20].

Recent advances in nanotechnology have enabled the production of nanofibrous structures with architectural features and morphological similarities similar to the natural extracellular matrix (ECM) in the human body. Electrospinning is a simple, versatile, cost-effective system for obtaining smooth and very fine nanofiber surfaces from synthetic or natural polymers using electrical field strengths [23]. Wound dressings obtained from electrospinning nanofibers have many advantages over conventional dressings [13-15]. Electrospun nanofiber dressings provide an ideal structure to replace the ECM until the host cells grow and new tissue is formed. Thanks to the large surface area and microporous structure of electrospinning nanofibrous surfaces, they can help stimulate fibroblasts, which can secrete important extracellular matrix components such as collagen and various cytokines (e.g. growth factors and angiogenic factors) to repair tissue damage after injury. In addition, it is possible to add antibacterial and therapeutic substances to nanofiber surfaces. Recently, many studies have been reported on electrospun surfaces obtained from mixtures of natural biopolymers and synthetic polymers. In particular, polyurethane (PU) nanofiber surfaces produced by electrospinning are widely used for wound dressing applications. PU nanofiber surfaces are preferred to be used as wound dressings due to their good barrier properties and oxygen permeability. In addition, it has been reported that PU-based semi-permeable dressings accelerate wound healing. However, PU polymer is a very soft and hydrophobic polymer. It can be a disadvantage in terms of these two properties when used alone as a wound dressing material. Because it may be too mild for clinical use as a wound dressing; besides, its hydrophobic property can prevent the absorption of fluid from the wound surface [23]. In addition to being a water-soluble polymer, Poly(vinyl alcohol) (PVA) is a non-toxic, biocompatible, and biodegradable polymer. PVA polymer is generally used by blending with other polymers to increase mechanical performance [24]. However, due to its high-water solubility, it is not suitable for clinical use as a stand-alone biomedical material in medical applications exposed to liquids such as wound fluid or blood. PCL, an FDA-approved, biocompatible, and biodegradable polymer, was found to be suitable for tissue regeneration, with its nanofibers appearing to effectively heal full-thickness skin wounds in rats [25].

In this study, three-layer composite nanofiber surface fabrication for use in wound care treatment was carried out using the electrospinning method. The layer, which forms the outer and first layer of the composite dressing that comes into contact with the environment, was obtained with a flexible and hydrophobic PU-based nanofiber surface. Then, this surface was covered with an APC-added PVA nanofiber surface. Finally, on the layer that will contact the wound area; to control the release of the APC bioactive agent and to increase the resistance against wound fluid, a composite nanofiber surface was produced by coating the PCL nanofiber surface. By using scanning electron microscopy (SEM) to determine the morphological properties of the produced composite nanofiber surface; the nanofiber diameter was determined. The Sandwich ELISA method was used to determine the release of APC bioactive agent from the produced composite surface.

2. MATERIAL AND METHOD

2.1 Material

As an additive, APC from the volunteer researcher was apheresis at a university blood center. Colter counter (Beckman, USA; 100 μm slit), 6% dimethyl sulfoxide (DMSO), and –80°C refrigerant were used for APC. Polyvinyl alcohol (PVA; 87–89% hydrolyzed and molecular weight of 85,000–124,000 g/mol), polycaprolactone (PCL molecular weight of 80 000), Dimethyl formamide (DMF), Dichloromethane (DCM) used on nanofiber surfaces from Sigma Aldrich; thermoplastic polyurethane (TPU) was obtained from BASF. Elga Flex3 water purification system (Veloia Water Solutions & Technologies, France) was used to prepare purified water. Thermo Scientific Pierce BCA (bichinconic acid) Protein Assay Kit (Thermo, USA) was used for BCA measurement. ELISA Kit Human EGF (Epidermal Growth Factor), bFGF (basic Fibroblast Growth Factor), and PDGF AA (Platelet Derived Growth Factor) (Elabscience, USA) were used for growth factors release.

2.2 Method

2.2.1. APC acquisition

APC used as an additive was obtained from a healthy and voluntary 31-year-old male, 178cm, 84 kg, Hg:16mg/dl, of West Asian descent, by obtaining informed consent. Platelet count 204000/μL was determined using a Coulter counter (Beckman, USA; 100 μm slit). Each apheresis platelet concentrate (APC) was divided into equal volumes and stored frozen at –80°C using 6% dimethyl sulfoxide (DMSO). After thawing APCs in a water bath at 37°C and removal from DMSO by centrifugation, they were diluted using autologous plasma or 0.9% NaCl.

2.2.2. Production of APC-loaded composite nanofiber surfaces

A three-layered composite nanofiber surface production approach was adopted to obtain a wound dressing that would release APC in a controlled manner. The first layer, which forms the outer layer of the dressing, was obtained from flexible, biocompatible, inert, and non-biodegradable PU nanofibers. The nanofibrous surface, which forms the second and middle layer of the composite structure, was formed from APC bioactive agent-loaded water-soluble PVA nanofibers. In the third layer, which will contact the wound environment, biocompatible and biodegradable PCL nanofibers were preferred.

PU polymer (10%, w/v) was stirred in DMF at 80ºC for 12 hours to dissolve. Aqueous PVA solution (10%, w/v) was prepared at 90ºC for 8 hours. Then, APC was added to the solution at a ratio of 9:1 (v/v) to obtain a PVA/APC mixture solution. The amount of APC added to the nanofibers is equal volume and 1 mL for each sample. The DMF: DCM (8:2, v/v) solvent system was used to dissolve to PCL polymer. PCL solution (10%, w/v) was stirred in the solvent system at 40ºC for 4 hours. Viscosity values of the prepared solutions were measured in Brookfield RV-DV II Viscometer at 100 rpm.

In the production of nanofiber surfaces, an INOVENSO Starter Kit electrospinning device was used. Firstly, the outer layer consisting of PU nanofiber was produced. Then the PVA nanofiber middle layer surface was then created on the PU nanofiber surface. Finally, the middle layer of the PVA surface was used to gather the inner layer, which is composed of PCL nanofiber. The flat plate received the deposition of the nanofibers. The nanofibers were deposited on the flat plate. Production was carried out under room conditions. The production parameters of nanofiber surfaces are given in Table 1.

Table 1. Production parameters of nanofiber surfaces

Nanofiber surface	Feed rate (ml/h)	Distance between needle tip collector (cm)	Applied voltage (kV)
PU	1 mL	20	20
PVA/APC	0.5	15	20
PCL	0.7	20	18

The produced surfaces were stored at -80°C until the following test and analysis. Carl Zeiss AG-EVO 40 XVP SEM was used to observe both the surface morphology of each produced nanofiber surface and the cross-sectional image of the three-layer composite structure. Nanofiber diameters were measured from the SEM images of each layer by using ImageJ image-processing program. In addition, the thickness of the composite structure was determined from three different regions with a digital micrometer.

The contact angle value provides information about surface properties such as hydrophobic, wettability, adhesion, and absorption [26]. Contact angle measurement of nanofiber surfaces was carried out using the "sessile drop technique" in KSV-The Modular CAM 200 Contact Angle

Measurement System. 40 photographs were taken from three different regions of the surfaces.

2.2.3. Determination of protein concentrations with BCA

Phases for EGF (catalog no: E-EL-H0059), bFGF (catalog no: E-EL-H6042), PDGF-AA (catalog no: E-EL-H1575) growth factors release used to do the in vitro by ELISA (Elabscience, USA) were performed in a BSL2 cabinet (Telstar Bio II Advance, Spain). The produced APC-loaded nanofiber surfaces were incubated in phosphate-buffered saline (PBS) in an incubator containing 5% CO_2 at 37°C. 0.5 mL of PBS was collected at 0, 48, 96, 144, 192, 240, 288, and 336 hours and the same amount (0.5 mL) of fresh PBS was added instead of the PBS collected at the mentioned times. These intervals are determined for the analysis of growth factors to be released into PBS from APC-loaded nanofiber surfaces. The release time of the GF amount was monitored for 336 hours, considering that proteins may be degraded [20]. Release has continued until now, albeit in very low amounts. Since there was no follow-up after 336 hours, the aftermath is unknown. Fresh PBS was added as much as the collected amount of PBS. Collected PBS for quantitative analysis of growth factors and BCA protein concentration analysis stored at -20°C for analysis. BCA measurement was performed with Thermo Scientific Pierce BCA Protein Assay Kit (Thermo, USA) as recommended by the manufacturer.

2.2.4. Analysis of growth factors by ELISA (enzyme-linked immunosorbent assay) method

Quantitative analysis of growth factors released from APC-loaded composite nanofiber surface into PBS at certain time intervals, EGF, bFGF, PDGF-AA Technology Laboratory ELISA Kit (Elabscience, USA) was performed as recommended by the manufacturer [27]. Wells for diluted standard, blank, and samples were determined. Diluted versions of standard, blank, and samples were added to the appropriate wells with a final volume of 100 µL. All samples and standards were run as two wells. To accurately measure the optical density (OD) value, the microplate reader device was turned on 15 minutes ago and made ready. At the end of the incubation, 50 µl of stop solution was added to each well. The OD values of each well were determined with a microplate reader set to a wavelength of 450 nm. The same procedure was applied for the analysis of all growth factors.

3. RESULTS AND DISCUSSION

3.1. Results of APC-loaded composite nanofiber surfaces production, characterization, and morphology

The cross-sectional structure of the three-layered composite structure, whose outer, middle, and inner layers are PU, PVA/APC and PCL nanofiber surfaces, respectively, was observed using SEM (Figure 1). Three parallel layers of the composite nanofiber surface are distinguished from the SEM image.

In addition, the surface images of each nanofiber layer forming the three-layer composite structure were also examined using SEM (Figure 2). The measurement results of the surfaces are given in Table 1. The thickness of the three-layered nanofiber structure was determined as 0.17 ± 0.01 mm. The nanofibrous structure was suitable thickness for using as a wound-dressing [28, 29]. The SEM image of the PU-based layer showed that the nanofibers forming the surface had a smooth and bead-free structure (Figure 2a). The contact angle of the PU-based nanofiber surface was measured as high as 116◦. The high contact angle value shows that water droplets do not spread on the PU-based surface due to its hydrophobic character [30]. The outer layers of wound dressing used in wound care applications are expected to be water resistant and absorb liquid rapidly from the layer in contact with the wound area. The water contact angle of the outer layer of the wound dressing defines its ability to protect the wound from contaminated fluids. Its wettability characteristic indicates the time required for the liquid to pass through the inner contact layer of the wound. The water contact angle is an index that shows the waterproof property of materials. The high contact angle indicates that the material has good water repellency [31]. Due to the lack of cytotoxicity of PU-based materials, it is common to use them in the medical field as wound dressings. Since water-resistant surfaces with hydrophobic character with high liquid contact angles can be obtained by using PU electrospinning nanofiber membranes, it is appropriate to cover the outer layer of the composite structure to protect the wound area from contaminated liquids. For this purpose, PU electrospin nanofiber surfaces have quite a good potential for coating waterproof wound care products. The SEM image of the APC-loaded PVA-based layer shows that the morphology of the nanofibers is flattened surface (Figure 2b). Nanofiber morphology is directly affected by electrospinning parameters, solution properties as well as components. In the study by Zhang et al (2005), the morphology of electrospun PVA nanofibers blended with Bovine Serum Albumin (BSA), which is a kind of protein-based molecule, was investigated. It was determined that the surface morphology caused irregularity with the addition of a small amount of BSA. At the same time, it has been stated that PVA can form secondary bonds by interacting with protein-based BSA molecules [32]. The complex nature of BSA, blending with PVA made it difficult to draw fine nanofibers from the polymer jet. The interaction of PVA and BSA causes a decrease in the ability of the PVA solution to form jets. Due to the instability of the electrospinning process, it can lead to bead formation and a flattened appearance in the fiber morphology. It is thought that the main reason for the flattened appearance of the PVA nanofibers, on which the APC part of the blood containing protein-based components is loaded, is due to a similar molecular interaction. In addition, the contact angle value was measured to characterize the contact of the APC-loaded PVA nanofiber surface with the liquid. Accordingly, the contact angle value of the PVA/APC layer was 85°. In the literature, it has been reported that the contact angle value of PVA

nanofiber surfaces is 66° [33]. However, on surfaces where the PVA nanofiber surface morphology is flat or film-like, the closer position of the nanofibers to each other increases the physical connectivity of the nanofibers. Water molecules find it more challenging to enter the nanofiber as a result. This causes the contact angle value of the PVA nanofiber surface to reach a high value of 78.9° [34]. APC-loaded nanofiber surface produced within the scope of the study did not change the hydrophilic character of the PVA nanofiber surface. On the other hand, it is thought that the contact angle value is higher due to the closer and tighter position of the nanofibers forming the surface. The release of growth factors in APC from the hydrophilic PVA/APC nanofibers which are between the two hydrophobic layers, occurs as the degradation of the PVA nanofibers upon contact with the liquid. Besides, due to the hydrophilic nature of the growth factors [35], they are trapped in a hydrophobic biodegradable polymer which delays the entry and diffusion of water molecules [36]. In this way, it is tried to obtain a controlled release profile by keeping the growth factors in the polymer matrix. Growth factors linked to the nanofiber structure produce an appropriate initial release. A systematically controlled release then occurs due to the degradation of the polymeric matrix [37].
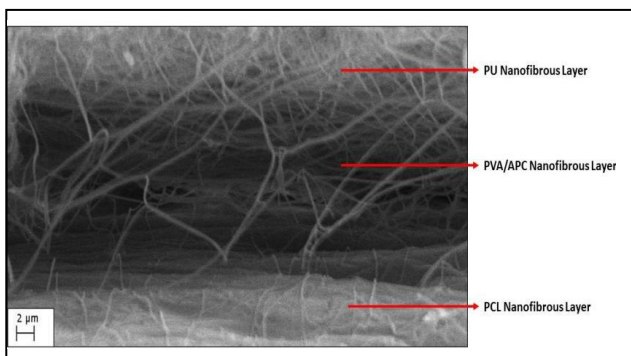

Figure 1. SEM images of cross-section of three layered PU-PVA/APC-PCL nanofibrous structure
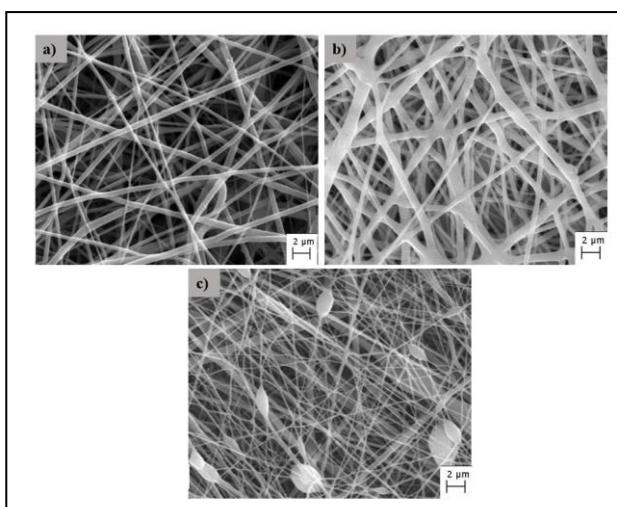

Figure 2. SEM images of nanofiber surfaces
a) PU nanofiber layer b) PVA/APC nanofiber layer c) PCL nanofiber layer

The scanning electron microscopy (SEM) image of the PCL-based layer reveals a surface with a thin and beaded nanofiber structure. This structure can be observed in Figure 2c of the image (Figure 2c). In addition, according to the measurement results of the 111° contact angle of the PCL nanofiber surface, it is understood that the surface has a hydrophobic character. Nanofibrous surfaces obtained by using bio-swelling or late-degrading polymers are excellent candidates for obtaining sustained drug-release systems with slow and controlled release. The preparation of nanofiber surfaces by sandwich production technique using the electrospinning method of different polymer solutions/melts sequentially, or the control of the bead diameter in the nanofiber structure are also applied to prolong drug release [38]. According to Laha et al. (2017), one layer of drug-loaded nanofibers was coated with another drug-free nanofiber layer with the sandwich fabrication technique approach to create a long-term drug release profile. In this way, the release with zero-order controlled drug release kinetics has been found to last up to 48 hours [39]. In addition, the beaded structures formed on the nanofiber surface also support long-term drug release [40]. In the study by Li et al., drug release control was achieved by adjusting the bead diameter on the nanofiber surface with various parameters. It is known that this hydrophobic character of PCL-based nanofibers is a feature that slows down the release rates of drugs or active components. In addition, the bead formation seen on the surface helps to slow down the release of active components loaded in the PCL nanofiber [41]. Thus, it is expected that the hydrophobic and beaded nanofiber structure of the PCL nanofiber surface, which is the inner layer of the produced composite nanofiber structure, provides a protective barrier and a reservoir to assist diffusion. In this way, it is thought that the diffusion of APC, which will occur after the contact of the nanofiber structure, which is thought to be applied as a wound dressing, to the wound exudate will be provided over a long period, and a controlled manner.

3.2. Results of the release of growth factors amounts by the time

The released amount of growth factors from the nanofiber surfaces to the buffer solution in vitro was first calculated using the EGF standard curve. The released amount of EGF component released from the nanofiber was determined from the acquired standard curve graph using the equation of the line that gives the absorbance value that varies with the amount of growth factor. Figure 3 shows reduction in EGF release over time. It was determined that the release in all samples reached the highest level in the first 48 hours. When the released amount of EGF from the first sample was examined, a decreasing release was observed towards the 48th and 96th hours. By the 144th hour, the released amount of increased again, and the release continued to decrease in the 288th and 336th hours zones. At the 96th hour, a decline was seen in the released amount of EGF when it was evaluated in the second sample. The released amount of EGF began to rise at the 144th hour, and it was found that it fell at the 192nd hour, rose at the 240th hour, fell again at the 288th hour, and rose once more at the 336th hour.

**Table 2.** Fiber diameters and fiber diameter distributions of nanofiber surfaces

Nanofiber surface	Contact angle	Fiber diameter (mean ± SD)	Fiber diameter distributions
PU	116°	933 ± 83 nm	700-900 nm
PVA/APC	85°	1433 ± 200 nm	1000-1600 nm
PCL	111°	229 ± 44 nm	160-310 nm
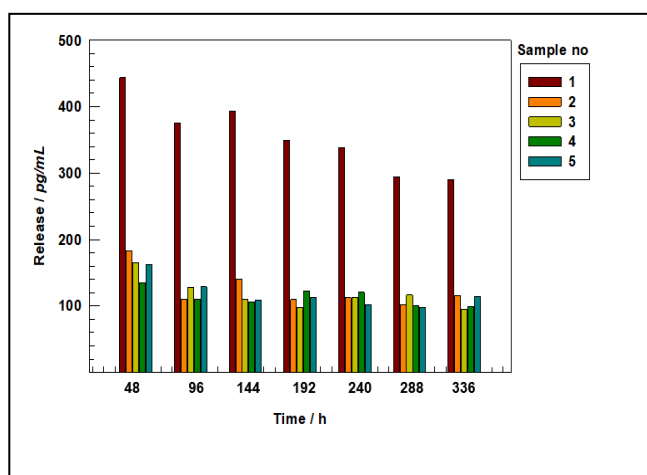
Figure 3. The release amount of EGF over time from nanofiber surfaces loaded with APC (n=5)

When the released amount of EGF from the third sample was examined, a decreasing release was observed towards 48th, 96th, 144th, 192nd hours. In addition, it was determined that the released of amount increased in the 240th and 288th hours and decreased in the 336th hour. When the released amount of EGF from the fourth sample was evaluated, a declining release was seen towards the 48th, 96th, and 144th hours. The released amount of EGF intensity peaked at the 192nd hour and then fell again at the 240th, 288th and 336th hours. When the fifth sample's released amount of EGF was examined, it was found to have decreased at 48th, 96th, and 144th hours. The released amount of EGF increased during the 192nd hour, reduced at the 240th and 288th hours, and then increased once again at the 336th hour, it was discovered.

The released amount of growth factors from the nanofiber surfaces to the buffer solution in vitro was first calculated using the bFGF standard curve. The released amount of bFGF component from the nanofiber was determined from the acquired standard curve graph using the equation of the line that gives the absorbance value that varies with the amount of growth factor. Figure 4 shows reduction in the released amount of bFGF over time. When the time-dependent released amount of bFGF from the first sample was evaluated, Figure 4 showed a decreasing release towards the 96th and 144th hours. The released amount of bFGF increased at the 192nd and 240th hours, reduced at the 288th and 336th hours, and then continued. The second sample's time-dependent the released amount of bFGF declined at 96th and 144th hours, increased again at 192nd hours, declined at 240 and 288th hours, then increased once

more at 336th hours. When the time-dependent released amount of bFGF from the third sample was evaluated, a rise was seen at the 96th hour and a decrease in the amount of release at the 144th and 192nd hours. The released amount of bFGF increased during the 240th and 288th hours. It started to fall on the 336th hour. When the time-dependent released amount of bFGF from the fourth sample was analyzed, a declining release was found towards the 96th and 144th hours. At the 192nd and 240th hours, the released amount level fell at the 288th and 336th hours. When the time-dependent released amount of bFGF from the fifth sample was analyzed, a decreasing release was observed towards the 48th and 96th hours. The released amount of value increased at the 192nd and 240th hours and decreased at the 288th hour. It was observed that it increased again at the 336th hour.
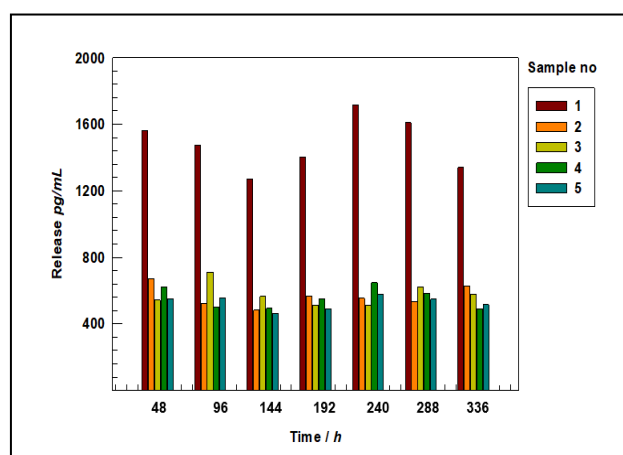
Figure 4. The release amount of bFGF release over time from nanofiber surfaces loaded with APC (n=5)

The number of growth factors released from the nanofiber surfaces to the buffer solution in vitro was first calculated using the PDGF-AA standard curve. The amount of PDGF-AA component released from the nanofiber was determined from the acquired standard curve graph using the equation of the line that gives the absorbance value that varies with the amount of growth factor. Figure 5 shows reduction in PDGF-AA release over time. When Figure 5 is studied, it can be seen that the release in all samples peaked within the first 48 hours. When the time-dependent released amount of PDGF-AA from the first sample was analyzed, 48th, 96th, 144th, and 192nd decreased throughout the hours. The released amount of PDGF-AA started to rise once more around the 240th hour, and it then started to fall once more in the 288th and 336th hour zones. When the time-dependent

released amount of PDGF-AA from the second sample was analyzed, 96th, 144th, and 192th hours decreased. The released amount of PDGF-AA surged by the 240th hour, dropped in the 288th hour, and then rose once again in the 336th hour. When the amount of PDGF-AA released from the third sample was examined depending on time, it was seen that it decreased at the 48th, 96th, 144th, and 192nd hours. The released amount of PDGF-AA grew between the 240th and 288th hours and was reduced by the 336th. When the time-dependent released amount of PDGF-AA from the fourth sample was evaluated, a declining release was seen between the 48th and 96th hours. The released amount of PDGF-AA increased at the 192nd and 240th hours and then reduced again at the 288th and 336th hours. When the time-dependent released amount of PDGF-AA from the fifth sample was evaluated, a declining release was seen between the 48th and 96th hours.
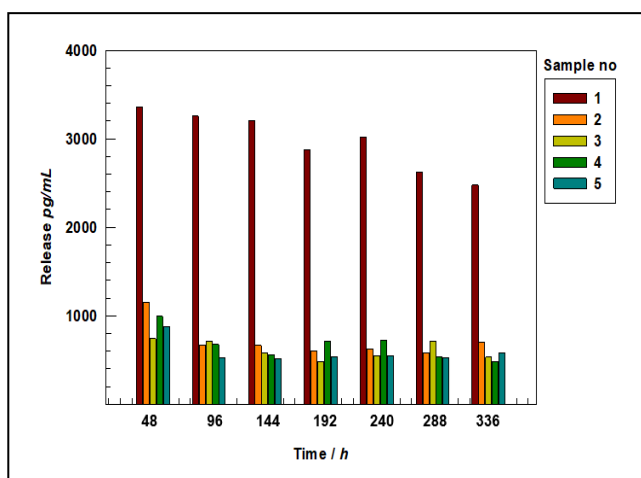

Figure 5. The release amount of PDGF–AA release over time from nanofiber surfaces loaded with APC (n=5)

The released amount of between the FGF, EGF, and PDGF-AA groups were significantly different in all time intervals from the 48th to the 336th hour, according to Table 3. Average release percentage for EGF, bFGF, and PDGF-AA in five samples after the release study; continued to decrease from respectively 17.55% to 13.06%; from 14.93% to 14.01%; from 18.11% to 12.97% from the 48th hour to the 336th hour. At the 48th, 96th, and 144th hours, paired comparisons revealed a difference between EGF and PDGF-AA, with EGF values being lower than PDGF-AA. After 192 hours, it was discovered that the EGF values were statistically considerably lower than those of the other 2 groups. When the time-dependent release differences in each group were examined, it was seen that there was no statistically significant difference in the bFGF group, while there was a significant difference in the EGF and PDGF-AA groups (Table 3).

Platelets contain more than 1,100 proteins, including GFs, immune system messengers, enzymes, enzyme inhibitors, and other bioactive compounds involved in various aspects of tissue repair [42]. Therefore, the determination of the sustained release of total protein may indirectly reflect the effect of APC sustained release within the dressing. In the present study, it was determined that the release of EGF and PDGF-AA decreased with time. The highest EGF and PDGF-AA release level was detected from all nanofiber samples in the first 48 hours. In the following periods, although there were no dramatic changes in the released amount of growth factors, release was observed. According to our experience, it can be suggested that due to the minimal differences in the number of cells during electrospinning on the nanofiber surface, the released factors may increase in concentration. Thanks to the sensor sensitivity of the sandwich ELISA method, non-dramatic fluctuations were observed. Trace, if not dramatic, changes in the release were observed for bFGF over all periods. Similar to our findings, there are release profiles of PRP-added wound dressings. For example; in the analysis of total protein released kinetics, Wang et al. found that PRP was almost completely released from the gauze in the first 12 hours, whereas the PRP-doped asymmetric chitosan/silk fibroin nano-silver (CTA-SF/Ag/SA) was released from the dressing in the first 36 hours. showed a gradual release [43]. In another study, PRP-derived growth factors were incorporated into silk fibroin/ PCL/PVA nanofibers by coaxial electrospinning to determine the release profiles of growth factors and how the presence of these growth factors enhances the osteogenic capabilities of nanofibers. Surfaces containing different ratios of PRP and PVA were prepared and characterized. The release of growth factors from the nanofibers over time was then measured. In conclusion, it was reported that combining PRP with coaxial nanofibrous positively affected its bioactivity and osteogenic ability [44]. Researchers coated biodegradable PCL surfaces with PRP to improve cell proliferation in another study. The surfaces were evaluated for mechanical properties (Young's modulus, tensile stress), sustained release of total protein, and growth factors (PDGF-BB, TGF-β1, and VEGF). In conclusion, it was stated that PRP-loaded PCL surfaces are promising for tissue regeneration applications [45]. In a study, macroscopically investigation of potential of the electrospun 2/1 %9 PVA / %1 NaAlg nanofibrous mats as wound dressing in vivo was purposed. In this research the results of show that it was concluded that the earliest and the latest wound contractions were obtained on the wounds dressed with Suprasorb-A and gauze, respectively. It is noteworthy that the performance of the electrospun PVA/NaAlg mat as wound dressing was higher than the performance of antibacterial Bactigras and gauze impregnated with a drug healing wound [46].

With the three-layer composite nanofiber structure developed within the scope of the study, the biological properties of APC are preserved; at the same time, it was observed that the release of growth factors contributing to wound healing occurred in the buffer solution in vitro depending on time.

Table 3. Comparison of growth factor release within and between groups

Duration	FGF	EGF	PDGF-AA	p
48th hours	622.38 (542.94-1559.75)	164.51 (135.00-443.87)	993.00 (741.79-3355.05)	**0.004***
96th hours	557.61 (500.17-1472.98)	128.27 (110.14-374.74)	679.44 (526.73-3254.74)	**0.008***
144th hours	492.84 (459.84-1271.33)	110.14 (106.26-393.38)	581.85 (514.08-3206.85)	**0.006***
192nd hours	550.28 (489.17-1403.32)	112.47 (97.98-349.63)	599.92 (479.74-2875.23)	**0.009****
240th hours	579.61 (511.17-1718.63)	113.51 (101.86-338.24)	620.71 (544.80-3018.00)	**0.009****
288th hours	583.27 (530.72-1611.08)	102.12 (97.98-294.22)	583.66 (526.73-2618.60)	**0.009****
336th hours	578.38 (491.61-1339.77)	114.29 (95.39-290.86)	577.33 (478.84-2478.54)	**0.009****
p	0.084	**0.012**	**0.016**	

*Statistically significant difference was found between EGF and PDGF-AA. **EGF statistically significant difference was found between and other groups

4. CONCLUSION

With the growth in global population, wound care management issues are becoming more and more crucial. The patient needs and some of the attributes needed in wound care cannot be met by traditional wound care productions. There is therefore a lot of room for research and development into contemporary wound dressings that contain the right medications or wound-healing agents. With nanofiber surfaces, it offers very ideal features for producing drug delivery systems that aid in wound healing while also developing desired wound care attributes. In this research, a multi-layer composite dressing that contains growth factor and contains APC was created for use in the treatment of wounds. It was found that the three-layer composite nanofiber surface with layered barrier control released APC in a time-dependent way. The electrospinning technique and other chemical solutions also prevented the APC-loaded composite nanofiber surface from having an impact on protein release. Up to the 336th hour, it was noticed that the release of growth factors from APC continued at low levels. Future research will benefit from the evaluation of APC-loaded composite nanofiber surfaces as a wound dressing in additional in vivo tests. These results are anticipated to serve as a guide for developing pertinent bioactive wound dressings.

REFERENCES

1. Jiang Y, Huang S, Fu X, Liu H, Ran X, Lu S, Hu D, Li Q, Zhang H, Li Y, Wang R. 2011. Epidemiology of chronic cutaneous wounds in China. *Wound Repair and Regeneration* 19(2), 181-188.

2. Sen CK, Gordillo GM, Roy S, Kirsner R, Lambert L, Hunt TK, Gottrup F, Gurtner GC, Longaker MT. 2009. Human skin wounds: A major and snowballing threat to public health and the economy. *Wound Repair and Regeneration* 17(6), 763-771.

3. Broussard KC, Powers JG. 2013. Wound dressings: Selecting the most appropriate type. *American Journal of Clinical Dermatology* 14(6), 449-59.

4. Simões D, Miguel SP, Ribeiro MP, Coutinho P, Mendonça AG, Correia IJ. 2018. Recent advances on antimicrobial wound dressing: A review. *European Journal of Pharmaceutics and Biopharmaceutics* 1(127), 130-141.

5. Chang CJ, Kazemzadeh-Narbat M. 2021. Innovation in wound care products: a FDA regulatory perspective. *Journal of Wound Care* 30(Sup2), 3-4.

6. Chermnykh ES, Kiseleva EV, Rogovaya OS, Rippa AL, Vasiliev AV, Vorotelyak EA. 2018. Tissue-engineered biological dressing accelerates skin wound healing in mice via formation of provisional connective tissue. *Histology and Histopathology from Cell Biology to Tissue Engineering* 33,1189-1199.

7. Stupin VA, Gabitov RB, Sinelnikova TG, Silina EV. 2018. Biological mechanisms of chronic wound and diabetic foot healing: The role of collagen. *Serbian Journal of Experimental and Clinical Research* 19(4), 373-82.

8. Langer C, Mahajan V. 2014. Platelet-rich plasma in dermatology. *JK Science* 16(4), 147.

9. Foster TE, Puskas BL, Mandelbaum BR, Gerhardt MB, Rodeo SA. 2009. Platelet-rich plasma: From basic science to clinical applications. *The American Journal of Sports Medicine* 37(11):2259-2272.

10. Gholami GA, Mohammadi M, Abrishami MR. 2014. Platelet rich plasma: Review of literature. *Journal of Dental School* 32(3), 176-186.

11. Dvorak HF, Brown LF, Detmar M, Dvorak AM. 1995. Vascular permeability factor/vascular endothelial growth factor, microvascular hyperpermeability, and angiogenesis. *The American Journal of Pathology* 146(5), 1029.

12. Cohen S, Carpenter G. 1975. Human epidermal growth factor: isolation and chemical and biological properties. *Proceedings of the National Academy of Sciences* 72(4), 1317-1321.

13. Norouzi M, Boroujeni SM, Omidvarkordshouli N, Soleimani M. 2015. Advances in skin regeneration: application of electrospun scaffolds. *Advanced Healthcare Materials* 4(8), 1114-1133.

14. Garcia-Orue I, Gainza G, Gutierrez FB, Aguirre JJ, Evora C, Pedraz JL, Hernandez RM, Delgado A, Igartua M. 2017. Novel nanofibrous dressings containing rhEGF and Aloe vera for wound healing applications. *International Journal of Pharmaceutics* 523(2), 556-566.

15. Wang Z, Qian Y, Li L, Pan L, Njunge LW, Dong L, Yang L. 2016. Evaluation of emulsion electrospun polycaprolactone/hyaluronan/ epidermal growth factor nanofibrous scaffolds for wound healing. *Journal of Biomaterials Applications* 30(6), 686-698.

16. Jang, C. S., Kim, S. I., Kim, H. K., Kweon, C. O., Kim, B. W., Kim, D. C., ... & Ryu, J. K. (2014). Plateletpheresis: The process, devices, and indicators of product quality. *Journal of Life Science 24*(9), 1030-1038.

17. McCullough, J. 2010. Overview of platelet transfusion. In *Seminars in Hematology* 47(3), 235-242. WB Saunders.

18. El-Timamy A, El Sharaby F, Eid F, El Dakroury A, Mostafa Y, Shaker O. 2020. Effect of platelet-rich plasma on the rate of orthodontic tooth movement: a split-mouth randomized trial. *The Angle Orthodontist* 90(3), 354-361.

19. Li J, Chen M, Wei X, Hao Y, Wang J. 2017. Evaluation of 3D-printed polycaprolactone scaffolds coated with freeze-dried platelet-rich plasma for bone regeneration. *Materials* 10(7), 831.

20. Zhang X, Yao D, Zhao W, Zhang R, Yu B, Ma G, Li Y, Hao D, Xu FJ. 2021. Engineering Platelet-Rich Plasma Based Dual-Network Hydrogel as a Bioactive Wound Dressing with Potential Clinical Translational Value. *Advanced Functional Materials* 31(8), 2009258.

21. Farzamfar S, Esmailpour F, Rahmati M, Vaez A, Mirzaii M, Garmabi B, Shayannia A, Ebrahimi E, Vahedi H, Salehi M. 2017. Poly-lactic acid/gelatin nanofiber (PLA/GTNF) conduits containing platelet-rich plasma for peripheral nerve regeneration. *International Journal of Health Studies* 3(2), 18.

22. Miroshnichenko S, Timofeeva V, Permyakova E, Ershov S, Kiryukhantsev-Korneev P, Dvořaková E, Shtansky DV, Zajíčková L, Solovieva A, Manakhov A. 2019. Plasma-coated polycaprolactone nanofibers with covalently bonded platelet-rich plasma enhance adhesion and growth of human fibroblasts. *Nanomaterials* 9(4), 637.

23. Unnithan AR, Barakat NA, Pichiah PT, Gnanasekaran G, Nirmala R, Cha YS, Jung CH, El-Newehy M, Kim HY. 2012. Wound-dressing materials with antibacterial activity from electrospun polyurethane–dextran nanofiber mats containing ciprofloxacin HCl. *Carbohydrate Polymers* 90(4), 1786-1793.

24. Alavarse AC, de Oliveira Silva FW, Colque JT, da Silva VM, Prieto T, Venancio EC, Bonvent JJ. 2017. Tetracycline hydrochloride-loaded electrospun nanofibers mats based on PVA and chitosan for wound dressing. *Materials Science and Engineering: C* 77, 271-281.

25. Choi JI, Kim MS, Chung GY, Shin HS. 2017. Spirulina extract-impregnated alginate-PCL nanofiber wound dressing for skin regeneration. *Biotechnology and Bioprocess Engineering* 22, 679-685.

26. Hsieh YL. 2000. Mat Characteristics of Polyester Fibers. Pastore CM, Kiekens P (Ed), *Mat Characteristics of Fibers and Textiles.* New York: Markel Dekker Inc. p.33-57.

27. Cordenonsi LM, Faccendini A, Rossi S, Bonferoni MC, Malavasi L, Raffin R, ... & Ferrari F. 2019. Platelet lysate loaded electrospun scaffolds: Effect of nanofiber types on wound healing. *European Journal of Pharmaceutics and Biopharmaceutics*, 142, 247-257.

28. Karuppannan SK, Dowlath MJ, Ramalingam R, Musthafa SA, Ganesh MR, Chithra V, Ravindran B, Arunachalam KD. 2022. Quercetin functionalized hybrid electrospun nanofibers for wound dressing application. *Materials Science and Engineering: B* 285, 115933.

29. Tanha S, Rafiee-Tehrani M, Abdollahi M, Vakilian S, Esmaili Z, Naraghi ZS, Seyedjafari E, Javar HA. 2017. G-CSF loaded nanofiber/nanoparticle composite coated with collagen promotes wound healing in vivo. *Journal of Biomedical Materials Research Part A* 105(10), 2830-2842.

30. Kim SE, Heo DN, Lee JB, Kim JR, Park SH, Jeon SH, Kwon IK. 2009. Electrospun gelatin/polyurethane blended nanofibers for wound healing. *Biomedical Materials* 4(4), 044106.

31. Yang Y, Hu H. 2017. Spacer fabric-based exuding wound dressing–Part II: Comparison with commercial wound dressings. *Textile Research Journal* 87(12), 1481-1493.

32. Zhang C, Yuan X, Wu L, Han Y, Sheng J. 2005. Study on morphology of electrospun poly (vinyl alcohol) mats. *European Polymer Journal* 41(3), 423-432.

33. Hashmi M, Ullah S, Ullah A, Khan MQ, Hussain N, Khatri M, Bie X, Lee J, Kim IS. 2020. An optimistic approach "from hydrophobic to super hydrophilic nanofibers" for enhanced absorption properties. *Polymer Testing* 90, 106683.

34. Zhao JH, Xu L, Liu Q. 2015. Effect of ethanol post-treatment on the bubble-electrospun poly (vinyl alcohol) nanofiber. *Thermal Science* 19(4), 1353-1356.

35. Selçuk E, Calapoğlu NŞ. 2022. Overview of primary messengers and their receptors. *Suleyman Demirel University Journal of Health Sciences* 13(3), 559-566.

36. Fredenberg S, Wahlgren M, Reslow M, Axelsson A. 2011. The mechanisms of drug release in poly (lactic-co-glycolic acid)-based drug delivery systems--a review. *International Journal of Pharmaceutics* 415(1-2), 34–52.

37. Shah SS, Cha Y, Pitt CG. 1992. Poly (glycolic acid-co-dl-lactic acid): diffusion or degradation-controlled drug delivery? *Journal of Controlled Release* 18(3), 261-270.

38. Kajdič S, Planinšek O, Gašperlin M, Kocbek P. 2019. Electrospun nanofibers for customized drug-delivery systems. *Journal of Drug Delivery Science and Technology* 51, 672-681.

39. Laha A, Sharma CS, Majumdar S. 2017. Sustained drug release from multi-layered sequentially crosslinked electrospun gelatin nanofiber mesh. *Materials Science and Engineering: C* 76, 782-786.

40. Li T, Ding X, Tian L, Hu J, Yang X, Ramakrishna S. 2017. The control of beads diameter of bead-on-string electrospun nanofibers and the corresponding release behaviors of embedded drugs. *Materials Science and Engineering: C* 74, 471-477.

41. Ceylan M, Yang SY, Asmatulu R. 2017. Effects of gentamicin-loaded PCL nanofibers on growth of Gram positive and Gram-negative bacteria. *International Journal of Applied Microbiology and Biotechnology Research* 5, 40-51.

42. Arnoczky SP, Shebani-Rad S. 2013. The basic science of platelet-rich plasma (PRP): What clinicians need to know? *Sports Medicine and Arthroscopy Review* 21(4), 180-185.

43. Wang Q, Qian Z, Liu B, Liu J, Zhang L, Xu J. 2019. In vitro and in vivo evaluation of new PRP antibacterial moisturizing dressings for infectious wound repair. *Journal of Biomaterials Science, Polymer Edition* 30(6), 462-485.

44. Cheng H, Yang X, Che X, Yang M, Zhai G. 2018. Biomedical application and controlled drug release of electrospun fibrous materials. *Materials Science and Engineering:C* 90, 750-763.

45. Diaz-Gomez L, Alvarez-Lorenzo C, Concheiro A, Silva M, Dominguez F, Sheikh FA, Cantu T, Desai R, Garcia VL, Macossay J. 2014. Biodegradable electrospun nanofibers coated with platelet-rich plasma for cell adhesion and proliferation. *Materials Science and Engineering:C* 40, 180-188.

46. Üstündağ GC, Karaca E, Özbek SE, Çavuşoğlu İ. 2010. In vivo evaluation of electrospun poly (vinyl alcohol) /sodium alginate nanofibrous mat as wound dressing. *Tekstil ve Konfeksiyon* 20(4), 290-298

Comparison of Stain Removal Characteristics of Knitted Structures

Berna Cüreklibatır Encan[1] 0000-0002-4493-7079
Arzu Marmaralı[2] 0000-0001-6251-0645

[1] Ege University / Emel Akın Vocational Training School / Bornova, İzmir, Türkiye
[2] Ege University / Faculty of Engineering Textile Engineering Department / Bornova, İzmir, Türkiye

Corresponding Author: Berna Cüreklibatır Encan, berna.encan@ege.edu.tr

ABSTRACT

The subject of stains and stain removal has great importance to the professional lives of textile researchers and the daily lives of the public. Therefore, stain removal characteristics of five different types of 100% cotton knitted fabrics (single-jersey, piquet, 3-thread fleece, 1x1 rib, and interlock) commonly used for casual wear were investigated in this study. Samples were stained with three types of common stains, and the effects of various fabric properties on stain removal characteristics were investigated. The stain removal performance was evaluated both objectively via a spectrophotometer and subjectively by Grey Scale grading. According to the results, fabric structure had a significant effect on stain removal characteristics. 1x1 rib and single jersey were the most difficult structures for stain removal, whereas, piquet fabric was the most convenient. Additionally, tomato paste was the most difficult stain to remove, whereas chocolate milk was the easiest.

1. INTRODUCTION

Staining and stain removal of fabrics by laundering are important issues in both daily life and textile literature. Laundering is a process in which physical and chemical effects interact in the washing water. The first phase of laundering is the removal of soil from the fabric, the second phase is stabilizing the soil to prevent redeposition onto the fabric and the last phase is removing dirt and chemicals from the laundry with the help of rinsing process [1]. A successful soil removal by washing depends largely on factors such as fabric type, the type of soil, wash load, type of washing machine, water quality, applied washing conditions (amount and type of mechanical action, time, and temperature), and the composition of the detergent [2-4]. Efficient cleaning is only possible when certain factors such as chemical action, mechanical action, temperature, and time come together [1]. Researchers in the field of textiles have long been studying the removal of stains from the surface of textiles left by the soils and the effects of various washing conditions on stain removal.

Bueno et al. [5] studied the modeling of the kinetics of stain removal from cotton-knitted fabrics using a commercial washing machine. They focused on the physical process of stain removal by varying the textile load, washing time, and drum rotational speed. A new mathematical model was suggested to explain the effect of mechanical action present during the washing process and the extent of stain removal. Fen-Juan et al. [6] investigated the usage of image analysis in determining the degree of stain removal. In that study, standard stain cloths were washed under various washing conditions, and washing efficiency was analyzed. Additionally, the stain photos taken before and after washing were compared via image analysis. As a result, it was concluded that the results of washing efficiency and image analysis were significantly correlated, and image analysis could be used to evaluate stain removal.

In the literature review, it is seen that there are various studies on stain resistance. Kabbari et al. [7] studied predicting the stain-repellency characteristics of plush knitted fabrics by comparing surface response and fuzzy logic methods. It was observed that the fuzzy logic model

had a better prediction performance, and it could be applied in the knitting industry. Chauhan et al. [8] evaluated the mechanical, chemical, thermal, and UV stability of the superhydrophobic cotton fabric. They developed a modified cotton fabric with self-cleaning and stain-resistant properties with a proposed method. Pallye and Ghosh [9] developed a super-hydrophobic and stain-repellent fabric finish. Additionally, a stain-repellent fabric for use in aircraft upholstery was designed by Kuruppu [10].

Moreover, forensic scientists are interested in staining characteristics of various fabrics, as well. Because apparel with bloodstains is important evidence, bloodstain pattern analysis (BPA) has become a popular research topic in the field of forensic science [11]. Miles et al. [12] investigated fabric surface characteristics for satellite bloodstain morphology using a pair of denim jeans (98/2% cotton/elastane) and a t-shirt (95/5% cotton/elastane) selected for staining. It was concluded that surface roughness influences the morphology of stains generated and the increasing of surface roughness leads to an increase in the number and extent of satellite stains. Dicken et al. [13] stated that factors of bloodstain size for non-absorbent surfaces are still being investigated, however, interactions between blood and fabrics are still quite unknown. Therefore, they used a micro-computed tomography (CT) scanner to examine the bloodstain size and shape on the surfaces of the 100% cotton rib knit and 100% cotton drill woven fabrics. It was observed that the bloodstain morphology depended on both the impact velocity and fabric structure. De Castro et al. [11] examined the effect of various factors affecting appearances, such as prior laundering, fiber content, fabric structure, and blood impact angle on drip bloodstain appearance. They used four different fabrics that are 100% cotton plain woven, 100% polyester plain woven, a blend of polyester and cotton plain woven, and 100% cotton single jersey knit fabrics. It was observed that the bloodstain characteristics change according to fiber content and fabric structure and these factors should be taken into consideration while interpreting bloodstain patterns. Williams et al. [14] researched the impact dynamics of porcine drip bloodstains on fabrics. The number and size of satellite stains were examined on two types of 100% cotton fabrics (a plain woven bed sheet and a jersey knit). A correlation was observed between surface roughness and some satellite bloodstains. A higher number of satellite stains occurred on more rough surfaces. Furthermore, Nolan et al. [15] thought that in some criminal cases victims' clothes may have been washed several times before a criminal investigation. Therefore, they investigated the effects of repeated washing process and fabric type on the permanence of seminal fluid and spermatozoa using various fabrics (cotton, nylon, cotton terry towel, polyester fleece, satin, and lace) laundered up to six times. However, it was concluded that further research should be conducted to distinguish the effects of fabric construction.

Despite significant results concluded by forensic researchers, comparing two quite different fabric types, (knitted and woven fabrics), may not be sufficient from a textile point of view. Because many characteristics such as fabric production method (knitted, woven, or nonwoven), the structure of knitted fabric (single jersey, rib, interlock, etc.) and woven fabric (plain, twill, satin, etc.), and the yarn material have important effects on staining behavior of the fabrics. To overcome this lack, collaborations between forensic and textile researchers were formed. Li et al. [16] examined the effect of yarn production methods on wicking and bloodstain pattern analysis (BPA) on woven cotton fabrics. They observed that fabrics made with ring-spun yarns wicked more blood than open-end and vortex yarns. In another study, Baby et al. [17] investigated the effects of yarn count and blood drop size on wicking and bloodstains on textiles. It was concluded that samples knitted with finer yarns had larger stains. Wu et al. [18] dropped the blood on three 100% cotton single jersey knit fabrics with different yarn counts and also onto paper. Results showed that number and area of the stains decreased, as the yarn count decreased.

Although staining and stain removal characteristics of fabrics are significant subjects in both academic and daily life, it is observed that the influence of fabric structure, a main characteristic of fabrics, on stain removal is not investigated in detail. Therefore, in this study, the stain removal characteristics of five different knitted fabrics frequently used in casual garments were examined. To simulate some common stains, three different types of stains were used (tomato paste, red wine, and chocolate milk).

2. MATERIAL AND METHOD

2.1 Material

To include knitted structures that are frequently used in daily life in the scope of the experiment, five knitted fabrics knitted in different structures using 100% cotton ring yarn were supplied by a textile company. To create a wide range of fabrics, structures produced on both single-bed and double-bed circular knitting machines were included in the research. While three fabric structures (single-jersey, piquet, and 3-thread fleece) were knitted on a single-bed circular knitting machine, others (1x1 rib and interlock) were produced on a double-bed circular knitting machine.

2.2 Method

As the aim of this study is to investigate the effect of fabric structure on the stain removal property, some fabric characteristics that were expected to influence the porosity were measured besides fundamental fabric properties. Because Bueno et al. [5] stated that stain removal of textiles depends on two main porosities of fabrics. The first and

larger porosity are the spaces between the yarns (inter-yarn), and the second and smaller porosity are the spaces between fibers within the yarns (intra-yarn).

The measured properties were mass per unit area, courses per cm, wales per cm, fabric thickness, air permeability, and hydrophility. Mass per unit area, courses per cm, and wales per cm determine the amount of yarn in the unit area. Fabric thickness is a significant parameter for successful stain removal as it defines the distance that washing liquor should travel between the front and the back sides of the fabric. These values collectively affect the fabric density and fabric tightness, thus, fabric porosity. Air permeability value is known to be directly related to fabric porosity. The coefficient of friction identifies the surface roughness of the fabric. A smoother surface provides a larger contact area for the washing liquor resulting in a more effective stain removal than a rougher surface. In addition, the hydrophility of the samples affects the wicking of the soils. Moreover, *L (luminance)* values of the clean fabrics (before staining and washing) are measured to observe if the luminance of the samples affects stain removal performance. Since generally preferred fabrics in casual garments were chosen as the test samples in this study, some other properties are quite different from each other, except for the fiber content used. Therefore, the fabric density value was used to compare the fabrics with each other. The fabric density is the weight per unit volume of the fabric that allows for determining how strong, dense, and permeable the fabric is. Therefore, this parameter was calculated to evaluate some properties of the samples using Equation (1):

$$FD = m_s/t \qquad (1)$$

where: FD – fabric density, [g/cm^3]; m_s – mass per unit area of the fabrics [g/m^2]; t – fabric thickness [mm]. The used symbols, units, related test standards, used test devices, and repetitions of tests for each parameter during tests are listed in Table 1.

All samples were conditioned before measurements and the tests were conducted in standard atmosphere conditions. Stitch diagrams and measured properties of five different fabric structures are given in Table 2.

As per the International Association for Soaps, Detergents and Maintenance Products (A.I.S.E.), soil types are classified as bleachable, enzymatic, particulate, and greasy. Bleachable and enzymatic soils are predominantly preferred for laundry detergent performance tests [19]. They are quite common in consumer habits and are usually easier to remove without a pre-treatment. Therefore, chocolate milk (enzymatic), red wine (bleachable), and tomato paste (bleachable) were selected for this study. Because of the denser character of tomato paste, 15 g of tomato paste was diluted with 50 ml of water to obtain a homogeneously applicable soil. Each type of soil was poured into a clean bowl. Soils were applied to the fabrics via a brush and a circular templet with a 5 cm diameter (Figure 1) in standard atmosphere conditions.

Figure 1. Circular templet used for soiling

Table 1. Tested parameters and related test standards

Parameter	Symbol	Unit	Related standard	Test device	Repetition
Mass per unit area	m_s	g/m^2	TS EN 12127:1999	Digital scale with .000 accuracy	3 times
Course per cm	cpc	-	TS EN 14971: 2006	Magnifying glass	3 times
Wale per cm	wpc	-	TS EN 14971: 2006	Magnifying glass	3 times
Thickness	t	mm	TS 3374 ISO 1765: 2004	Wira Digital Thickness Gauge (2 kPa presser foot)	3 times
Fabric density	FD	g/cm^3	-	Calculated	-
Coefficient of friction	μ_k	-	-	Frictorq	3 times
Air permeability	AP	l/m^{2}s	ISO 9237:1995	Textest FX 3300 (pressure difference of 100 Pa and sample area of 20 cm^2)	10 times
Hydrophility	H	s	AATCC 79:2007	Burette	5 times
Luminance	L	-	ASTM E1331	HunterLab UltraScan PRO spectrophotometer	4 times
Color difference	ΔR	-	ASTM E1331	HunterLab UltraScan PRO spectrophotometer	4 times

Table 2. Stitch diagrams and measured properties of samples

Fabric structure	Yarn count	m_s	cpc	wpc	t	FD	μk	AP	L	H	Stitch diagram
	Ne	g/m²	course/cm	wale/cm	mm	g/cm³		l/m²s	-	s	
Single jersey	35	220	19	15	0.70 a	0.31	0.2948 a	187 a	93.47	12	
Piquet	30	180	16	13	0.78 b	0.23	0.3494 b	540 b	96.20	14	
Fleece (Three thread)	50/50/20	200	18	12	1.17 c	0.17	0.3681 c	652 c	93.69	4	
1x1 Rib	30	200	16	11	0.89 B	0.22	0.3048 A	393 B	87.79	60+	
Interlock	40	200	17	16	0.83 A	0.24	0.3085 A	319 A	96.48	3	

Four samples were created for each kind of stain for repetition. After 24 hours, stained parts of the samples were folded in four layers, and measurements were taken in a wale direction with a HunterLab UltraScan PRO spectrophotometer. The reflectance values of the samples were recorded at 460 nm wavelength.

Then, samples were laundered in a Type A washing machine according to ISO 6330: 2012 (E) (Procedure No. 4N, normal washing) with 20 g of Reference detergent 2. Washed samples were laid on a flat surface to dry for 24 hours. Afterward, spectrophotometer measurements were repeated in the same way. From the reflectance values measured before and after washing, the color differences (ΔR) were calculated as shown in Equation (2) [20]. As it is known, higher ΔR means better stain removal.

$$\Delta R = RA - RB \qquad (2)$$

Where; RA: Reflectance value after washing, RB: Reflectance value before washing, and ΔR: Amount of stain removal

Photos of created stains before and after washing are given in Table 3. Stains are lined as tomato paste, red wine, and chocolate milk from top to bottom, respectively.

In addition to the objective evaluation using a spectrophotometer instrument, subjective evaluation was conducted by three experts in this field. AATCC Grey Scale for Staining was used for staining evaluation subjectively. In this scale, the colors of the samples are rated from 1 to 5 (including half steps), where grade 1 means the highest color change while grade 5 means no color change [21].

As known, fabric structures knitted on single-bed and double-bed machines are quite different. Thus, the results of single and double-layer samples were evaluated separately. Test results were evaluated using the software PASW Statistics 18 with a 95% confidence in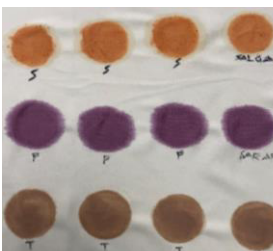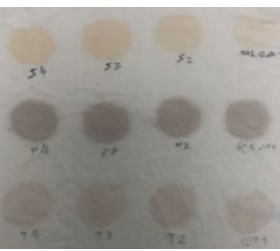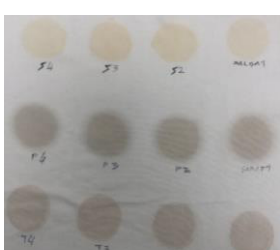terval. Applied tests to determine the statistical importance of the variations were decided according to the number of fabric structures. The statistical method analysis of variance (ANOVA) and Independent-Samples T Test were applied to single-bed and double-bed samples, respectively. The probability values or p-values were examined to determine whether the parameters were significant or not. If the p-value of a parameter is greater than 0.05 (p>0.05), the parameter was accepted as insignificant and was ignored. When the p-value was stated as lower than 0.05 (p<0.05), then the Student-Newman-Keuls (S-N-K) posthoc test was used for homogeneous variance and Tamhane's T2 posthoc test was used for heterogeneous variance.

Table 3. Created stains before and after washing

Fabric structure	Before washing	Soil type	After washing
Single jersey		Tomato paste	
		Red wine	
		Chocolate milk	
Piquet		Tomato paste	
		Red wine	
		Chocolate milk	
Fleece (Three thread)		Tomato paste	
		Red wine	
		Chocolate milk	
1x1 Rib		Tomato paste	
		Red wine	
		Chocolate milk	
Interlock		Tomato paste	
		Red wine	
		Chocolate milk	

3. RESULTS AND DISCUSSION

Because Smulders [4] stated that the type of fiber determines the degree of hydrophobicity/hydrophilicity, the wettability, and the extent of soil removal, the fiber type parameter is kept constant. Stain removal results tested by both objective and subjective methods of the samples are given in Table 4. To show the significance level of the difference between mean values in Tables 2 and 4, the measured mean values for each property are marked with letters (from "a" to "c"). The letter "a" shows the lowest value, while the letter "c" presents the highest. Lowercase letters were used for single-layer samples, while uppercase letters were used for double-layer fabrics. Mean values marked with the same letter indicate that they are not significantly different.

As it is known, the p=0.000 value means measured values are significantly different from each other in statistical analysis. Therefore, it is possible to say that the coefficient of friction, air permeability, and ΔR values of fabric samples (Figure 2 and Figure 3) for tomato paste, red wine, and chocolate milk stains are significantly different from each other.

Table 4. Stain removal results of the samples

Fabric structure	ΔR			Grey Scale Grading		
	Tomato paste	Red wine	Chocolate milk	Tomato paste	Red wine	Chocolate milk
Single jersey	14.99 a	18.91 a	22.87 a	2	2-3	3
Piquet	30.59 b	38.40 c	35.63 c	3	3-4	4
Fleece (Three thread)	30.64 b	22.24 b	27.31 b	4	2	3
1x1 Rib	14.62 A	18.24 A	23.07 A	1-2	2	3-4
Interlock	26.04 B	42.13 B	34.24 B	2-3	3	2-3
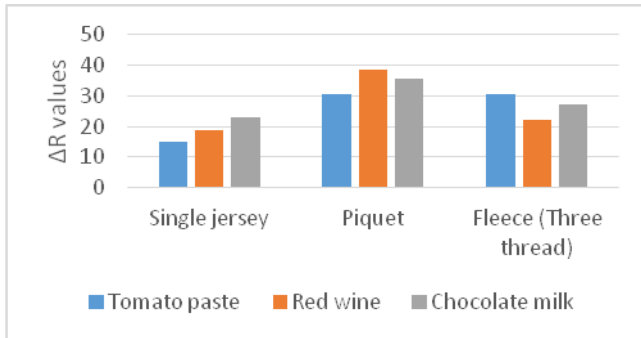
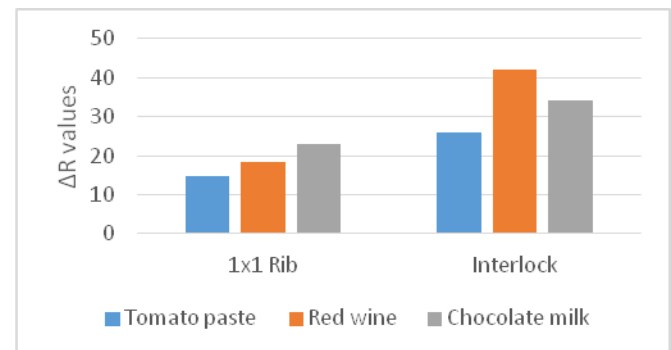Figure 2. ΔR values of single-layer samples

When the samples produced on a single-bed knitting machine were compared, it was observed that the single jersey fabric had the lowest ΔR value for all stain types. As mentioned before, the lower ΔR value shows that the stain removal capacity from this fabric is poor. This result can be explained by the highest fabric density values of single jersey fabric. As explained in a previous study, the higher fabric density means that the fabric contains more yarn in unit volume [22]. In this case, because of the higher fabric density value, both water and detergent will not be able to reach the stain effectively. Furthermore, as is expected stain is trapped in a dense structure and cleaning can be more difficult for a dense structure than a sparse one. Single jersey structure has the lowest air permeability value among the used fabrics as well. Lower air permeability is related to a lower porosity leading to a less successful stain removal. Additionally, it is seen that Grey scale results obtained from subjective evaluations are compatible with the spectrophotometer results.

Piquet fabric investigated in this study has the best stain removal results of single-layer fabrics. This fabric has lower fabric density and higher air permeability than the single jersey sample because of the tucks between stitches. Because of the lower fabric density both water and detergent reached the stain effectively, and the stain could be easily removed from the fabric structure. Furthermore, a higher air permeability, which is a strong indicator of higher porosity [23], enables the access of both water and detergent. Grey-scale results were similar to the spectrophotometer results of the piquet sample.

Although three-thread fleece fabrics are knitted on the single-bed machine, they have a quite different structure from piquet and single jersey because of comprising three

yarns in one course. The three-thread fleece consists of a face yarn, a binding yarn (usually in the same yarn count as the face yarn), and a thicker fleece yarn [24]. This structure has the highest air permeability and the lowest fabric density among the samples knitted on single-bed machines. Yet, a general result can not be reached for its characteristic of stain removal. Because the stain removal level is the same as the piquet structure for tomato paste, on the other hand, the removal level of red wine and chocolate milk stain for three-thread fabric is between the other two structures. As given in Table 4, it is observed that the results of the spectrophotometer and Grey scale are compatible with each other for all kinds of stains on fleece fabric.

Moreover, according to the statistical analysis, the stain removal results strongly depend on the kind of stain for both objective and subjective evaluations, and tomato paste stain is the least removed stain, except for the fleece structure.

Figure 3. ΔR values of double-layer samples

When double-layer samples are examined, as is expected, it is seen that the 1x1 rib structure has lower fabric density and higher air permeability values. According to the results, 1x1 rib fabric has quite low stain removal results and this means that created stains could not be removed from this fabric structure effectively. 1x1 rib structure consists of one face and one reverse stitched wale, respectively. However, wales with reverse stitches are placed behind the wales with face stitches. That is why reverse wales can only be seen when the fabric is stretched widthwise. Therefore, reverse wales are not fully exposed from both the front and back of the fabric. This may result in a smaller contact area between the fabric and detergent, leading to poor stain removal.

Grey scale gradings and spectrophotometer results of the 1x1 rib sample are mostly aligned.

Although interlock fabric consists of two 1x1 rib fabrics knitted together, it has quite similar values of fabric density and coefficient of friction to 1x1 rib fabric, as seen in Table 2. Yet, ΔR values of interlock are higher than 1x1 rib for all stain types. Spectrophotometer results and Grey scale gradings are mostly compatible for interlock fabric.

When single and double-layer fabrics are considered together, piquet, fleece, and interlock samples have higher ΔR values than single jersey and 1x1 rib fabrics resulting in better stain removal, depending on the type of stain. Regarding red wine and chocolate milk stains, piquet, and interlock samples' ΔR values are significantly higher than fleece fabric. On the other hand, piquet and fleece have better stain removal results in tomato paste stains. Within all five structures, piquet can be regarded as the most convenient fabric structure for stain removal with its higher ΔR and Grey scale results. As per Grey Scale results, chocolate milk stain is considered to be easier to remove than tomato paste and red wine stains. Furthermore, it is observed that ΔR and Grey scale are mainly compatible for the chosen stains.

When the stain removal results and fabric characteristics are evaluated altogether, it can be expressed that among the measured properties fabric density and air permeability are significantly related to a successful stain removal, whereas the coefficient of friction does not have an obvious impact. As it is known, staining and removal of the stain from a fabric surface is rather a complex process and it is affected by various parameters. The cotton fabrics used in the study were provided by a textile company, thus there are discrepancies in some of their structural and mechanical properties. Therefore, it is thought that the stain removal characteristic of fabrics might be due to other characteristics besides fabric density. That is why, hydrophility and luminance of the samples are measured as well. The hydrophility of the samples is expected to be a major factor affecting stain removal characteristics. Hydrophility values present that single jersey, piquet, fleece, and interlock samples are hydrophilic, while 1x1 rib fabric is hydrophobic. However, a consensus about the effect of hydrophility on stain removal can not be reached within this study. The only hydrophobic sample, 1x1 rib, provides lower stain removal results in reflectance and Grey scale grading. Similarly, single jersey, a hydrophilic sample, also presents lower results. A general comment can not be made about the hydrophilic fabrics as well.

Luminance (*L*) values of the samples are quite similar to each other, except for the 1x1 rib sample as seen in Table 2. *L* value of the rib fabric is lower than the other samples. It means that the rib fabric color is a little darker than the others. This may result in a poor reading of stain removal, as the reflectance value may be negatively affected. A darker color may lead to a lower ΔR, even if the stain is well removed. When the result in Table 4 is analyzed, it can be seen that the rib sample presents lower results in ΔR and Grey scale grading.

When the chosen soils are compared, it can be said that tomato paste is the hardest stain to remove, whereas chocolate milk is the easiest according to the results. This outcome is more visible in Grey scale grading and results. As mentioned before, tomato paste and red wine stains are bleachable, whilst chocolate milk is enzymatic. It should be taken into consideration that the detergent used in this study contains enzymes, which may affect the better stain removal results of chocolate milk.

4. CONCLUSION

The subject of staining and removing stains are major concerns for both the professional life of textile academics and the daily life of the public. Literature research in the field of textiles suggests that recent studies generally focus on the effect of various washing parameters on stain removal and stain repellency. Staining characteristics of fabrics have become a popular and important subject in the field of forensic sciences in recent years. Since the evidence in the crime scene examined by the authorities often includes fabrics, staining characteristics of various samples play a major role in forensics. Therefore, some frequently used knitted structures (single jersey, piquet, three-thread fleece, 1x1 rib, and interlock) were stained with commonly seen stains, and the effects of various fabric properties on their stain removal characteristics are investigated in this study. Stain removal performance was evaluated both objectively via a spectrophotometer and subjectively by Grey Scale grading.

Results of ΔR and Grey scale grading presented that, between studied fabrics, 1x1 rib, and single jersey were the most difficult structures for stain removal, whereas piquet fabric was the most convenient. The reason for the poor stain removal characteristic of 1x1 rib fabric is thought to be its structure causing a lower contact area. For the single jersey sample, the lower porosity of fabric and lower air permeability, because of higher fabric density is considered to result in less stain removal. On the other hand, piquet fabric, with its lower fabric density and higher air permeability due to tuck stitches in its structure, provided the best stain removal performance for this study. It can be concluded that tomato sauce is the most difficult stain to remove from the fabric surface, while chocolate milk is the easiest regardless of the structure.

When the results were evaluated, it is observed that fabric structure significantly affects stain removal capacity. Fabric density and air permeability were found to have a significant effect on stain removal, while the influence of the coefficient of friction, hydrophility, and luminance was not evident in this study.

Five different types of knitted fabrics often preferred in casual garments are investigated in this study. It is observed that fabric structure substantially affects stain removal

characteristics. Moreover, fabrics have many parameters that may influence their staining properties. Since the staining characteristic of fabrics plays a significant role in forensic science, it may have great importance to establish a database including various fabric types, structures, raw materials, etc. with the collaboration of textile and forensic academics.

REFERENCES

1. Gündüz Balpetek F, Gülümser T. 2016. The effects of some ingredients in the structure of household laundry detergents over the whiteness of textile materials *Pamukkale Üniverstesi Mühendislik Bilimleri Dergisi* 22(7), 597-604.

2. Biranje SS, Nathany A, Mehra N, Adivarekar R. 2015. Optimisation of detergent ingredients for stain removal using statistical modeling *Journal of Surfactants and Detergents* 18, 949-956.

3. Gülümser T. 2010. Soil releasing effect of concentrated detergents compared with the ordinary ones *Tekstil ve Konfeksiyon* 4, 329-335.

4. Smulders E. 2002. *Laundry Detergents.* Weinheim: Wiley-VCH.

5. Bueno L, Laso C, Amador C, Bakalis S. 2019. Modelling the kinetics of stain removal from knitted cotton fabrics in a commercial Front Loader Washing Machine (FLWM) *Chemical Engineering Science* 200, 176-185.

6. Fen-Juan S, Pinghua X, Weichao F, Yulong Y, Xuemei D, Xiongying W. 2020. Evaluation of stain release based on image histogram analysis *Industria Textila* 71(3), 204-208.

7. Kabbari M, Fayala F, Ghith A, Liouane N. 2017. Predicting stain repellency characteristics of knitted fabrics using fuzzy modeling and surface response methodology *The Journal of The Textile Institute* 108(5), 683-691.

8. Chauhan P, Kumar A, Bhushan B. 2019. Self-cleaning, stain-resistant and anti-bacterial superhydrophobic cotton fabric prepared by simple immersion technique *Journal of Colloid and Interface Science* 535, 66-74.

9. Pallye R, Ghosh S. 2020. Development of super-hydrophobic and stain repellent fabric finish *IOP Conference Series: Materials Science and Engineering* 827, 012003.

10. Kuruppu KADD. 2021. Surface treated cotton fabric with stain repellent property for the use in aircraft upholstery. *Journal of Engineered Fibers and Fabrics* 16, 1-9.

11. De Castro TC, Carr DJ, Taylor MC, Kieser JA, Duncan W. 2016. Drip bloodstain appearance on inclined apparel fabrics: Effect of prior-laundering, fibre content and fabric structure *Forensic Science International* 266, 488-501.

12. Miles HF, Morgan RM, Millington JE. 2014. The influence of fabric surface characteristics on satellite bloodstain morphology *Science & Justice* 54(4), 262-266.

13. Dicken L, Knock C, Beckett S, de Castro TC, Nickson T, Carr DJ. 2015. The use of micro computed tomography to ascertain the morphology of bloodstains on fabric *Forensic Science International* 257, 369-375.

14. Williams EMP, Dodds M, Taylor MC, Li J, Michielsen S. 2016. Impact dynamics of porcine drip bloodstains on fabrics *Forensic Science International* 262, 66-72.

15. Nolan A, Speers SJ, Murakami J, Chapman B. 2018. A pilot study: The effects of repeat washing and fabric type on the detection of seminal fluid and spermatozoa *Forensic Science International* 289, 51-56.

16. Li X, Li J, Michielsen S. 2017. Effect of yarn structure on wicking and its impact on bloodstain pattern analysis (BPA) on woven cotton fabrics *Forensic Science Internaitonal* 276, 41-50.

17. Baby R, Michielsen S, Wu J. 2021. Effects of yarn size and blood drop size on wicking and bloodstains in textiles *Journal of Forensic Sciences* 66, 1246-1256.

18. Wu J, Michielsen S, Baby R. 2019. Impact Spatter Bloodstain Patterns on Textiles *Journal of Forensic Sciences* 64(3), 702-710.

19. International Association for Soaps, Detergents and Maintenance Products. 2023, October 5. A.I.S.E. laundry detergent testing guidelines [pdf]. Retrieved from https://www.aise.eu/documents/document/20201002111904-laundry_detergent_testing_guidelines_v_7,_october_2020_v1.pdf

20. Cireli A, Sarışık M, Kutlu B, Yaman V. 2004. The effects of washing conditions on soil removal in domestic laundering processes *AUTEX Research Journal* 4(2), 101-112.

21. Wang M, Chapman L, Moore M, Suh M. 2019. Replication of screen-printing fabric via ink-jet textile printing *Journal of Imaging Science and Technology* 63(4), 040402-1-040402-10.

22. Cüreklibatır Encan B, Marmaralı A. 2023. Effect of tuck loops on fabric properties of cardigan derivative structures *Dokuz Eylül University Faculty of Engineering Journal of Science and Engineering* 25(73), 149-158.

23. Sıddıqui MOR, Ali M., Zubair M., Sun D. 2018. Prediction of air permeability of knitted fabric by using computational method *Tekstil ve Konfeksiyon* 28(4), 273-279.

24. Asker Ğ, Balcı O. 2022. Investigation of the effect of raising and finishing process on the physical performance of 3-thread fleece fabric *Tekstil ve Konfeksiyon* 32(3), 183-192.

Improvement of Mechanical And Light Transmittance Properties of PU Foam Coated Curtain Fabrics

Aslıhan Koruyucu [1*] [ID] 0000-0002-8443-5188
Gözde Kartal[2] [ID] 0009-0009-3868-7147

[1]Namık Kemal University/ Faculty of Engineering/ Textile Engineering Department, Tekirdağ, Türkiye
[2]Akın Tekstil, Kırklareli, Türkiye

Corresponding Author: Aslıhan Koruyucu, adelituna@nku.edu.tr

ABSTRACT

In foam coating, the main factors are the foam density of the coating material and the compatibility among foam structure, the coating material and the fabric surface. In this study, the results of breaking force and elongation, tear strength and light transmittance were compared according to the fabric structure, coating recipes, foam density and the foam coating layer viscosity statistically. And also, air permeability, aged under artificial light and weathering tests were evaluated. The high yarn density of warp threads per unit length in polyester woven fabric leads to an increase in tensile strength. The best results in tensile strength and elongation at break experiments were acquired at coating recipe 4. As a result, the minimum light transmittance value was 1.04 and the maximum light transmittance value was 1.12 by using coating recipe 4, respectively. Air permeability values of PU foam coated fabrics were in the range of 0-2 mm/s, whereas air permeability value of untreated polyester fabric was measured as 17.36 $l/m^2/s$. Maximum air permeability was obtained in coating recipe 4. The higher air permeability values also gave better barrier to air penetration. The air permeability of coated fabrics were very low due to pore size. The coating material covered the pores of the untreated fabric and restricted air permeability. The color fastness to artificial light of the PU foam coated fabric samples were very good. The fading degree of PU foam coated curtain fabrics was 6. The weathering exposure time of the blue wool scale fabric and PU foam coated fabric samples corresponded to 100 hours. The color fastness to artificial weathering of PU foam coated fabrics in the three coating layers were obtained above 6. Consequently, the low filler content, soft binder ratio and foam density had a positive effect on the mechanical, air permeability, color fastness to artificial light, color fastness to artificial weathering and light transmittance properties of foam coated fabrics.

1. INTRODUCTION

The coating is used for technical textile production to achieve functional properties to fabrics [1]. The foam application process can be classified into direct and indirect systems. The main advantages of coating process are lower water, and chemical consumption, besides savings in energy costs [2]. In this process, the uniform foam is applied to the fabric with the foam under pressure.

The foam coating is balanced with the aid of additives. It is applied to one side of the fabric. The foam coated fabric is finally calendered under low pressure. The foam coated fabrics are used as the production of curtain covering in home textiles. The sun-protective properties of curtain fabrics are due to material parameters, weaving and coating processes. Because of curtain fabrics produced from polyester have significant mechanical performance, polyester has been used as the most popular fibre for the production of curtain covering in home textiles. The features of 100% polyester fabrics include non-allergenic, high strength, ease of use, fast drying and very good wrinkle-free properties. Besides, they are used as curtains due to their very good resistance to light.

Foam is described as a viscous material that is too stable but its penetration into the fabric is poor [3-4]. The foam coating technology has significant properties. These properties can be described as the foaming degree, foam stability, viscosity, wetting power and bubble size. Besides new technology has improved the coated-fabric physical

To cite this article: Koruyucu A, Kartal G. 2024. Improvement of mechanical and light transmittance properties of pu foam coated curtain fabrics. *Tekstil ve Konfeksiyon,* 34(3), 261-274.

properties such as tear and breaking strength, elasticity and adhesion.

The black-out foam coating method was beneficial as an unbiased way of assessing the fabric feature. The effectiveness of darkening in the case of woven foam coated fabrics is associated with their geometry and structural parameters.

In the literature, there are different studies on the compatibility of chemicals with fabrics considering in foam coating performance. These studies could be summarized as follows:

Temperature and time affected the dyeing process. The type of dyestuff used and the degradation of dyestuff were adversely affected the environment. Polluted waste water after dyeing contained large amounts of chemicals that had a negative impact on the environment [5].

The ecofriendly and sustainable new foam-coating technology were investigated. In their studies, it was emphasized that the use of less quantities of water, hazardous chemicals and less waste discharge. Also, 30% energy saving in drying was obtained [6,7,8].

The chemical and water consumption were reduced in pigment foam dyeing process with a foam controller [9]. And also, water consumption could be reduced by using foam finishing, counter-flow washing technique and solvent dyeing methods [10].

The suspension properties, foam stability and foam properties were studied [11,12,13]. Hydrolysis degree of foaming agent was affected foam stability [11]. It was used as an environmentally friendly, biodegradable foaming agent along with the sustainable production of keratin hydrolysate [12], [13].

The flame retardancy for cotton fabrics using foamed phosphonium salt precondensates and flame-retardant for PET fabrics using PTFE were used [14,15].

The performance features of different foam applications were investigated [16,17,18,19,20]. The homogeneous distribution of the finishing materials ensured crosslinking with cellulose. As a result, the wrinkle recovery angle was higher than the conventional ones. And also, the foam formation caused strength loss with decrease in density [17,18]. Also, it was stated that the foam finishing was more sustainable, economical and performed well compared to conventional padding [19]. Spider silk protein had been used in foam coating and improved the abrasion behaviour of textile material [20].

In studies [21,22,23,24,25,26], the reasonable mechanical results were achieved through selection of type of foaming agents. Strength properties of polyvinyl alcohol was better than anionic foaming agent [22]. When nano pigments were not used in the coating, the viscosity of the coating was higher [24] Also, the surface viscosity and mechanical strength increased with a more stable structure of the foam [25]. Mechanical and physical properties of encapsulant foams depend on foam cell geometries [26].

In studies [27, 28, 29,30,31], the addition of filling agents improved their mechanical properties. The small size of the calcium carbonate filling particles ensured strong adhesion between the filler and the binder. The low filler concentration of calcium carbonate resulted in positive changes in mechanical and structural characteristics [27]. The modification of filler or matrix components with chemical treatment or coating improved durability performance [28]. It was concluded that kaolin filling agent was chemically, thermally and mechanical stable, inexpensive and low risk as an allergen [29]. And also, the addition of kaolinite significantly improved the heat resistance and mechanical properties [30]. The relationship of the mechanical properties with the foam density and microstructure were studied. That relationship was considering foam cell sizes and also the cell shape [31].

In studies [32,33,34,35], density was an important parameter that influences the properties and performance of rigid polyurethane foam. Lower density was related to the effect of bubbles during foam-laying and the reduction in surface tension of the foamed-fiber dispersion [32]. It was found that the mechanical properties of rigid polyurethane foams changed with the foam density [33]. Also, the polyurethane foam density directly affected its cell structure. The tensile, tear strength, the elongation at break and the adhesive strength linearly increased with the increase of density [34]. As a final conclusion, the most significant parameters on mechanical properties in rigid PUR foams were the foam density, the temperature and material orientation [35].

In studies [36,37], the biodegradable polyurethane samples and the polyols were synthesized. The mechanical and optical properties of the PU coatings prepared were characterized [36]. And also, the density, rheology index, flexural strength, flexural modulus and compressive strength of rigid polyurethane foam increased with NCO/OH ratios [37].

The binder used in the recipe was provided the adhesion of the fibers in the fabric. And also, this situation was increased the air permeability [38]. The chemical polymeric binder was reduced air permeability and thus ensured ease of use [38].

In studies [39,40,41], the light transmission of PU foam coated fabrics were performed with the digital image analysis method. As a conclusion, the light barrier features of PU foam coated fabrics were linked to both fabric construction parameters and fabric porosity [41]. The pores in the fabric structure were closed by polymer coating [42]. Thus, light transmittance of foam coated fabrics were decreased.

The aim of this study was to assess the mechanical performance, air permeability, color fastness to artificial light and light transmittance properties of PU foam coated curtain fabric samples.

In the literature, studies generally focused on the compatibility of chemicals with fabrics in foam coating performance. In this work, unlike the literature, it was aimed to important parameters of the foam coating and PU foam was used in order to give the mechanical, air permeability, color fastness to artificial light, color fastness to artificial weathering and light transmittance properties to produced from 100% polyester fabric. The important parameters were soft: hard binder ratio, kaolin filling agent amount, foam density, coat layer viscosity and fixing temperature for the foam coating method. Commonly used chemicals were selected for foam coating method, thus focusing only on optimum production conditions for PU foam coated curtain fabric properties. The color fastness to artificial light, air permeability, light barrier and mechanical properties of the PU foam coated curtain fabrics were evaluated through a spectrophotometer according to ISO and DIN EN test method.

2. MATERIALS AND METHOD

2.1. MATERIALS

100% polyester woven fabric was used for this study due to its wide usage in home textiles. Properties of woven fabrics were given in Table 1. The polyester fabric had a unit weight of 165 g/m^2.

Table 1. Properties of woven fabric

Property	Warp	Weft
Raw material	Polyester	
Density (1/cm)	28	16
Fabric structure	Plain weave	

Coating chemicals of; binder, foaming agent, cross-linking, fixation agent, synthetic thickener, pigment dyestuffs, filling agent were used and their properties were indicated in Table 2.

Table 2. Properties of coating chemicals

Chemical	Property
Binder	Polyurethane binder, anionic/nonionic
Foaming agent	Hydrocarbons, alkyl amine oxides, amphoteric
Cross-linking	Aromatic blocked isocyanate, non-ionic
Fixation agent	The butanone oxime-free blocked isocyanate-based crosslinking agent, anionic
Synthetic thickener	polyurethane, nonionic
Filling agent	Kaolin
Pigment colorants	

The filler characteristic determines many of the mechanical and light transmittance properties of foam coated textiles.

The particle size, dispersion degree and filler content were determined to affect foam coated fabric properties.

In this study, three layers of foam coating was applied to the surface of 100% polyester woven fabric. It was produced in 1st layer of coating white, 2nd layer of coating black and 3rd layer of white. There was a crosslinker in the final (3rd) layer. In the second layer, black pigment colorant was used. The first layer was white so that the coating could reflect sunlight. The black pigment colorant in the second layer was used to significantly reduce the light transmittance. The crosslinker in the last layer coating was used to improve the breaking, tear and breaking elongation and also weathering resistance of the coated fabric.

In foam coatings, stable foam application was applied to curtain fabric samples with a knife over roller application system. The soft and hard polyurethane binder ratio of 1:1 (50:50) was used as a reference and varied in 66.5:33.5. The gap between the knife and the fabric controlled the application of foam. The coating thicknesses were 1.5 mm, 1.7 mm and 1.9 mm, respectively. The foam density changed between 197-292 g/cm^3. All the curtain fabric samples were dried at 125° C for 2 minutes to prevent cracking on the surface after coating. After that the coated fabric samples were cured at 165° C for 2 minutes. After three coating layer, the foam form is crushed with calender and the fabric surface is smoothened.

2.2. METHOD

In this study, the light transmittance and mechanical properties of the polyurethane foam coated curtain fabrics were evaluated.

The light transmittance properties of foam coated fabrics according to DIN EN 13758-1 test method was evaluated using a UV/VIS spectrophotometer. The light transmittance properties were determined within the wavelength range of 400-700 nm. Based on the experimental results, the transmittance level assessed was 0-2%. It could determine that there was very good protection against UV-Visible light by each curtain fabric samples.

PU foam coated fabrics should block the UV-VIS light. To evaluate the light transmittance properties of foam coated fabrics, a spectrophotometric measurement was used. This method was evaluated the light transmittance properties of foam coated fabrics.

ISO test methods 13937-2, 13934-1 were used for tear strength, breaking force and elongation of woven textile fabrics, respectively. All fabric samples were taken into consideration in the warp and weft directions. For mechanical tests (breaking, tearing strength and breaking elongation) as well as foam density and soft:hard binder ratio, three readings were obtained and the average was used for analysis. The microstructure of polyurethane foam

was characterized with a scanning electron microscope (SEM).

Air permeability of coated fabrics according to TS 391 EN ISO 9237 test standard through the 5 cm^2 test area at 50 Pa pressure in l/m^2/s was measured.

Color fastness to artificial light test with xenon arc fading lamp of PU foam coated curtain fabrics were evaluated according to ISO 105-B02 test method. This test method determined the fading degree of PU foam coated curtain fabrics. Additionally, PU foam coated polyester fabrics were exposed to artificial light with 78 hours.

Color fastness to artificial weathering test with xenon arc fading lamp of PU foam coated curtain fabrics were evaluated according to ISO 105-B04 test method. Color

fastness was evaluated by comparing the color change in the fabric samples with the blue wool reference.

For foam coating method, foam density (low, medium and high), two different binder ratio (soft/rigid), two different amount of kaolin filling agent and coating thickness were determined as the independent variables and 256 different fabrics were prepared with 2^8 factorial experimental design.

For this method, fabric properties were kept constant. The fabric samples were cut to 30x35 cm dimensions according to the width and length of the machine. The foam coating recipes were shown in Table 3.

Table 3. The foam coating recipes

	Parameters	1st layer	2nd layer	3rd layer
Recipe 1 (Foam coating method)	Foam density (g/cm^3)	244	244	244
	Soft: Hard Binder Ratio	50:50	50:50	50:50
	Fixing Temperature (℃)		165℃ for 2 minutes	
	Coating thickness (mm)	1.5	1.7	1.9
	Foam coating viscosity(cps)	1530	1565	1590
Recipe 2 (Foam coating method)	Foam density (g/cm^3)	229	232	236
	Soft: Hard Binder Ratio	50:50	50:50	50:50
	Fixing Temperature (℃)		165℃ for 2 minutes	
	Coating thickness (mm)	1.5	1.7	1.9
	Foam coating viscosity(cps)	1530	1565	1590
Recipe 3 (Foam coating method)	Foam density (g/cm^3)	197	210	210
	Soft: Hard Binder Ratio	50:50	50:50	50:50
	Fixing Temperature (℃)		165℃ for 2 minutes	
	Coating thickness (mm)	1.5	1.7	1.9
	Foam coating viscosity(cps)	1530	1565	1590
Recipe 4 (Foam coating method)	Foam density (g/cm^3)	292	292	292
	Soft: Hard Binder Ratio	66.5:33.5	66.5:33.5	66.5:33.5
	Fixing Temperature (℃)		165℃ for 2 minutes	
	Coating thickness (mm)	1.5	1.7	1.9
	Foam coating viscosity(cps)	1530	1565	1590
Recipe 5 (Foam coating method)	Foam density (g/cm^3)	280	286	286
	Soft: Hard Binder Ratio	66.5:33.5	66.5:33.5	66.5:33.5
	Fixing Temperature (℃)		165℃ for 2 minutes	
	Coating thickness (mm)	1.5	1.7	1.9
	Foam coating viscosity(cps)	1530	1565	1590

3. RESULTS AND DISCUSSIONS

3.1. Mechanical Properties

3.1.1. The effect of foam density, the amount of soft binder and filling agent on breaking strength

Figure 1 illustrated the effect of foam density, the soft: hard binder ratio and filling agent on breaking strength of foam coated curtain fabric samples. The tensile strength of a fabric, which is its resistance when a load is applied in the warp and weft direction, is affected to some extent by the construction or every property of the coating with crosslinker. In this study, the tensile strength correlated with the foam densities. In the 1st and 2nd coating application (recipe 1 and recipe 2), the foam density was medium. The breaking strength decreased with medium foam density due to decrease in the cell-wall thickness. As the foam density increased, the cell size and cell structure of the polyurethane foam decreased. In fact, it did not form the uniform cell structure. The results showed that the toughness increased with the increased foam density. Also the breaking strength increased with the increased foam density. Soft: hard binder ratio was 1:1 in the 1st, 2nd and 3rd coating layers.

The crosslinker in the 3rd layer of coating recipes was used to improve mechanical properties of foam coated fabric samples. The results showed that at the standard 50:50 soft:hard binder ratio, the breaking strength was 1009 N. This result significantly increased up to 1160 N when the soft:hard binder ratio was to 66.5:33.5. This means the breaking strength of the PU foam coated fabric samples was enhanced 15% on the warp direction and 3% on the weft direction when the soft binder amount was increased 33% in recipe 4.

Although the coating recipes generally increased the breaking strength values, it was concluded that 66.5:33.5 soft:hard binder ratio had a positive effect on breaking strength value in recipe 4.

Breaking strength for the foam specimens as function of density was increased. At the same time, crosslinking affected the structure and mechanical properties.

The relative effect depends on the soft:hard binder ratio.

3.1.2. The effect of foam density, the amount of soft binder and filling agent on tearing strength

The foam coating process applied to fabric is an important factor in the tear strength of the fabric. As the process applied to the fabric prevents the movement of the yarn groups all together, the fabric tears more easily. In the coated fabrics, tear strength was decreased as the movement of the threads was increased. The tearing strength of foam coated fabric samples was given in Figure 2.
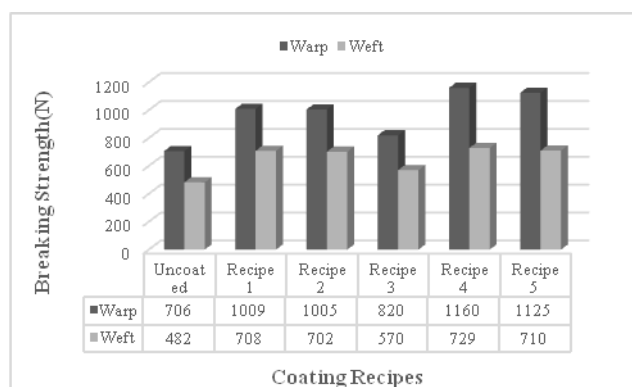

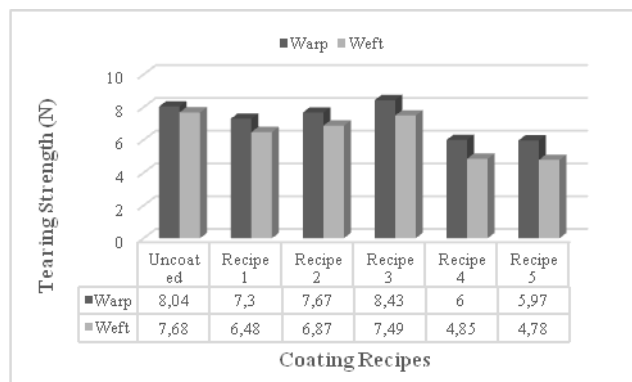**Figure 1.** The diagram of breaking strength in the warp and weft directions

Figure 2. The diagram of tearing strength in the warp and weft directions

As shown in Figure 2, the decrease in tearing strength was observed when compared to the reference. Tear strength of woven fabrics depends on many factors such as fiber, yarn, fabric properties and coating processes applied to the fabric. Therefore, different results can be obtained after coating.

However, according to the results of PU foam coated fabrics, tear strength values decreased when compared to uncoated fabric. Foam density and the amount of kaolin filling agent had a negative effect on tear strength results.

The foam density and the amount of soft binder affected the tearing strength of foam coated fabric samples.

The tear strength decreased under the high foam density condition. The tear strength could reach up to 6.0 N/mm and the foam density was about 292 g/cm^3.

The 50:50 soft: hard binder ratio had a tearing strength of 7.30 N in the warp direction. The least tearing strength recorded was 5.97 N in the warp direction. It could be concluded that the tearing strength of the PU foam coated fabric samples reduced with increased foam density.

From the results, it could be observed that the tearing strength increased from 7.30 N up to 7.67 N at 50:50 soft:hard binder ratio and 244 g/cm^3 medium foam density. It decreased from 6 N up to 5.97 N at 66.5:33.5 soft:hard binder ratio and the high foam density was 292 and 286 g/cm^3, respectively.

This tearing strength of foam coated fabric samples significantly decreased to 6 N when the soft:hard binder ratio was to 66.5:33.5. This means the tearing strength of the PU foam coated fabric samples decreased 25.37% when the soft binder amount was increased 33%.

3.1.3. The effect of foam density, the amount of soft binder and filling agent on breaking elongation

In the tests, PU foam coated 100% PES fabric samples had minimum breaking elongation values at recipe 3. The foam coated fabric samples had more elongation in the warp direction. These elongations could be associated with the low foam density and the 50:50 soft:hard binder ratio.

Cross-linking occurred between the chemical substance molecules in the coating recipes. However, the cohesion force between the molecules caused deformation.

Elongation in the warp direction was greater than that of the weft direction. On the other hand, in the breaking strength test, the foam coated 100% PES woven fabric samples had the lowest elongation.

A maximum elongation could occur as a result of the minimum cohesion force between the chemical substance molecules in the coating recipes.

From the results, it could be observed that the breaking elongation increased from 37.77 % at coating recipe 5 up to 38.95 % at recipe 4. In coating recipes 5 and 4, the soft:hard PU binder ratio was prepared at 66.5:33.5. The least breaking elongation obtained was 29.65 % in warp direction and 50:50 soft:hard binder ratio at recipe 3.

When recipe 1, recipe 2 and recipe 3 were investigated, it was observed that the coating recipes had affected results negatively. The movement of weft and warp yarns under the break elongation load caused a decrease with the effect of the 50:50 and 66.5:33.5 soft: hard binder ratio.

Breaking elongation values increased with increasing foam density in coating recipes 4 and 5.

The highest breaking elongation (%) recorded was 38.95 at coating recipe 4 in the warp direction. It could be concluded that the breaking elongation (%) of the PU foam increased with increasing foam density and soft: hard binder ratio.

Breaking elongation for the foam coated specimens were increased with increasing foam density.

3.1.4. The effect of soft:hard binder ratio and foam density on cracking

In woven fabrics, the surfaces of the weft and warp threads covered with kaolin filling material and the coated fabric had gain a fuller attitude.
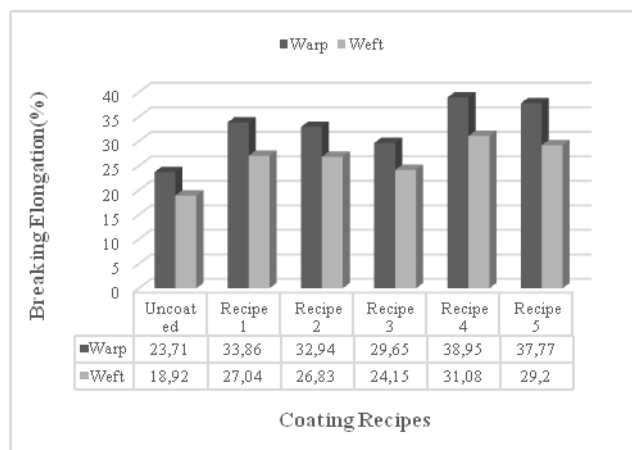

Figure 3. The diagram of percentage of elongation in the warp and weft directions

	Uncoated	Recipe 1	Recipe 2	Recipe 3	Recipe 4	Recipe 5
■Warp	23,71	33,86	32,94	29,65	38,95	37,77
■Weft	18,92	27,04	26,83	24,15	31,08	29,2

Because of the fact that the fabric samples coated with 50:50 soft:hard binder ratio coating recipe were hard handle, cracking was occurred on the coating surface. As the foam density of the coating recipe was decreased, cracking was observed on the recipe 3 coating surface. In this recipe, foam density was decreased due to the formation of weakest links such as allophonate.

In the coating recipes, the viscosity difference in each coating layer was expressed as the cohesion force between the coating chemicals. At the same time, the amount of cracking on the coating surface also depended on the viscosity in the coating recipes.

There was a difference in viscosity due to the difference in the content of coating chemicals.

In addition, as the viscosity was increased, the cohesive force interacting between the coating chemicals also increased.

PU polymer was created a bond with kaolin filler in the coating recipe.

The polymer has formed a bond with the filling agent. However, it was observed that the polymer did not have a significant effect on the cracking behavior. In addition, the water absorbed by the polymers evaporated during drying, causing crack formation on the coating surface. The SEM images obtained from 50:50 soft: hard PU binder ratio samples after drying were presented in Figure 4.

This was because it is necessary to use the crosslinker to bond the PU binder with the kaolin filler.

Due to the high adhesion in fabric samples coated with high PU foam density, no cracking occurred on the surface of the coated fabric samples. In addition, when the soft: hard binder ratio was increased in the coating recipes, the high adhesion was provided in the PU foam coated fabric samples.
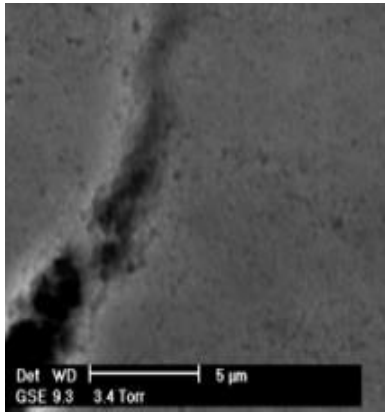
Figure 4. SEM views of the cracking obtained from 50:50 soft: hard PU binder samples after drying

Kaolin content in coating recipes affected mechanical properties of PU foam coated fabric samples. Increasing kaolin content in coating recipes, increased the PU foam coating density.

On the other hand, cracking in the coating surface would result in increased light transmittance.

3.2. The effect of each layer of coating on the light transmittance

In many cases, filling agent and pigment were used to modify the properties of the polymer structures [43].

In this study, the light transmittance properties of each layer of 100% polyester curtain fabric samples coated with polyurethane foam were evaluated. Transmittance measurements were evaluated at every 40 nm. The arithmetic calculated light transmittance values were in the range of 420-700 nm. The light transmittance properties of PU foam coated fabric samples were presented in Figure 5 and in Figure 6. The light transmission of foam coated fabric samples did not exceed 2%.

In this study, two types of recipes were used. Hard and soft PU binder ratios were used equally in the coating recipes 1, 2 and 3. In the coating recipes 4 and 5, the amount of soft binder was increased 33%. In the PU foam coating process, each layer coating application had a certain viscosity.

As the foam density was increased, the light transmittance reduced significantly due to the small pores on the surface of the coated fabric samples.

The low amount of kaolin filling agent in the coating recipe 1 and 2 decreased the light transmittance of foam coated fabric samples. However, the foam density was kept at a medium level in the coating recipe 1 and recipe 2. The low amount of kaolin in the coating recipe 1 and recipe 2 provided an advantage the light transmittance of the foam coated fabric samples, as presented in Figures 5 and 5a.
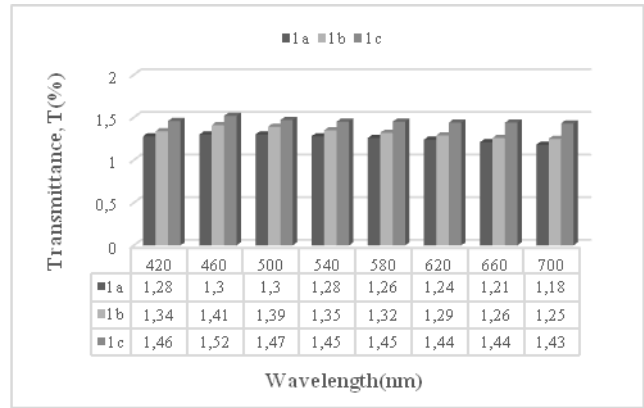

Figure 5. Spectral transmittance T (%) of foam coated fabrics at 420-700 wavelength λ (coating recipe 1) 1a (3rd layer), 1b (2nd layer), 1c (1st layer)

At the same time, when foam density was increased as seen in Figure 5a, the light transmittance of foam coated fabric samples decreased. In recipe 2, the foam density was 236 g/cm^3.
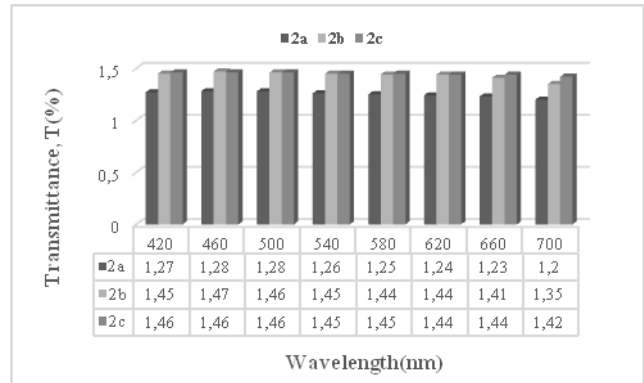

Figure 5a. Spectral transmittance T (%) of foam coated fabrics at 420-700 wavelength λ (coating recipe 2) 2a (3rd layer), 2b (2nd layer), 2c (1st layer)

However, the soft: hard binder ratio was 50:50 in recipes 1, 2 and 3. The amount of kaolin in the recipe 1 and 2 was 150 gram. The foam density was 244 g/cm^3 and 236 g/ cm^3, respectively. It was kept at a medium level.

After coating with recipe 1, 2 and 3, the fabric samples were dried at 125℃ for 2 minutes and then fixed at 165℃ for 2 minutes. After the fixation process, calendering process was applied to the coated fabric samples.
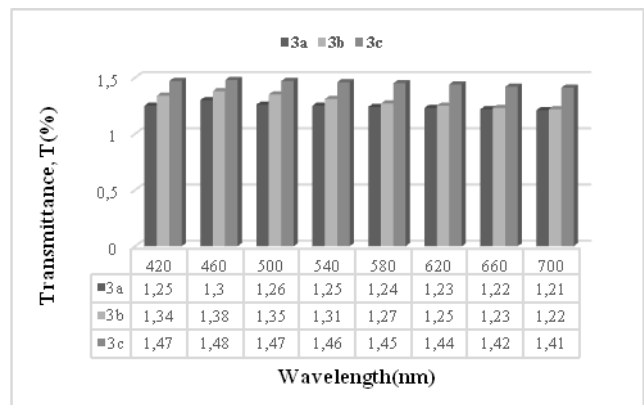

Figure 5b. Spectral transmittance T (%) of foam coated fabrics at 420-700 wavelength λ (coating recipe 3) 3a (3rd layer), 3b (2nd layer), 3c (1st layer)

In recipe 3(3a), low foam density caused less foam cells per unit cross-section. Low foam density had more pores on the fabric surface. That meant less covering. This would lead to a significant increase in light transmittance, as presented in Figure 5b.

Although the foam density was kept at a medium level, it was observed that the amount of kaolin and the drying time were not important.

In this study, the coating application in which soft binder was increased 33% in coating recipe 4 and recipe 5, as indicated in Figure 6 and 6a.

The high amount of kaolin and foam density in the coating recipe 4 was ensured that the light transmittance of the coated fabric sample was minimal. Light transmittance was obtained the least in recipe 4(4a-4b-4c) owing to its chemical structural and good adhesion features of PU foam coated fabric samples. The light barrier property of the fabric sample coated with recipe 4 was the best, as presented in Figure 6.
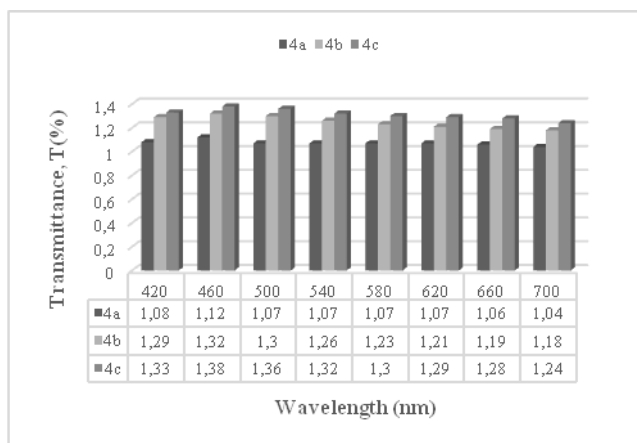

Figure 6. Spectral transmittance T (%) of foam coated fabrics at 420-700 wavelength λ (coating recipe 4) 4a (3rd layer), 4b (2nd layer), 4c (1st layer)
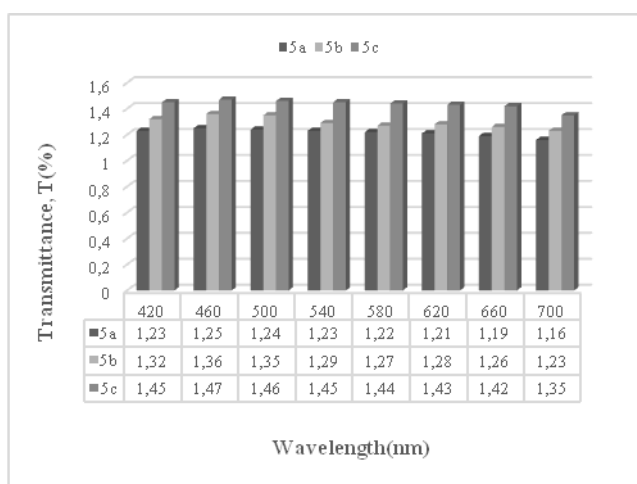

Figure 6a. Spectral transmittance T (%) of foam coated fabrics at 420-700 wavelength λ (coating recipe 5) 5a (3rd layer), 5b (2nd layer), 5c (1st layer)

The effect of the coating recipes on the light transmittance showed a significant change among the 420-700 nm wavelengths. In this wavelength range, the lowest light transmittance was obtained in recipe 4 and the highest light transmission was obtained in recipe 3. As could be seen from Figure 6b, the mostly effective light barrier feature was obtained after coating recipe 4 application.
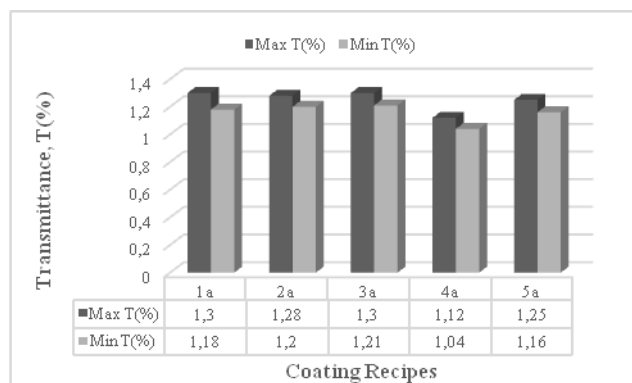

Figure 6b. Spectral transmittance T (%) of PU foam coated fabrics 1a (recipe 1), 2a (recipe 2), 3a (recipe 3), 4a (recipe 4), 5a (recipe 5)

3.3. Air Permeability of PU Foam Coated Curtain Fabrics

Air permeability properties of the coated fabric samples were analyzed. This test method is for measuring the permeability of fabrics to air and is applicable to industrial fabrics that are permeable to air. It was observed that the PU foam coating recipes significantly reduced the air permeability values. As a result, the air permeability analysis of PES fabrics, it was revealed that the coating recipes had a primary effect. The air permeability values in coated PES fabrics decreased by 100% in coating recipe 4. Air permeability, which measures the fabric's ability to allow air to pass through has direct relationship with pore size. An increase in pore size led to an increase in air permeability. The higher air permeability values also gave better barrier to air penetration. The air permeability of coated fabrics were very low. In this study, PU foam coated fabrics air permeability values in the range of 0-2 l/m^2 /s , whereas untreated polyester fabric shows air permeability value of 17.36 l/m^2 /s. Maximum air permeability was obtained in coating recipe 4. Fabric air permeability measurement results were given in Table 4.

The air permeability of PU foam coated fabrics showed 88.47 % decrease in recipe 3 and 100 % decrease in recipe 4 compared to the air permeability of the uncoated PES fabric (Table 4). In woven fabrics, the air flow passes vertically through the gaps between the warp and weft yarns. And also, the coating process reduced the porosity of the fabric. Coating of polyester fabrics led to a decrease in air permeability values. The coating material covered the pores of the untreated fabric and restricted air permeability. As a consequence, air permeability of PU foam coated

fabrics decreased significantly due to greater PU foam adhesion to the textile material.

Table 4. Fabric air permeability measurement results

Coated Fabric Samples	Air Permeability (l/m² /s)	Air Permeability Change (%)
K0 (uncoated fabric)	17.36	-
K1(1a)(recipe 1)	1	94.24
K2 (2a)(recipe 2)	0.66	96.19
K3 (3a) (recipe 3)	2	88.47
K4 (4a) (recipe 4)	0	100
K5 (5a)(recipe 5)	0.33	98.09

3.4. Evaluation of Color Fastness to Artificial Light of PU Foam Coated Curtain Fabrics

Color fastness to artificial light test with xenon arc fading lamp of PU foam coated curtain fabrics were assessed according to ISO 105-B02 test method. Color fastness is the degree to which a colourant resists fading due to light exposure. Fading is related to factors such as the light, proportion of UV and humidity. In this test, samples were exposed to approximately 5 times more energy than normal daylight. This test method was determined textile materials fading degree. The fading degree of number 1 blue wool scale fabric is the worst, while the fading degree of number 8 blue wool scale fabric is the best. The difference between the part exposed to light and the parts not exposed to light at number 6 of the blue wool scale continued until 4 was obtained. In this test, the exposure time of the blue wool scale fabric and PU foam coated fabric samples corresponded to 78 hours. In addition, blue wool fabric scale 4 faded up to grey scale 4. This fading expressed as grey scale grade 4. The main factors that affect the fading of color are: light, light source, intensity, duration of effect, chemical structure of the coating, type of fiber, environment, atmospheric conditions, humidity and temperature. The color fastness to artificial light test results of five PU foam coated polyester fabrics were shown in Table 5 and Figure 7.

The minimum color fastness to artificial light value required for 100 % polyester fabrics was 4 according to standard ISO 105 B02.

At the same time, this test method determined the fading degree of PU foam coated curtain fabrics. PU foam coated PES fabrics were exposed to Xenon arc fading lamp for 78 hours of exposure. As seen in Table 5 and Figure 7, the color fastness to artificial light of PU foam coated fabrics in the three coating layers were obtained above 6. In other words, the color change degree of polyurethane foam coated fabric samples were above 6. In general, the color fastness to artificial light of the PU foam coated fabric samples were very good. Exposure of PU foam coated fabrics to artificial sunlight affected the performance and

behavior of functional apparel. In this study, the color fastness to artificial light process had no effect on the surface changes of the PU foam coated fabrics. Consequently, the color fastness to artificial light with xenon arc fading lamp did not affect the appearance and fading degree.

Table 5. The color fastness to artificial light test results of PU foam coated polyester fabrics

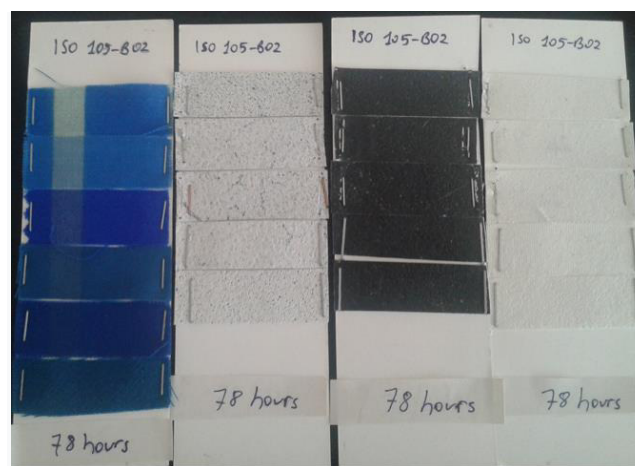| Coated Fabric Samples	Color Fastness to Artificial Light (according to ISO 105-B02 test method)		
	1st layer	2nd layer	3rd layer
K0 (uncoated fabric)	4 (shade change)		
K1(1a)(recipe 1)	6+	6+	6+
K2(2a)(recipe 2)	6+	6+	6+
K3(3a)(recipe 3)	6+	6+	6+
K4(4a)(recipe 4)	6+	6+	6+
K5(5a)(recipe 5)	6+	6+	6+

Figure 7. The color fastness to artificial light test results according to ISO 105-B02 test method: (a). blue wool reference fabric samples, (b).3rd layer PU foam coated fabric samples, (c). 2nd layer PU foam coated fabric samples, (d). 1st layer PU foam coated fabric samples, respectively.

3.5. Evaluation of Color Fastness to Artificial Weathering of PU Foam Coated Curtain Fabrics

In this test, fabric samples coated with PU foam were sprayed with water and exposed to light with a xenon arc lamp under certain conditions. At the same time, 6 blue wool references were exposed to light, protected from the sprayed water by a window glass. Fastness evaluation was evaluated by comparing the color change in the fabric samples with the blue wool reference. A glass filter was placed between the xenon arc lamp and the sample and blue wool references for uniform reduction of ultraviolet rays. The light transmittance of this glass filter should be 0% between 290 nm and 300 nm, and at least 90% between 380 nm-750 nm. As seen in Table 6 and Figure 8, the color fastness to artificial weathering of PU foam coated fabrics in the three coating layers were obtained above 6. The test samples and blue wool references were exposed to weather

conditions until the contrast between the unexposed and exposed parts of reference 6 was equal to 4 on the grey scale. In this test, the weathering exposure time of the blue wool scale fabric and PU foam coated fabric samples corresponded to 100 hours. The reference number showing the contrast closest to the contrast in the test sample expressed the color fastness value. The color fastness to artificial weathering test results of five PU foam coated polyester fabrics were shown in Table 6 and Figure 8.

Table 6. The color fastness to artificial weathering test results of PU foam coated polyester fabrics

Coated Fabric Samples	Color Fastness to Artificial Weathering (according to ISO 105-B04 test method)		
	1st layer	2nd layer	3rd layer
K0 (uncoated fabric)	4 (shade change)		
K1(1a)(recipe 1)	6+	6+	6+
K2(2a)(recipe 2)	6+	6+	6+
K3(3a)(recipe 3)	6+	6+	6+
K4(4a)(recipe 4)	6+	6+	6+
K5(5a)(recipe 5)	6+	6+	6+

As indicated in Table 6 and Figure 8, the color fastness to artificial weathering of PU foam coated fabrics in the three coating layers were obtained above 6. In other words, the color change degree of polyurethane foam coated fabric samples were above 6. In this study, the color fastness to artificial weathering process had no effect on the surface changes of the PU foam coated fabrics.
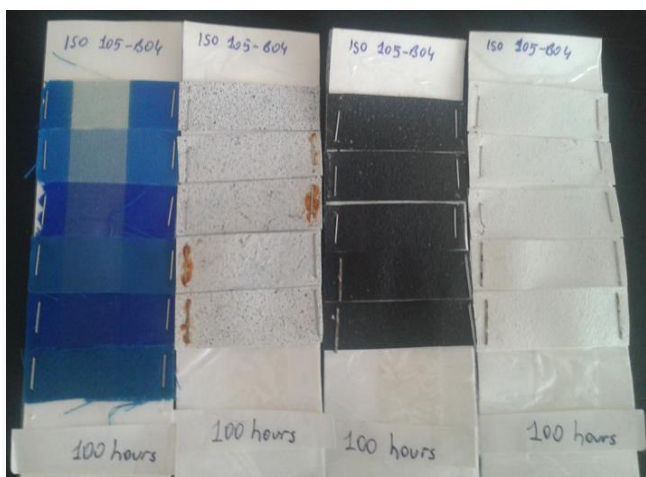

Figure 8. The color fastness to artificial weathering test results according to ISO 105-B04 test method: (a). blue wool reference fabric samples, (b).3 rd layer PU foam coated fabric samples, (c). 2nd layer PU foam coated fabric samples, (d). 1st layer PU foam coated fabric samples, respectively.

3.6. Statistical Analysis

The resulting model is statistically significant at $\alpha=0.05$ with R=0.95 and $R^2=0.9025$. The significant factors were coating recipes.

In this study, the effect of the coating recipes used on the breaking, elongation, tearing strength values in the warp and weft directions were determined by performing a one-way analysis of variance in the SPSS statistical program and the results were given in Table 7-12. The effect of the coating recipes used on the light transmittance in the wavelength range of 400-700 nm were determined by performing a one-way analysis of variance in the spss statistical program and the results were presented in Table 13-20. As seen in Table 13-20, the lowest light transmittance values were acquired at coating recipe 4. As a consequence, the most effective light barrier feature was obtained after coating recipe 4 application, as presented in Table 13-20 and Figure 6b. As seen in Table 7-8 and Table 11-12, the highest breaking strength and breaking elongation values were acquired at recipe 4 in both warp and weft directions. The least tensile strength and elongation values were acquired at recipe 3. Conversely, the lowest tear strength values were acquired at recipe 5, as presented in Table 9-10.

Breaking Strength

Warp and weft directions

Tables 7-20, in which the results of Kruskal Wallis test for mechanical performance and light transmittance are summarised, shown as, df- the degrees of freedom of the test, Asymp.Sig(p).-the statistical significance level, N-sample number.

Table 7. Ranks

Result	Recipe	N	Mean Rank
	Raw fabric	3	2.00
	Recipe 1	3	10.67
	Recipe 2	3	8.33
Warp	Recipe 3	3	5.00
	Recipe 4	3	17.00
	Recipe 5	3	14.00
	Total	18	
	Raw fabric	3	2.00
	Recipe 1	3	13.67
	Recipe 2	3	10.00
Weft	Recipe 3	3	5.00
	Recipe 4	3	17.00
	Recipe 5	3	9.33
	Total	18	

Table 8. Test Statistics

		Result
	Qi-Square [a]	16.392
Warp	df	5
	Asymp.Sig.	0.006
	Qi-Square [a]	15.830
Weft	df	5
	Asymp.Sig.	0.007

Tearing Strength

Warp and weft directions

Table 9. Ranks

Result	Recipe	N	Mean Rank
Warp	Raw fabric	3	14.00
	Recipe 1	3	8.00
	Recipe 2	3	11.00
	Recipe 3	3	17.00
	Recipe 4	3	4.33
	Recipe 5	3	2.67
	Total	18	
Weft	Raw fabric	3	15.00
	Recipe 1	3	8.00
	Recipe 2	3	11.00
	Recipe 3	3	16.00
	Recipe 4	3	5.00
	Recipe 5	3	2.00
	Total	18	

Table 10. Test Statistics

		Result
Warp	Qi-Square [a]	16.251
	df	5
	Asymp.Sig.	0.006
Weft	Qi-Square [a]	16.175
	df	5
	Asymp.Sig.	0.006

Breaking Elongation

Warp and weft directions

Table 11. Ranks

Result	Recipe	N	Mean Rank
Warp	Raw fabric	3	2.00
	Recipe 1	3	11.00
	Recipe 2	3	8.00
	Recipe 3	3	5.00
	Recipe 4	3	17.00
	Recipe 5	3	14.00
	Total	18	
Weft	Raw fabric	3	2.00
	Recipe 1	3	11.00
	Recipe 2	3	8.00
	Recipe 3	3	5.00
	Recipe 4	3	17.00
	Recipe 5	3	14.00
	Total	18	

Table 12. Test Statistics

		Result
Warp	Qi-Square [a]	16.579
	df	5
	Asymp.Sig.	0.005
Weft	Qi-Square [a]	16.579
	df	5
	Asymp.Sig.	0.005

Transmittance (%) -Wavelength

In order to verify the level of barrier properties, the light transmittance was determined with a wavelength ranging from 400 to 700 nm. Transmittance measurements were evaluated at every 50 nm in 6 rectangular samples taken from each specific area of the fabric. Asymptotic significances are not illustrated in 400 nm.

Table 13. Ranks

Result	Recipe	N	Mean Rank
450 nm	Recipe 1	3	2.33
	Recipe 2	3	8.00
	Recipe 3	3	5.00
	Recipe 4	3	13.67
	Recipe 5	3	11.00
	Total	15	

Table 14. Test Statistics

	Result
Qi-Square [a]	12.333
df	4
Asymp.Sig.	0.015

Table 15. Ranks

Result	Recipe	N	Mean Rank
500 nm 550 nm 600 nm	Recipe 1	3	2.33
	Recipe 2	3	8.33
	Recipe 3	3	4.67
	Recipe 4	3	13.67
	Recipe 5	3	11.00
	Total	15	

Table 16. Test Statistics

	Result
Qi-Square [a]	12.667
Df	4
Asymp.Sig.	0.013

Table 17. Ranks

Result	Recipe	N	Mean Rank
	Recipe 1	3	2.33
	Recipe 2	3	7.67
650 nm	Recipe 3	3	5.00
	Recipe 4	3	13.33
	Recipe 5	3	11.67
	Total	15	

Table 18. Test Statistics

	Result
Qi-Square [a]	12.467
Df	4
Asymp.Sig.(p)	0.014

a.Kruskal wallis test, b. Grouping variable:recipes

Table 19. Ranks

Result	Recipe	N	Mean Rank
	Recipe 1	3	2.33
	Recipe 2	3	7.00
700 nm	Recipe 3	3	5.67
	Recipe 4	3	13.67
	Recipe 5	3	11.33
	Total	15	

Table 20. Test Statistics

	Result
Qi-Square [a]	12.267
Df	4
Asymp.Sig.(p)	0.015

a.Kruskal wallis test, b. Grouping variable:recipes

Depending on the Table 15-16, it can be seen that, light transmittance (%) had a statistically significant effect (p= 0.013 < 0.05) in recipe 4. Additionally, on the Table 7-8, breaking strength had a statistically significant effect (p= 0.006 < 0.05) in recipe 4 in the warp direction. Polyurethane foam coating had a statistically significant effect (p=0.005<0.05) on the breaking elongation values of the fabric (Table 11-12).

The highest light barrier and the least light barrier values were acquired at recipe 4 and recipe 3, respectively. The low light transmittance was related to the low porosity in the fabric structure. This could be accomplished by the kaolin filler, the soft binder ratio and the high foam density. As the foam density at coating recipes was decreased, cracking was observed at the recipe 3.

Asymptotic significances (2-sided tests) are illustrated. The significance level is 0.05.

4. CONCLUSIONS

In this paper, the breaking strength, elongation, tearing strength, air permeability, color fastness to artificial light, color fastness to artificial weathering and light transmittance properties of PU foam coated curtain fabric samples were investigated. After mechanical, air permeability, color fastness to artificial light, color fastness to artificial weathering and light transmittance tests conclusions can be emphasized. The main results are summarized as follows:

There were significant differences between pairs of breaking strength, elongation and tearing strength through the fabrics in both directions.

The results showed that soft: hard binder ratio significantly affected the mechanical properties of the polyurethane foam coated fabric samples. In order to get good breaking strength, the adhesion property of the binder to the yarn surface should be good. Polyurethane foam coating had showed a good adhesion feature to fabric.

For polyurethane foam coatings, mechanical properties were evaluated as a function of foam density and structure of the foams. The mechanical properties of a cellular foam depend on the polymer material and the cell wall. Important structural properties in tension were foam density and closed foam cell. Due to the small size of the cells, the anisotropy of the mechanical properties of these foams is also lower. The microstructural feature of the cell is related to the microstructure and the foam density.

Foam density is an important parameter that influences the mechanical properties of PU foam coated fabrics. The water and chemical absorption increased with decrease in foam density. Due to increase in the cell size and decrease in the cell-wall thickness.

The penetration effect of the PU foam coating into the fabric caused to decrease of the tear strength of fabric samples. For foam coating method, the foam density significantly changed the breaking strength and optimal conditions were at 292 g/cm^3 and 165℃ with 2 minutes of fixing temperature. As the foam density was increased, the cell size and cell structure of the polyurethane foam decreased.

The low filler concentration resulted in positive changes in mechanical properties due to bonding mechanism between filler, the coating material and the fabric surface. The use of a greater quantity of kaolin filling agent has led to the deterioration of mechanical properties. For that reason, the quantity of kaolin filler should be under 150 g/kg in coating recipe.

The amount of filling agent (kaolin) significantly improved the mechanical properties of coated fabric samples. When the amount of kaolin (filling agent) was increased, cracking was observed on the surface of the PU foam coated fabric

samples after preparing recipe 3 and also, drying at 125°C for 2 min.

The coating material covered the pores of the untreated fabric and restricted air permeability. It was determined that the coating process reduced the air permeability values due to pore size. The air permeability values in PU foam coated PES fabrics decreased 88.47% in recipe 3 and 100 % in recipe 4 compared to the air permeability of the uncoated PES fabric. PU foam coating technique affected the penetration of the coating material into the fabric and had a important effect on the air permeability of the coated fabric. Consequently, air permeability of PU foam coated fabrics decreased significantly due to greater PU foam adhesion to the textile material.

The color change degree of polyurethane foam coated fabric samples were above 6. In general, the color fastness to artificial light of the PU foam coated fabric samples were very good. Exposed to artificial sun light of PU foam coated fabrics affected the behavior of functional apparel. Consequently, the color fastness to artificial light did not affect the appearance and fading degree.

The color fastness to artificial weathering of polyurethane foam coated fabric samples were above 6. In this study, the color fastness to artificial weathering process had no effect on the surface changes of the PU foam coated fabrics. And also, the weathering resistance of PU foam coated curtain fabrics is related to the filling material and foam density.

The low light transmittance is related to the fabric porosity. This can be accomplished by the kaolin filler, the soft binder ratio and the high foam density.

The foam coating was to create barrier properties on the fabric. The light barrier property of PU foam coated fabrics provided comfort sensation.

Due to good mechanical, adhesion and also good light barrier properties, PU foam coated fabrics have used as coating of curtain fabrics.

More detailed studies can be performed by changing the binder ratios and foam density in order to minimum the light transmittance of coated fabric samples.

REFERENCES

1. Bulut Y, Sular V. 2008. General properties and performance pests of fabrics produced by coating and lamination techniques. *Journal of Textile and Engineering,* 15(70), 5-16.

2. Sen A. K. 2007. *Coated Textiles-Principles and Applications*, 2nd edn. CRC Press, Boca Raton, FL, USA, pp. 94-95.

3. Kinnunen-Raudaskoski K., Hjelt T., Kenttä E., Forsström U. 2014. Thin coatings by foam coating. *Tappi Journal*, 13(7), 9-19.

4. Kenttä, E., Koskela, H., Paunonen, S., Kinnunen Raudaskoski, K., Hjelt, T. 2016. Functional surfaces produced by foam coating. *TAPPI J.*,15(8), pp.515-521.

5. Kumar PS, Yaashikaa PR. 2018. Sustainable dyeing techniques, *Sustainable innovations in textile chemical processes.* Springer, Singapore, pp 1–29.

6. Song MS, Hou JB, Lu YH, Lin J, Cheng DH. 2013. Performance of foam and application in foam finishing of textile, *3rd International Conference on Textile Engineering and Materials,* vol 821–822, pp 661–664.

7. Rather L.J, Jameel S, Dar OA, Ganie SA, Bhat KA, Mohammad F. 2019. Advances in the sustainable technologies for water conservation in textile industries., *Water in Textiles and Fashion*. Woodhead Publishing, Sawston, pp 175–194

8. Van der Walt G H J, Van Rensburg N J J. 1986. Low-liquor dyeing and finishing. *Textile Progress*, 14, pp.1–50

9. Chen S, Wang C, Fei L, Liu H. 2017. A novel strategy for realising environmentally friendly pigment foam dyeing using polyoxyethylene ether surfactant. *Color Technol*, 133, pp.253–261.

10. Gopalakrishnan M, Punitha V, Saravanan D. 2019. Water conservation in textile wet processing. *Water in Textiles and Fashion*, Woodhead Publishing, Sawston, pp 135–153.

11. Hou Q, Wang X. 2017. The effect of PVA foaming characteristics on foam forming. *Cellulose*, 24, pp.4939–4948.

12. Bhavsar PS, Zoccola M, Patrucco A, Montarsolo A, Mossotti R, Giansetti M, Rovero G, Maier SS, Muresan A, Tonin C. 2017. Superheated water hydrolyzed keratin: a new application as a foaming agent in foam dyeing of cotton and wool fabrics. *ACS Sustain Chem Eng,* 5, pp.9150–9159.

13. Li K, Zhang, JF, Li QJ. 2011. Study on foaming properties of sodium dodecyl sulfate for textile foam dyeing and finishing. *Advanced Materials Research*. Trans Tech Publication, vol 332–334, pp 1515–1519

14. Gregorian RS, Namboodri CG, Young RE, Baitinger WF. 1983. Foam application of phosphonium salt flame retardants. *Textile Research Journal*, 53, pp.148–152

15. Ashrafi, F., Lavasani, M.R. 2019. Improvement of the mechanical and thermal properties of polyester nonwoven fabrics by PTFE coating. *Turkish Journal of Chemistry*, 43: pp.760-765.

16. Wadsworth LC, Wey PS. 1988. Effects of differential foam application of durable press and fluorochemical finishes to cotton fabric. *Journal of Industrial Textiles*, 17, pp.152–166

17. Yang CQ, Perenich TA, Fateley WG. 1989. Studies of foam finished cotton fabrics using FT-IR photoacoustic spectroscopy. *Textile Research Journal*, 59, pp.562–568.

18. Liu Y, Xin JH, Choi CH. 2012. Cotton fabrics with single-faced superhydrophobicity. *Langmuir*, 28, pp.17426–17434

19. Muhammad M.and Shaheen S. 2020. Development of sustainable and cost efficient textile foam-finishing and its comparison with conventional padding. *Cellulose*, 27, pp.4091-4107.

20. Jokisch S, Scheibel T. 2017. Spider silk foam coating of fabric. *Pure Appl Chem,* 89: pp.1769–1776.

21. Lappalainen T., Salminen K., Kinnunen K., Jarvinen M., Mira I., Anderson M. 2014. Foam Forming Revisited. Part II. Effect Of Surfactant on the Properties of Foam-Formed Paper Products. Nord. *Pulp and Paper Research Journal,* 29, pp.689-699.

22. Gottberg J.M., Lappalainen T., Salminen K. 2017. Polyvinyl Alcohol as Foaming Agent in Foam Formed Paper. In Paper Conference and Trade Show; *TAPPI*: Minneapolis.

23. Bunker D., Cecchini J., Hietaniemi M., Virtanen M., Torvinen K., Asikainen J., Salminen, K. 2017. Foam Forming Tecnology Folding Box Board Focused Developments. In Paper Conference and Trade Show, *TAPPI:* Minneapolis, pp.1802.

24. Kentta E., Kumar V., Andersson P., Forsström,U. 2021. A Novel Foam Coating Approach To Produce Abrasive Structures On Textiles. *Autex Research Journal*, 0031, pp.1-8.2021.

25. Hou Q, Wang X. 2018. Effect of fiber surface characteristics on foam properties. *Cellulose*, 25: pp.3315-3325.

26. Goods S. H., Neuschwanger C. L., Henderson C. C., Skala D. 1998. Mechanical properties of CRETE, a polyurethane foam. *Journal of Applied Polymer Science,* vol.68, pp.1045-1055.

27. Mouna S., Walid C., Sondes G., Riadh Z., Visileanu E. and Slah M. 2022. The effect of calcium carbonate content and particle size on the mechanical and morphological properties of a PVC foamed layer used for coated textiles. *Industria Textila*, vol.73, no.5, pp. 580-586.

28. Chang BP, Mohanty AK, Misra M. 2020. Studies on durability of sustainable biobased composites: a review. *Royal Society of Chemistry Advances* ,10(31), pp.17955–17999.

29. Bryant GM. 2016. Dynamic sorption of semistable foams by fabrics: Part I: Implications for textile foam application processes. *Textile Research Journal,* 54, pp.217–226

30. Chen X., Sang X., Zhang Q. 2015. Preparation and characterization of polyurethane-imide/ kaolinite nanocomposite foams. *Royal Society of Chemistry Advances.*, pp. 53211–53219

31. Angel S, Ana MB, Ignacio G, et al. 2017. The Role of microstructure on the mechanical properties of polyurethane foams containing thermoregulating microcapsules [J*]. Polymer Testing*, pp. 274-282.

32. Xiang W., Filpponen I., Saharinen E., Lappalainen T., Salminen K., Rojas O.J. 2018. Foam processing of fibers as a sustainable alternative to wet-laying: fiber web properties and cause- effect relations. *ACS Sustainable Chemistry &Engineering,* 6, pp.14423-14431.

33. Thirumal M., Khastgir D., Singha N.K., Marjunath B.S., Naik Y.P 2008. Effect of foam density on the properties of water blown rigid polyurethane foam. *Journal of Applied Polymer Science*, vol.108, pp.1810-1817.

34. Zheng XG, Li SM, Zeng Z, et al. 2015. Effect of apparent density on mechanical properties of polyurethane foam curing materials[J]. *Chinese Railway Science*, 36 (3), pp. 12-16

35. Linul E, Marsavina L, Voiconi T, et al. 2013. Study of factors influencing the mechanical properties of polyurethane foams under dynamic compression[J*]. Journal of Physics*, 451, pp. 214-2.

36. Zhang J, Tu W, Dai Z. 2012. Synthesis and characterization of transparent and high impact resistance polyurethane coatings based on polyester polyols and isocyanate trimers. *Progress in Organic Coatings,* 75(4), pp.579–583

37. Asefnejad A., Khorasani M., Behnamghader A., Farsadzadein B., Bonakdar S. 2011. Manufacturing of biodegradable polyurethane scaffolds based on polycaprolactone using a phase separation method: physical properties and in vitro assay. *The International Journal of Nanomedicine,* 6, pp. 2375

38. Asker G. and Balcı O. 2022.Investigation of The Effect of Raising and finishing process on the phycysical performance of 3-thread fleece fabric. *Tekstil ve Konfeksiyon*, 32(3), pp.183-192.

39. Szkudlarek J. and Snycerski M. 2017. Structural modelling of blackout fabrics patterned by weave used as a curtain in interior public spaces. *Fibres And Textiles in Eastern Europe,* vol.25,4(124); pp.45-49.

40. Ye X. and Chen D. 2018. Thermal insulation coatings in energy saving. *Energy-Efficient Approaches in Industrial Applications*, pp.1-17.

41. Militky J., Travnickova M., and Bajzik V. 1999. Air permeability and light transmission of weaves. *International Journal of Clothing Science and Technology,* 11(3), pp. 116- 125.

42. Demirbağ Genç S, Alay Aksoy S. 2022. Development of temperature and pH-responsive smart cotton fabrics by P(NIPAM-co-MAM) copolymer finishing. *Tekstil ve Konfeksiyon*, 32(3), pp.193-207.

43. Margolis J. 1958. The kaolin clotting time: a rapid one-stage method for diagnosis of coagulation defects. *Journal of Clinical Pathology,* 11, pp. 406–409.

Dynamic Heat Transfer Simulation in Textile for Practical Application: A Comparative Analysis of Microscopic and Macroscopic Approaches

Elena Codau[1]* [ID] 0000-0002-8261-6727
Teodor-Cezar Codau[2] [ID] 0000-0002-5388-7878
Robert-Madalin Chivu[3] [ID] 0000-0002-3383-5800

[1]Technical University "Gheorghe Asachi" of Iasi, Faculty of Industrial Design and Business Management, Str. Prof. Dr. Doc. Dimitrie Mangeron, No. 28, 700050-Iasi, Romania
[2]University of Minho, Fibrenamics, Campus de Azurém, 4800-058 Guimarães, Portugal
[3]University of Minho, Department of Mechanical Engineering, MEtRICs, Campus de Azurém, 4800-058 Guimarães, Portugal

ABSTRACT

Heat transfer simulation in textile materials has many practical applications, such as in the design of protective clothing for firefighters, the development of thermal insulation materials, and the optimization of temperature control in textiles for comfort and performance. This paper presents a study on heat transfer simulation in woven fabrics using the Comsol Multiphysics® application. The simulations were carried out for both microscopic (3D) and macroscopic (1D) scales and the heat flux variation was compared with experimental results. The steady-state average heat flow through the textile was determined, and this value was used to calculate the thermal resistance of the woven fabrics. The thermal resistance values obtained were within a deviation range of 4.2% to 6.3% from the values determined according to ISO 11092/1016, thus validating the proposed model. For the transient regime, the microscopic approach proved to be more accurate, the estimated time for the heat flow to reach a certain value depending essentially on the scale approached in the modeling. This finding has particular significance in the field of protective clothing, especially for firefighters exposed to radiant heat sources, where estimating the time for burns to occur is crucial.

1. INTRODUCTION

Clothing is the interface between the human body and the environment, with the main role of ensuring the thermal protection of the wearer. The heat-related characteristics of textiles play a crucial role in determining the level of thermal comfort they provide, and, over time, many standard properties have been defined to characterize the heat transfer capacity of textiles. Heat exchange between the human body and environment throughout the clothing system takes place under dynamic conditions and these standardized properties are not sufficient for the characterization of textiles in terms of heat transfer, especially in thermal protective clothing and sportswear during intense physical activity and/or special environmental conditions (e.g., high temperature and thermal radiation). Modeling and simulation are methods that can cover this dynamic behavior issue [1].

Heat transfer simulation in textile materials is an active area of research that aims to understand and optimize the thermal performance of textiles [2]. Overall, heat transfer simulation in textiles is advancing rapidly, providing valuable insights into the thermal performance of textiles and leading to the development of more efficient products [3].

Torvi [4] was the first to develop and validate a significant model for textile heat transfer, specifically for testing fabrics at high temperatures and open flame. The one-dimensional physical model considered the textile material homogeneous and the mathematical equations accounted for heat transfer through conduction and radiation. Mell and Lawson [5] then used the Torvi model but incorporated multilayer textile structures for protective clothing for firefighters. Gibson [6] proposed a model in which the textile material was treated as a hygroscopic porous medium, coupling mass, and heat transfer according to

To cite this article: Codau E, Codau T C, Chivu R M. 2024. Dynamic heat transfer simulation in textile for practical application: a comparative analysis of microscopic and macroscopic approaches. *Tekstil ve Konfeksiyon,* 34(3), 275-282.

Whitaker's theory. The proposed mathematical model accounted or the conservation of momentum and energy as well as the continuity equation. Prasad [7] developed a detailed mathematical model for studying non-stationary heat and moisture transfer through multilayer fabric assemblies, considering the presence of air gaps and the changes in thermodynamic and transport properties due to the presence of water. The model was solved using the Runge-Kutta approximation method and compared favorably to experimental measurements. More recently, Łapka [8] presented a complex mathematical model that accounted for the interaction between protective clothing for firefighters and human skin, incorporating heat transfer through conduction and radiation, as well as the diffusion of water vapor through porous media.

The mathematical models outlined earlier describe the system using global equations that do not consider the thermal interaction between the fluid and solid components within the textile structure. Over the last decade, recent advancements in simulation software have made it possible to reduce the computational resources required for these simulations. Currently, two approaches are highlighted in the simulation of heat and mass through porous materials, depending on the model scale: microscopic or macroscopic. Each of these two model types comes with its working assumptions that directly influence the accuracy of the results and the costs of simulation. However, the comparisons between the values from the macroscopic scale simulation and the experimental results revealed substantial differences in the transitory area (dynamic regime) for temperature, heat flow, etc. [9]. These differences are of particular importance in critical applications such as firefighting interventions, for steel workers exposed to fire and very high temperatures, etc.

In this paper, the Finite Element Method (FEM) has been used to simulate the heat transfer over textiles at the microscopic and macroscopic scales.

2. THEORETICAL CONSIDERATION

Porous materials facilitate heat transfer through two mechanisms: the solid matrix and the fluid in the voids. Heat is transferred through the solid matrix via conduction, while the transfer through the fluid occurs through conduction, convection, and radiation.

Thermal conduction is a process of transferring heat within a thermodynamic system or between systems that are in thermal contact, and it occurs due to direct molecular interactions without involving mass transfer. The equation for conduction heat transfer was derived by Fourier in 1882 and can be expressed as [10]:

$$\frac{\partial T}{\partial t} = \frac{1}{C_p \cdot \rho} \cdot k \cdot \nabla^2 T \tag{1}$$

where: k is thermal conductivity, ρ - density, C_p - thermal capacity, T - temperature, t - time variable, and $\Delta^2 T$ - divergence of gradient temperature (Laplace operator).

Radiation heat transfer occurs through electromagnetic waves and involves wavelengths ranging from 0.1 μm (ultraviolet) to 100 μm (infrared). The relationship between emitted energy and the temperature was established experimentally by Jozef Stefan and theoretically by Ludwig Boltzmann, utilizing the abstract concept of the black body [11]:

$$E_b = \varepsilon \cdot \sigma \cdot T^4 \tag{2}$$

where: E_b is the energy emitted in unit time, per unit area, T - the temperature, σ - Stefan-Boltzmann constant, and ε - the emissivity coefficient.

Radiative heat transfer is a property of the surface that is influenced by temperature, optical properties, and surface orientation. To determine the effect of surface orientation, a *shape factor* was introduced. Although it is impossible to calculate shape factors within the voids of natural porous materials, Song [12] concluded that radiative heat transfer can be disregarded in textiles due to the very small dimensions of the voids between structural components (yarns/fibers).

Convection is the mechanism of heat transfer associated with fluid mass transport. When the flow lines are parallel there is a laminar flow, otherwise, it is a turbulent flow. The law of thermal convection was deduced by Newton and has the form:

$$\frac{\dot{Q}}{S} = h_t \cdot (T_s - T_\infty) \tag{3}$$

where: $\dot{Q}/S$ is heat flow, h_t - the thermal convection coefficient, T_∞ - the bulk fluid temperature, and T_s - the border temperature.

The convection coefficient includes all the factors on which the heat transfer depends on the fluid properties, surface geometry, and flow type [13]. In most cases, this coefficient is impossible to be calculated or experimental determined. For that reason, the similarity and boundary layer theory is necessary.

Free convection is governed by a non-dimensional number called the *Rayleigh number*, *Ra*:

$$Ra = \frac{\rho^2 \cdot g \cdot \beta \cdot C_{p,a}}{\mu_a \cdot k_a} \cdot L_{ch}^3 \cdot \Delta T \tag{4}$$

where: g is gravitational acceleration, β - the coefficient of thermal expansion, ΔT - the difference between surface temperature T_s and bulk temperature T_∞, L_{Ch} - the

characteristic length, v - the kinematic viscosity, μ_a - the dynamic viscosity of air, $C_{p,\,a}$ - the specific heat, and k_a - the thermal conductivity.

In the case of textile structures, calculating the characteristic length can be challenging, but considering a channel that is tangentially confined by the warp and weft yarns, the characteristic length can be substituted with the equivalent hydraulic diameter, d_h [14]:

$$d_h = \frac{4 \cdot A}{C_s} \tag{5}$$

where A is the area of the channel section and C_s is the perimeter of the section.

3. MATERIAL AND METHOD

3.1 Material

All textile materials used in this study are woven fabrics, each with the same composition in the warp and weft systems. The woven fabrics were selected taking into account the importance of these materials in applications such as fire protection clothing.

The thermal conductivity and specific heat capacity were measured with the *Hot disc* technique in compliance with the standard ISO 22007-2/2008. The thermal resistance of the fabrics was determined using the *Sweating guarded hot plate*, in compliance with the standard ISO 11092/2016. Fabric thickness was tested with a *Digital Thickness Gauge* SDL Atlas according to ISO 5084/1996 and for surface weight, an electronic balance was used. The thermal properties of the fabrics determined according to these standards are shown in the first table from the *Results and Discussion* section and are used in the 1D (macroscopic) simulation of heat transfer.

To simulate the heat transfer through textile materials at the microscopic level, the properties of the yarns were performed directly in Comsol® starting from those of the fibers (listed in Table 1) and their composition. The equivalent thermal conductivity of the yarns, k_{ech}, was calculated with the following relation [15]:

$$k_{ech} = \sum \theta_i \cdot k_i + \varepsilon_y \cdot k_{fluid} \tag{6}$$

where k_i, are the thermal conductivity of fibers, Θ_i the volume fraction of fibers, ε_y - the yarn porosity and k_{fluid} - the thermal conductivity of the fluid.

The volume fraction of fibers can be written as:

$$\Theta_i = \frac{\rho_y}{\rho_i} \alpha_i \tag{7}$$

where ρ_i is the density of the fibers, α_i – the mass fraction of fibers (from Table 1), and ρ_y – the density of the yarn.

The density of the yarn was determined from the following equation:

$$\rho_y = \frac{Yarn\ linear\ density}{Yarn\ cross - section\ surface} \tag{8}$$

The porosity of the yarn can be found from the following relation:

$$\sum \theta_i + \varepsilon_y = 1 \tag{9}$$

Table. 1. Fiber properties [16] [17]

Fibers	Density	Thermal conductivity	Heat capacity
	g/m³	W/(m·K)	J/(kg·K)
Nomex®	1380	0.25	1256
Kevlar®	1440	0.04	1420
PBI	1300	0.41	1130
Viscose	1530	0.289	1590
PA-antistatic	1070	0.21	1700

3.2 Method

3.2.1. Heat transfer simulation

The software used in the simulation is Comsol Multiphysics®, which is a cross-platform software that allows the modeling and simulation of physical processes based on FEM [18]. FEM is the most widely used method of solving engineering problems including structural analysis, heat transfer, fluid flow, or mass transport [19]. Comsol Multiphysics® has a large number of modules that allow solving engineering or scientific problems, with the possibility of coupling these modules. Due to the predefined models, the simulation is much easier. The emphasis is on the physical quantities and there is no need to define new equations.

In this paper, Comsol Multiphysics® has been used to simulate the heat transfer in textile structures at the macroscopic and microscopic scales. The macro-scale simulation was performed under the assumption that the fabrics are homogeneous and isotropic materials for which the global properties are obtained by standard methods (Table 2). For the microscopic level simulation, the 3D geometric models and the yarns property were considered. The heat transfer mechanism through the woven fabrics takes place mainly by conduction. A very small order of magnitude of the Rayleigh number obtained directly in Comsol® for fabrics from Table 2 under ISO 11092/2016 conditions, confirms that the thermal convection can be neglected. To estimate Ra, Equation 4 and the air properties stored in the material library were used.

3.2.2. 3D model of the textile structure

To accurately simulate the heat transfer through textiles, a geometric model close to the actual fabric structure is necessary. Ideal yarn is assumed to have a circular cross-sectional shape, but due to the mechanical stress in the weaving process and the interlacing of the yarns, the shape of the cross-section of yarn is flattening. To take into account this effect, Pierce [20] modified his circular model, introducing an elliptical shape. Later, Kemp [21] proposed a new cross-section model, a rectangular geometry with two circular shapes at the ends that is more suitable for jammed configuration. A lenticular geometric cross-section shape was proposed by Hearle, in 1978 [22].

Another aspect to be considered in the geometric model is the yarn path of both the weft and warp systems. The path of the yarns is related to the yarn density (yarns/cm) and cross sections of the yarns from the other system and was described by the same researchers who developed the cross-sectional models. Even if the lenticular geometry is the most widespread cross-section of the yarn in woven fabrics, the path and the cross-section shape depend on many technological factors such as yarn twist, mechanical stress, yarn density, etc.

In order to have a higher accuracy of the 3D model, microscopic analysis was used. Thus, the geometrical parameters of yarns in the fabrics were acquired by using a Magnum Ceti Binocular microscope.

A very clear cross-sectional image of the woven fabric is difficult to obtain. When the fabric is cut, the fibers are withdrawn from the yarn which makes it difficult to obtain a clear and real cross-section. To avoid this problem the fabrics were coated before cutting with an acrylic binder without applying pressure. For example, Figure 1 shows the cross-sectional image of S1 and S2 fabrics. The yarns of the S1 structure (Figure 1a) have a lenticular cross-section, while S2 (Figure 1b) have elliptical cross-section yarns.
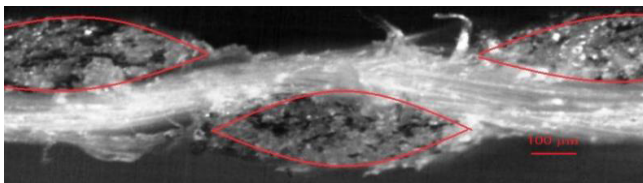
a)   S1-lenticular cross-section yarns
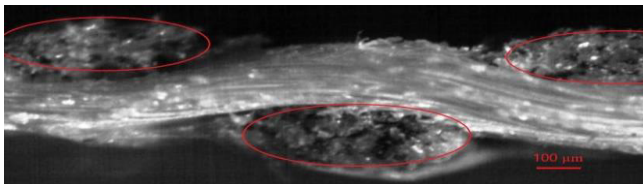
b)   S2- elliptical cross-section yarns

Figure 1. Micrograph cross-section of woven fabrics

The geometric parameters were obtained by processing the images by ImageJ software [23]. The parameters have been used to design the geometric model of the textile structure for each woven fabric in TexGen®.

TexGen® is an open-source software under the General Public License developed at the University of Nottingham for modeling textile structures [24]. To generate each yarn in TexGen® it was used a two-dimensional shape that swept along a path. The cross-section of yarns can be defined as an ellipse, lenticular, rectangle, or hybrid shape and can be constant along the path or different for each node. After creating the geometric model, TexGen® allows exporting it as an IGES file to Comsol Multiphysics®. Figure 2 shows the image of the S1 fabric and the corresponding geometrical model.
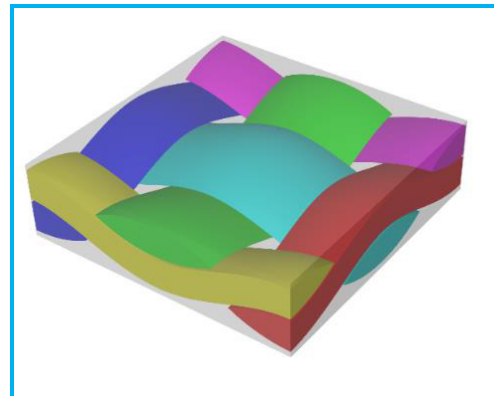

Figure 2. S1 woven fabric structure and 3D geometrical model

3.3. Experimental devices

To find out the experimental values of the heat flow through fabrics the device from Figure 3 was used.

The constant temperature of the lower border is provided by a calorimeter connected to a *Julabo* thermostatic bath while at the upper border, there is a radiator with a high dissipation power. The heat flux is monitored with a Captec flow sensor and the temperature is measured by the Omega type E thermocouples. Professional precision spacers are used to avoid changing the thickness of the textile material. The data obtained from the sensors are collected by the Data Acquisition System, DAQ Keithley 2700, taken over by a computer, and processed in Excel.
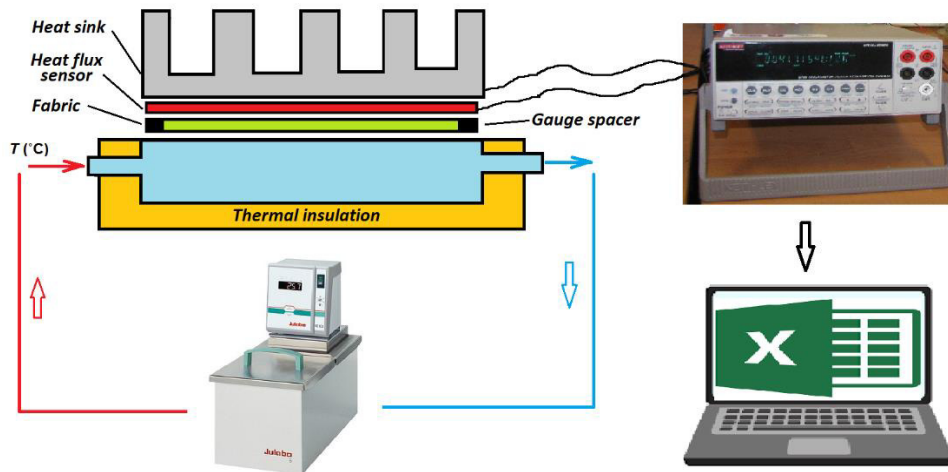
Figure 3. Experimental device to measure heat transfer through textile materials

4. RESULTS AND DISCUSSION

Table 2. gives the characteristics and thermal properties of the fabrics used in this study.

Table 2. The characteristics and thermal properties of woven fabrics

Properties	Symbol	S1	S2	S3	S4	S5
		93% Nomex® 5% Kevlar® 2% PA (antistatic)	40% PBI 58% Kevlar® 2% PA (antistatic)	95% Nomex® 5% Kevlar®	93% Nomex® 5% Kevlar® 2% PA (antistatic)	50% Viscose 47% Nomex® 2% Kevlar® 1% PA (antistatic)
	Units	Plain-weave	Plain-weave	Plain-weave	Plain-weave	Plain-weave
Yarn-linear density, T_t	tex	55	45	20	20	20
Warp/Weft density	yarns/cm	21/21	19/19	38/38	32/29	26/23
Warp/Weft yarn spacing	mm/mm	0.476/0.476	0.526/0.526	0.263/0.263	0.312/0.344	0.384/0.434
Surface weight	g/m²	242	211	150	110	130
Density	kg/m³	562	527	441	423	433
Thickness	mm	0.43	0.40	0.34	0.26	0.30
Thermal conductivity	W/(m·K)	0.1154	0.2122	0.1074	0.1073	0.1142
Specific heat capacity	J/(kg·K)	951	655	1026	964	1184
Thermal resistance	(m²·K)/W	0.0129	0.0115	0.0105	0.0085	0.0097

To validate the 3D model of each fabric from Table 2, the thermal resistance, Rct, determined according to ISO 11092/2016 was compared with the value obtained by simulation at steady-state. The results are shown in Figure 4. The boundary conditions used in the simulation are the same as the standard ones: the lower side temperature, Tm, is 35 ºC, the upper side temperature, Ta, is 20 ºC, and the relative humidity RH of 65 %.

By definition, thermal resistance is defined as the ratio of the temperature difference between the two faces of a material to the heat flow:

$$R_{ct} = \frac{\Delta T}{\Phi} \qquad (10)$$

The thermal resistance values obtained from the microscopic simulation in Comsol® are local values because they depend on the point where the calculation was performed. However, to compare with the experimental results, global values are required. These values were obtained by using averaging functions provided by Comsol® and are related to the surface integral over a 2-dimensional domain.

It is noted that the values resulting from the simulation are close to the standard measurements, proving a good agreement between the predicted and experimental data. The correlation coefficient calculated between the two data sets is 0.999, which indicates a very good correlation. However, the predicted thermal resistance is lower than the experimental values within a deviation range of 4.2% to 6.3%. The reason behind these differences is given by the assumptions taken into account when the geometric model was created. Actually, the thermal conductivity of the yarns is lower than the calculated values due to their microporous nature. There is an important factor that influences the thermal conductivity of the yarns, namely the contact surface between the fibers, and it is related to the technological parameters.

To highlight the importance of the model scale in the simulation of heat transfer, two approaches were considered: microscopic and macroscopic scales at transient conditions. The simulations were performed for the fabrics and the results were compared with experimental determinations. The boundary conditions were those stipulated in ISO 11092/2016, while the initial temperature of the sample was 20 °C with a relative humidity R.H. of 65 %.

As can be seen in Figures 5.a. and 5.b., the intermediate values of heat flow on 3D simulation have also a non-uniform distribution, and therefore an averaging value must be calculated with the surface integral of the local heat flow divided by the total surface value.

The experimental values were obtained under the same initial and boundary conditions using the device from Figure 3. The transient heat flow is similar for all studied samples. An example for the fabric S1 was provided to highlight distinctions between the micro and macro-scale approaches in dynamic simulation scenarios (Figure 6). The differences between the simulated and experimental data are shown in Figure 7.
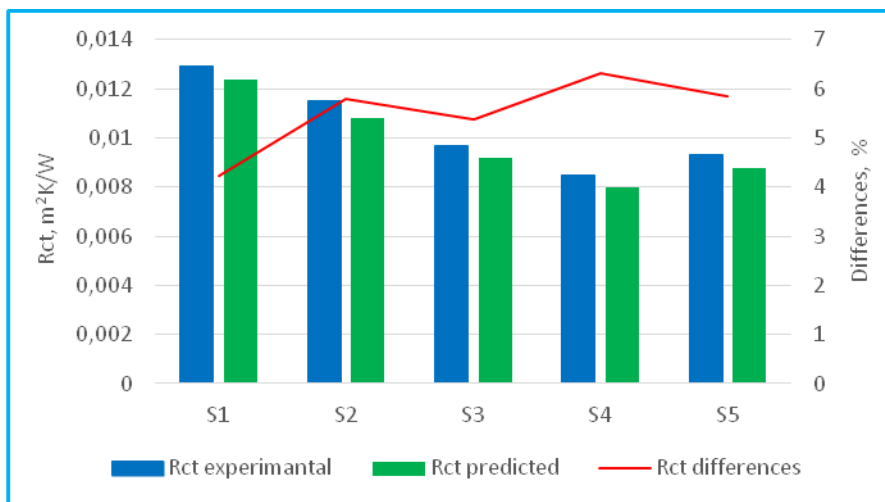

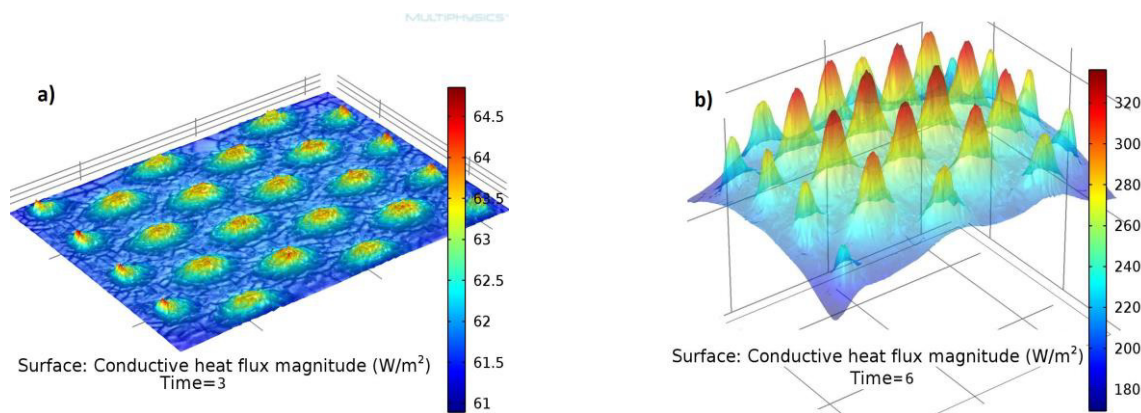**Figure 4.** Comparison of predicted thermal resistance with experimental results

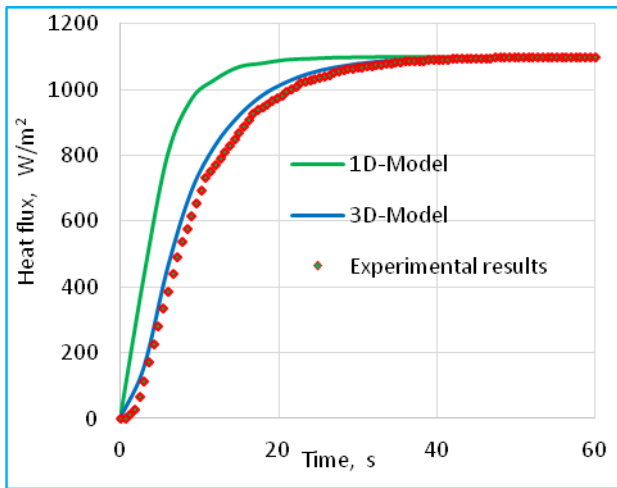**Figure 5.** 3D distribution of heat flow simulated for S1 fabric after 3s (a) and 6s (b), respectively.

Figure 6. The experimental and simulated values of heat flow for the S1 fabric
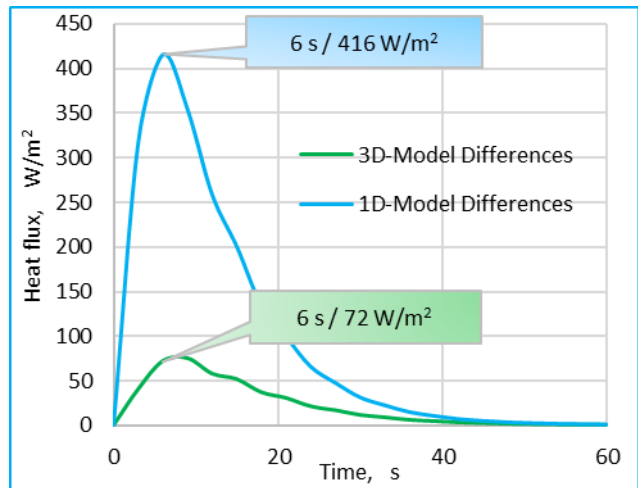

Figure 7. Heat flux differences between the experiment and simulation for the S1 fabric

The heat flux, for both simulation scales, shows values very close to the experimental data at steady-state, while in the transition area, substantial differences are observed. These differences are given by the rate of flux variation passing through the fabric reported to the time unit (the first derivative). From the 1D modeling, it can be concluded that the textile material would have a lower "thermal inertia" than in reality. For example, the 1D simulation estimates that the heat flow through the textile material reaches the value of 1000 W/m^2 in about 10 s, while the 3D modeling estimates 20 s, which is very close to the experimental value of 21.5 s. Thus, the 3D model can reproduce more faithfully the behavior of the textile material in the case of transient heat transfer because the results are much closer to the experimental data. Accurately, estimating the dynamic heat transfer performance is crucial on firefighter clothing because heat flux and exposure time are closely related to the degree of burns that the human skin can suffer. Stoll and Chianta [25] have quantified the reaction of human skin (second-degree burns) based on the thermal flux received by the human body and the time of exposure.

5. CONCLUSION

Using the Comsol Multiphysics® software, the heat transfer simulation through woven fabrics was performed for both microscopic (3D) and macroscopic (1D) scales. At steady-state, the heat flow through the 3D textile model has a relatively constant value and it was used to determine the thermal resistance of the woven fabrics. The values obtained have a deviation between 4.2 % and 6.3% from the thermal resistance of the fabrics determined according to ISO 11092/2016. Thus, the 3D model was validated with

the experimental results and a good correlation was found at steady-state.

The heat flux variation for both micro and macro-scale simulations was compared also on transient conditions. Although, the microscopic and macroscopic approaches do not show significant differences in terms of heat transfer at steady-state, for the transient area the micro-scale modeling provides more accurate results. Usually, in the textile field, the microscopic approach has not been widely used due to the very large hardware resources required but is of particular interest in the design of protective clothing for firefighters, the development of thermal insulation materials, and the optimization of temperature control in textiles for comfort and performance. For such applications, the use of accurate modeling justifies the necessary software resources, especially since the current technological advance has led to a large decrease in simulation costs.

The future research will focus mainly on:

➢ Carrying out simulations for high and very high heat flows and comparing the results with the experimental ones carried out within the standard EN ISO 6942:06/2002.

➢ Performing the mass transfer simulation through textiles and coupling the mass transfer with heat transfer that occurs simultaneously.

➢ Parameterization of geometric models to optimize complex textile structures in terms of heat and mass transfer.

REFERENCES

1. Codau E., Codau T. C. 2021. *Transferul de caldura si masa prin materialele textile*, Performantica, (Iasi) .

2. Hes L. et al. 2015. Analysis of heat transfer in inflatable sleeping pads, *Tekstil ve Konfeksiyon,* vol. (25), 300–303.

3. Angelova R. A. et al. 2016. Experımental study and numerıcal sımulatıon of the aır permeabılıty of systems of woven macrostructures, *Tekstil ve Konfeksiyon,* vol. (26), 385–392.

4. Torvi D. A., Dale J. D. 1999. Heat transfer in thin fibrous materials under high heat flux, *Fire technology,* vol. (35), 210–231.

5. Mell W. E., Lawson J. R. 2000. A heat transfer model for firefighters' protective clothing, *Fire Technology,* vol. (36), 39–68.

6. Gibson P. W. 1996. *Multiphase heat and mass transfer through hygroscopic porous media with applications to clothing materials,* University of Massachusetts Lowell.

7. Chen G., Prasad V., Jaluria Y. 2015. *Annual review of heat transfer,* Begell House.

8. Łapka P., Furmański P., Wisniewski T. S. 2016. Numerical modelling of transient heat and moisture transport in protective clothing, *Journal of Physics: Conference Series,* vol. (676).

9. Onofrei E. et al. 2014. Simulation and modeling of heat and mass transfer through fabrics exposed at low-level thermal radiation. In *7th International Textile, Clothing & Design Conference – Magic World of Textiles*, Dubrovnik, Croatia, p. 418-423.

10. Rathore M. 2015. *Engineering Heat and Mass Transfer,* Third edition, Laxmi Publications, New Delhi.

11. Cengel Y., Ghajar A. 2015. Heat and Mass Transfer: Fundamentals and Applications, Fifth edition, vol. (1,) Columbus: McGraw-Hill.

12. Song G. 2002. Modeling Thermal Protection Outfits for Fire Exposures. PhD Thesis. North Carolina State University. Available: https://repository.lib.ncsu.edu/handle/1840.16/5766.

13. Bejan A. 2013. *Convection Heat Transfer*, Fourth edition, vol. 1, John Wiley & Sons, New Jersey.

14. Incropera P. F. et al. 2011. *Fundamentals of Heat and Mass Transfer*, 7th edition, John Wiley & Sons, New Jersey.

15. Pezzin A., 2015. *Thermo-physiological comfort modelling of fabrics and garments*, Politecnico di Torino, Torino, Italy.

16. Morton W., Hearle J. 2008. *Physical Properties of Textile Fibres -* Fourth edition, Woodhead Publishing Limited number 68, Cambridge, England.

17. DuPont. 2023. *Kevlar® Aramid fiber technical guide*, https:www.dupont.com

18. Comsol Inc. *Introduction to COMSOL Multiphysics®*, https://www.comsol.com/documentation [Accessed 14.09.2021].

19. Courant R. 1943. Variational methods for the solution of problems of equilibrium and vibrations, *Bulletin of the American Mathematical Society,* vol. (49), no. 1, 1-23.

20. Pierce F. 1937. The geometry of cloth structure, *Journal of the Textile Institute,* vol. (28), 45-96.

21. Kemp A. 1958. An extension of Pierce cloth geometry to the treatment of noncircular, *Journal of the Textile Insitute,* vol. (49).

22. Hearle J., Shanahan W. 1978. An energy method for calculations in fabric mechanics part II: examples of application of the method to woven fabrics, *The Journal of The Textile Institute,* no. 4, 92-100.

23. Rasband W., Ferreira T. 2012. "imagej.nih.gov." Public Domain - Java Image Processing Program, [Online]. Available: https://imagej.nih.gov/ij/download.html. [Accessed 08.09. 2021].

24. http://texgen.sourceforge.net/, University of Nottingham, 2021. [Online]. Available: https://sourceforge.net/projects/texgen/.

25. Stoll A., Chianta M. 1969. Method and Rating System for Evaluation of Thermal Protection, *Aerospace Medicine,* vol. (40), no. 3.